Design of Generalized Fiber-reinforced Elasto-fluidic Systems

by

Joshua L. Bishop-Moser

A dissertation submitted in partial fulfillment
of the requirements for the degree of
Doctor of Philosophy
(Mechanical Engineering)
in the University of Michigan
2014

Doctoral Committee:

Professor Sridhar Kota, Chair
Professor Jessy W. Grizzle
Assistant Professor C David Remy
Professor Kon-Well Wang

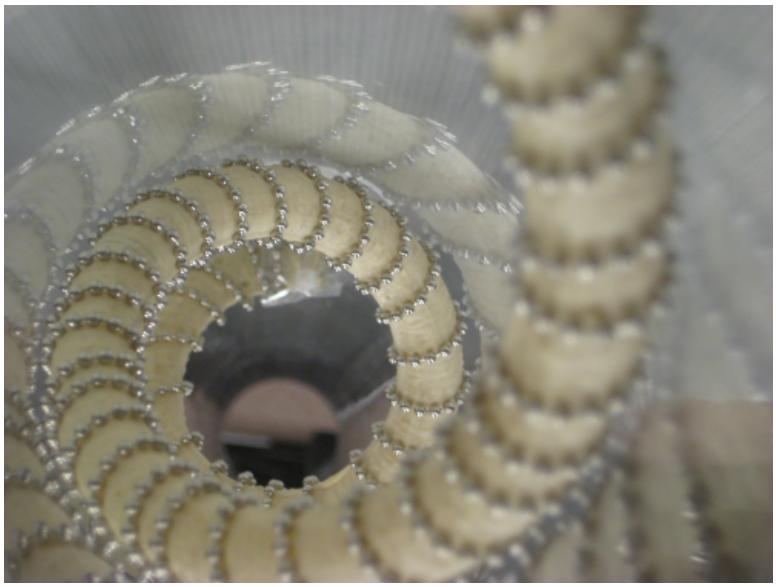

To my mom, Lauren, and my girlfriend, Darlene.
Thank you for all your love and support.

A C K N O W L E D G M E N T S

There are many people who have supported and influenced me, and I would like to thank them for helping me reach this point in my life and complete my doctoral work.

I would like to express my gratitude to my advisor and committee chair, Professor Sridhar Kota. I chose to come to the University of Michigan primarily to work with him, as he is the best at what he does. He supported my intellectual exploration, including my initiation of dozens of projects on ideas spanning the area of compliant systems design. He is a brilliant mechanical designer and engineer with an undeniable passion, and I have honed my skills under his guidance. He has mentored me in the art and science of research and engineering.

I was welcomed to the Compliant Systems Design Lab (CSDL) by Dr. Michael Cherry, Dr. Girish Krishnan, and Dr. Youngseok Oh. Michael is an impressive engineer and one of the nicest people I have ever met. I have collaborated with and bounced many ideas off of Girish. I want to thank them for helping me progress my research ideas.

This work could not have been completed without the help of my exceptional research assistants Kevin Lapprich, Adam Joyce, Jason Francolini, Corey Bertch, Darlene Yao, and Teresa Tombelli. From designing components to creating numerous prototypes to running experiments, these six were essential to the completion of my doctoral work. Kevin and Jason are skilled at fabrication and design for manufacturability. Adam has outstanding mechanical design creativity. The experiments could not have been completed without Corey and Darlene's impressive dedication, skill, and precision in fabricating prototypes. Teresa is an adept engineer and tirelessly ran experiments.

I would like to thank my committee members, Professor Jessy Grizzle, Assistant Professor David Remy, and Professor Kon-Well Wang. It is an honor to have such an impressive and distinguished committee review and guide my work. Additionally, this research would not be possible without funding from the National Science Foundation under NSF Award 1030887 and the Graduate Research Fellowship.

I would not have reached this point without my mother, Lauren Bishop. She has always loved me and supported me throughout my entire life, providing encouragement in every way she could. Much of my academic, creative, and scientific abilities are a direct result of her. My girlfriend, Darlene Yao, has been the best support system I could have ever asked for. She has been there through the challenges and excitement of the entire process, always cheering me on. I could not have completed this dissertation without everything she has done for me.

TABLE OF CONTENTS

LIST OF FIGURES

LIST OF TABLES

ABSTRACT

Design of Generalized Fiber-reinforced Elasto-fluidic Systems

by

Joshua L. Bishop-Moser

Chair: Sridhar Kota

From nature to engineered solutions, the metrics of mechanical systems are often strength, power density, resilience, adaptability, safety, scalability, and the ability to generate the necessary forces, motions, and forms. The use of fluidic structures with fiber reinforcement to realize these metrics is seen throughout nature; however, these structures are rarely used by engineers, in part due to the absence of a generalized understanding of their kinematics and forces. Fiber-reinforced elasto-fluidic systems use fluid pressure to actuate an envelope with tuned compliance to provide desired motion, forces, flexibility, and transmission of energy. These structures combine the high strain energy utilization and flexibility of fibers, the versatility and compressive load abilities of fluids, and the continuum nature of soft materials, exploiting the best features of each. These properties and others combine to make elasto-fluidic systems without contact friction and losses, free of joint backlash, scalable in size, safe for human interaction, resilient to impact, adaptable to external forces and constraints, low cost, and high in power density. These systems have a wide range of forces and motions, are able to be combined in parallel, form complex shapes, and eliminate the need for subsequent mechanisms for geometric or mechanical advantage.

This dissertation discovered a vast array of previously unknown fiber-reinforced elasto-fluidic systems, models their mechanical behavior, experimentally verifies the models, creates methods for easy design synthesis, and applies this knowledge to multiple practical applications.

A small subset of elasto-fluidic systems, popularly known as McKibben actuators, has been thoroughly investigated in the past half-a-century. McKibben actuators, generating extension or compression, represent only a very small portion of possible designs. Therefore, a vast design space of possible structures with multiple sets of fibers and different orientations yielding a rich array of functionality were yet to be investigated and applied to a wealth of applications. This dissertation develops the mechanics of generalized fiber-reinforced elasto-fluidic systems by first modeling the relationship of volume change and fiber orientation to motion kinematics and force generation. The kinematics of motions including translation, rotation, screw, bending, and helical were all modeled. Fiber configurations spanning the design space were tested to experimentally verify the predicted forces and motion. The force and kinematics were combined to form a design synthesis tool that maps the desired motions, freedoms, and constraints to fiber configurations. Synthesis methods were created for parallel combination of fiber-reinforced structures using discretized force and freedom directions. Lastly, novel applications were created using these fiber-reinforced elasto-fluidic structures, including an orthosis device for arm rotation contractures, a soft hexapod robot with an actuated flexible spine, and a structure for anchoring within pipes.

CHAPTER 1

Introduction

From nature to engineered solutions, the metrics of mechanical systems are often strength, power density, resilience, adaptability, safety, scalability, and the ability to generate the necessary forces, motions, and forms. The use of fluidic structures with fiber reinforcement to realize these metrics is seen throughout nature; however, these structures are rarely used by engineers, in part due the absence of a generalized understanding of their kinematics and forces.

1.1 Distributed Compliance

Distributed compliance is the use of material strain across large regions of a mechanism or structure. This compliance can take many forms, from thin beams to fibers to soft materials to fluids; yet, they all result in the same advantages of better material utilization, reduced part count, reduced or eliminated friction, responsiveness to perturbations, ability to withstand shock loads, and scalability.

1.1.1 Flexibility in Nature

Flexibility is found throughout nature, from plants to animals, from organisms microns to meters in length, aquatic to aerial to terrestrial. This flexibility can be passive, responding to changes in the environment, or active, creating force and/or motion. The key inspiration nature provides for this work is an understanding that flexibility and strength are not mutually exclusive. Despite the use of rigid structures in most of engineering, flexibility is the norm in nature. This flexibility takes many forms, sometimes using soft materials, other times using large aspect ratios, and in many cases using fluids and fibers. The elegant dexterity, adaptability, and complex motions of tongues and octopus tentacles, the practicality and stiffness of the penis, and the strength and intricacy of echinoderm feet all drive the desire to further understand flexible systems that uses fluids and fibers.

1.1.2 Compliant Mechanisms

Compliant mechanisms use material deformation to obtain desired motion, stiffness, and force transmission. There are three main types of compliant mechanisms: hybrid, lumped compliance, and distributed compliance. Hybrid systems use traditional joints (e.g. pin joints, sliding joints) and compliant elements. Lumped compliance uses narrow regions of reduced material to create localized material deformation, mimicking the behavior of a joint. Compliant mechanisms utilizing distributed compliance exploit material deformation across a large portion of the mechanism to obtain desired properties.

Distributed compliant mechanisms use the aspect ratio of the material, often using long thin beams, to obtain large ranges of motion. High aspect ratios allow for large deformation using materials that have relatively low yield strain, such as plastics and metals. The topology of the beams is the primary means to control the kinematics of the output [25] [31] [42] [80], a concept that can be readily applied to fiber-reinforced elasto-fluidic systems.

1.1.3 Fibers and Fabrics

Fibers use extremely high aspect ratios to ensure sufficient flexibility such that applied forces act primarily along the fiber direction. This tensile loading optimally distributes the strain energy, providing the most effective use of the material. The flexibility provides ample motion ability in directions that are outside of the fiber's axial direction. Fabrics extend this advantage to multiple directions, allowing for high flexibility combined with high strength. Fiber-reinforced composites use the high strengths of fibers and fabrics to create high strength to weight ratio structures. These advantages drive the desire to use fibers as integral load bearing components in mechanical systems, especially those with large deformations.

1.1.4 Soft Materials

Soft materials have a very high strain at failure and often a low ultimate tensile strength. Examples of these materials are silicone, latex, natural rubber, and other elastomers. These materials substantially deform while maintaining a continuum surface, which is useful for containing fluids in distributed compliance systems. The soft material is able to collect and concentrate distributed loads; the reverse of distributing concentrated loads can also be performed. These advantages present the opportunity to use soft materials as an intermediary between fluids and high load bearing elements such as fibers. The immense flexibility and extensibility of these materials ensures their shape can adapt to environmental factors.

1.1.5 Hydraulics and Pneumatics

Hydraulic and pneumatic systems use pressurized fluid to transfer force and motion throughout a system. These systems are often utilized for their ability to transduce fluid pressure to force with high power density, operate many actuated degrees of freedom with a single centralized pressure source, and withstand impact loads in their actuation direction. The fluid acts as a transmission member, transferring force and motion from one location and direction to others, in much the same way a link would in a traditional rigid link mechanism. However, unlike rigid link mechanisms, fluidic systems are able to easily distribute, concentrate, and redirect loads in many directions without requiring a multitude of mechanical connections. Current hydraulic and pneumatic systems have the drawbacks of expensive precision machined components, inability to withstand transverse impacts, higher than necessary weight, and use of sliding joints that can wear out. These numerous advantages of fluidic systems motivate the need for research on how to use soft distributed compliance to eliminate or reduce the drawbacks.

1.2 Elasto-fluidic Systems

Elasto-fluidic systems use fluid pressure to actuate an envelope with tuned compliance to provide desired structure, motion, flexibility, and transmission of energy. These systems can be monolithic, fiber or beam reinforced, fabric reinforced, or rigid element reinforced. Monolithic systems use only the material distribution to control the system's behavior, using thick sections of soft material to act as more rigid constraints, and thin sections to be more flexible. Fiber or beam reinforced systems use the inextensibility of fibers and beams to sustain loads in certain directions, while all other directions remain free to deform. These systems provide a high contrast between the stiff directions and the compliant directions. Fabric reinforced structures have inextensible surfaces, relying only on the bending of the surface under load to obtain deformation. Rigid element reinforced systems use plates or rigid structures to prevent the deformation of an elasto-fluidic system in multiple directions. These systems often use flexible elastomeric hinges with rigid connecting plates. There is a trade-off in these methods between control and range of motion, shown in Figure 1.1, with rigid element reinforced systems maximizing control, while monolithic maximize range of motion. Fiber-reinforcement provides a desirable combination of highly controlled motion with highly distributed strain.

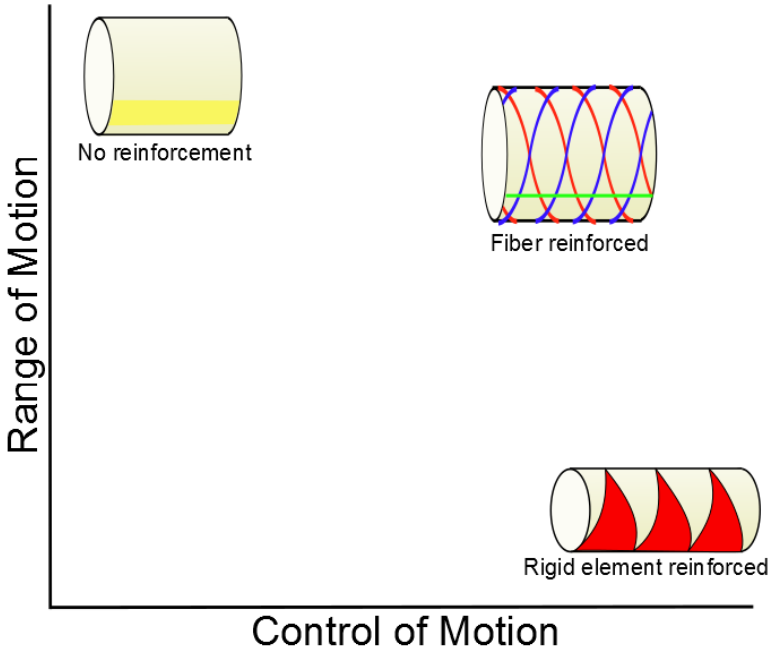

Figure 1.1: Comparison of range of motion to control of motion for different types of elasto-fluid systems. Fiber-reinforced systems have a desirable combination of properties, providing controlled motion and a large deflection range.

1.2.1 Advantages

Elasto-fluidic systems do not use discrete joints, which eliminates wear and energy loss from contact friction, allows for scalability of the design to very large or small sizes, and eliminates backlash. The soft structure allows for safe human interaction, as there are no heavy, rigid portions or dangerous joints. The soft continuum nature of the fluid and exterior ensure resilience against impacts, while providing adaptability of the system to external forces and constraints. This adaptability allows the actuators to be easily combined in parallel to form more complex motions. In fiber-reinforced systems, the fluid is in pure compression, the fibers in pure tension, and the soft material under large strain; this ensures lightweight, high power density structures and actuators through highly distributed strain energy. The diversity of fiber orientations allows for a wide range of force and deformation patterns as well as complex shapes, providing the opportunity for numerous applications. The layout of the fibers provides mechanical or geometric advantage that is integrated into the actuator, reducing or eliminating the need for further mechanisms. Elasto-fluidic systems are very low cost due to their simple design and use of inexpensive materials.

1.2.2 Applications

The advantages and versatility of elasto-fluidic systems, especially when fiber-reinforced, provide opportunities in a wide range of applications. Medical, aerospace, communications, manufacturing, robotics, toys, consumer products, energy, and many other areas have challenges that would substantially benefit from elasto-fluidic systems. Three of these numerous areas are explored in this thesis. An orthosis device for generating torsion at the arm is discussed in Section 4.4, a mobile robot with a soft spine is developed in Section 5.3, and a pipe inspection robot body design is developed in Section 6.4. While further research and development is needed to fully realize these and other applications, the research presented in this dissertation creates a critical first step in their development. Further engineering and research on dynamics, controls, manufacturing, and application specific challenges will need to be performed.

1.3 Literature Review

This section presents a summary of some of the previous work in elasto-fluidic systems. Section 1.3.1 reviews literature on elasto-fluidics in nature, Section 1.3.2 reviews fiberless elasto-fluidics, and Section 1.3.3 reviews fiber-reinforced elasto-fluidic systems.

Continuum actuated structures and manipulators have been explored by multiple authors. Greef et al. present a review of flexible fluidic actuators with an interest in their use as medical instruments [18]. Webster et al. review the literature on continuum constant curvature robots, focusing on kinematics and modeling [88]. Trivedi et al. review the state of the art in soft robotics, including the soft fluidic organisms in nature that inspire this work [81].

1.3.1 Elasto-fluidics in Nature

Nature provides a wealth of examples of fiber-reinforced elasto-fluidic systems in a wide range of environments and fiber configurations. Kier presents an overview of fiber-reinforced elasto-fluidic biological structures, commonly known in biology as muscular hydrostats [35]. Vogel presents another review of hydrostatic mechanisms used in nature [86]. A fiber-reinforced elasto-fluidic structure that contains no actuating muscles, a close proxy to engineered solutions with passive fibers, is the penis. Kelly presents a study of fiber arrangement in the fibrous tissue of penises spanning multiple species [33] [34]. Thompson et al. present the fiber reinforcement of the erectile tissue of the octopus copulatory organ [77].

Many animals have fibers in their outer layers. Alexander investigates bending of cylindrical animals with helical fibers in their skin (such as worms, fish, and whales), presenting a model of the kinematics of the fibers when bending [4]. Koehl et al. study the effects of osmotic pressurization of helically wrapped embryonic notochords [39], demonstrating the transition from extension to contraction of oppositely wound helical fibers at approximately 54° in a biological structure. McCurley et al. examine the structure of starfish feet, which use fluid pressure to actuate the fiber-reinforced outer structure [53]. Seymour determines the effect of helical fibers in the cuticles of worms and the resulting effect on motion, also presenting a simple kinematic model [70]. Shadwick presents a short review of helical fiber-reinforced organisms with a focus on their contained volume relative to the maximum potential contained volume [71]. Wainwrite presents an overview and simple kinematic models of fiber reinforcement in biological structures [87]. Holzapfel et al. present a model of the fiber reinforcement of the artery wall [28]. While these investigations into nature provide inspiration, an understanding of the kinematics and forces across the entire design space has not been explored.

1.3.2 Elasto-fluidics Without Fibers

There are a range of studies on elasto-fluidic systems that do not use fibers. Ilievski et al. developed a pneumatically actuated soft starfish shaped robot using a monolithic silicone body. [29]. Kusuda et al. present a monolithic pneumatically actuated elastomeric bending device [44]. Deng et al. presented a similar device, adding mathematical modeling [19]. These bending actuators have been extended to three inflatable chambers for bending in all directions by Chen et al. [12] and Martinez et al. [49]. Onoe creates multiple inflatable chambers in a continuum elastomeric material to generate locomotion [60].

Other work has focused on inextensible surfaces. The first approach is to use inflatable chambers of air, which have been used by Konishi et al. to actuate a finger like manipulator [40], Kimura et al. to generate a rolling robot that uses pneumatic bags as both the body and the actuation [36], Vaidyanathan et al. to create an underwater robot with inflatable sections [85], Maruyama to create arm-like manipulators [51], and by Laschi et al. to create an octopus arm inspired robot [46]. There have been many bellow configurations created, with Granosik et al. actuating a snake robot [24] and Immega et al. actuating a continuum octopus-like manipulator [30]. Other approaches such as cable driven elastomer structures by Calisti et al. [11] have been used to create manipulators mimicking octopus arms. These approaches generally create actuators, robots, and devices that have limited levels of output position control, as they are under-constrained.

1.3.3 Fiber Based Elasto-fluidics

There are multiple fiber configurations that have been explored, many captured in review papers by Daerden et al. [15] and Zhang et al. [90]. The one that has received the most research and commercial success is the McKibben actuator, patented by Gaylord in 1958 [21]. This configuration of equal and opposite fiber angles has been extensively modeled and analyzed. Tondu et al. present a review of force and kinematic modeling of the McKibben actuator [79]. Analytical and computational modeling of the McKibben actuator, with some papers performing experimental testing, have been presented by Adkins et al. [1], Chou et al. [13], Colbrunn et al. [14], Davis et al. [16], Goulbourne [23], Kawashima et al. [32], Klute et al. [37] [38], Kothera et al. [41], Kydoniefs [45], Liu et al. [47], Manuello et al. [48], Moss et al. [55], Nelson et al. [56], Shan et al. [72], Tondu et al. [78], Tsagarakis et al. [84], and Zhang et al. [90]. Holzapfel investigated fiber-reinforced cylindrical composite structures with McKibben style fiber layout using similar analysis methods to those used for the McKibben actuator [27]. All of these models use a single fiber angle, since the two families of fibers are assumed to be equal and opposite helices. While these models present a very good starting point for analyzing fiber-reinforced elastomeric enclosures, their underlying assumptions limit their scope. This limitation prevents the models from being usable in analysis or synthesis across the vast majority of the design space.

Multiple researchers have studied how to place McKibben actuators in parallel to control tentacle-like motion. Octarm uses three or six actuators in parallel, and has been extensively studied by Trivedi et al. [83] [82] and McMahan et al. [54]. Zhu combined multiple McKibben actuators in parallel in a soft medium [91]. Suzumori et al. placed a fiber reinforcement around multiple parallel pneumatic chambers [75] [74]. Wedler et al. created a Stewart platform using McKibben actuators [89]. Peel et al. investigated the application of McKibben actuators to deformable wings [67]. Peel also studied the fabrication of McKibben actuators [66] [64] and their application to powering an arm [65]. These parallel manipulators show the potential for soft robots, but their reliance on McKibben actuators limits them to a small subset of the wide range of possible motions and forces.

Outside of McKibben actuators, Ghoneim et al. investigated the use of a single family of fibers to reinforce a soft enclosure for pumping [22]. Paynter et al. created rotational actuation of fiber-reinforced pneumatic structures that have a single family of fibers [62] [61] [63], and Noritsugu et al. used the same configuration to create rotation for a medical application [57]. Matsikoudi et al. presented a mathematical analysis of rotation deformation of a single family of fibers [52]. Seok et al. added actuated fibers to a McKibben configuration to create a peristaltic worm robot [69]. Galloway et al. researched a fabrica-

tion method for easy creation of bending McKibben actuators [20]. Martinez et al. added fibers and rigid sections to soft fluid filled enclosures, including adding a single fiber to create a helical pattern when inflated [50]. These alternative fiber reinforcement designs show the potential for more complex motions, but do not explore the design space.

I have previously published research on fiber based elasto-fluidic systems. Sections of these publications are presented in the chapters of this dissertation. Portions of Chapter 2 are seen in [43]. Portions of Chapters 3 and 5 are seen in [8]. Portions of Chapter 5 were presented in [7]. Work in Chapters 3 and 4 were shown in [9]. Additional sections from Chapter 4 were published in [10], while most of Chapter 6 was published in [6].

1.4 Problem Statement

A small subset of elasto-fluidic systems, popularly known as McKibben actuators, has been thoroughly investigated in the past half-a-century. McKibben actuators, employing fibers at equal and opposite angles, represent only a very small portion of the entire design space. Therefore, a vast design space of possible structures with multiple sets of fibers and different orientations yielding a rich array of functionality are yet to be investigated and applied to a wealth of applications. These actuators have been inaccessible because of a lack of understanding of their mechanics: kinematics, forces, volumetric effects, and parallel combinations. An in depth knowledge of these properties as well as their stiffness, dynamics, and controllability will allow fiber-reinforced elasto-fluidic systems to become a regular part of mechanical design. Analytical modeling of these actuators is a necessary first step towards establishing a generalized methodology for the synthesis of an entire class of elasto-fluidic systems.

1.4.1 Research Goals and Scope

The overarching goal of this research is to understand the mechanics of generalized fiber-reinforced elasto-fluidic systems in order to realize their numerous advantages. Specific objectives of this thesis are:

1. Explore the entire design space of fiber-reinforced actuators with multiple sets of fibers and varying fiber angles.

2. Develop analytical models that relate volume change and fiber orientation to motion kinematics of fiber-reinforced systems.

3. Experimentally verify analytical kinematic models.

4. Analytically model and experimentally verify forces and moments generated for all fiber orientations.

5. Develop design synthesis tools that map desired motions and forces to corresponding fiber configurations and orientations. Desired motions include translation, rotation, screw, bending, and helical motions.

6. Create a synthesis model for parallel combinations of fiber-reinforced structures with one or two families of fibers to generate complex and coordinated motions.

7. Demonstrate novel applications of fiber-reinforced elasto-fluidic systems.

The scope of this dissertation includes the study of kinematics and forces generated. Material models needed to understand stiffness, dynamics, and controllability of fiber-reinforced systems are beyond the scope of this thesis.

The scope of fiber reinforcement configurations is limited to single and dual families of fibers as well as single or dual families of fibers with an additional single fiber added. Analysis of parallel configurations is limited to single and dual families of fibers placed in parallel triplets with their primary axis in parallel. Elastomeric effects were not modeled, limiting the utility of the analysis on configurations containing only a single family of fibers, as their fluid containment and kinematics are both underconstrained. Three or more families of fibers were not considered, as this configuration either prevents all actuated motion or cause no change in behavior from the configuration with two families of fibers. Configurations with only single fibers, rather than families of fibers, are outside the scope of this thesis, as their deformation is substantially based on the material and structural properties of the elastomer, rather than primarily on the fiber reinforcement. Configurations with two families of fibers and two or more single fibers is overconstrained, thus generating no motion. Configurations with one family of fibers and two single fibers, while fully constrained in kinematics, are not fully constrained in fluid containment, thus their behavior is dependent on material properties. These conditions are summarized in Figure 1.2.

Series combinations of actuators were not considered, as their freedoms, constraints, and actuation can be easily combined using existing techniques used in robotics and mechanism synthesis. Combinations with two actuators in parallel is not presented in this thesis, but can be easily derived from the analysis of triplets of actuators; this analysis was presented previously [8]. Four or more actuators in parallel can be understood from triplets of actuators, since there are no additional constraint couplings that are not already addressed in this research. Parallel combinations of actuators in which the primary axes of the structures are not parallel were not addressed since this is still an active topic of research in

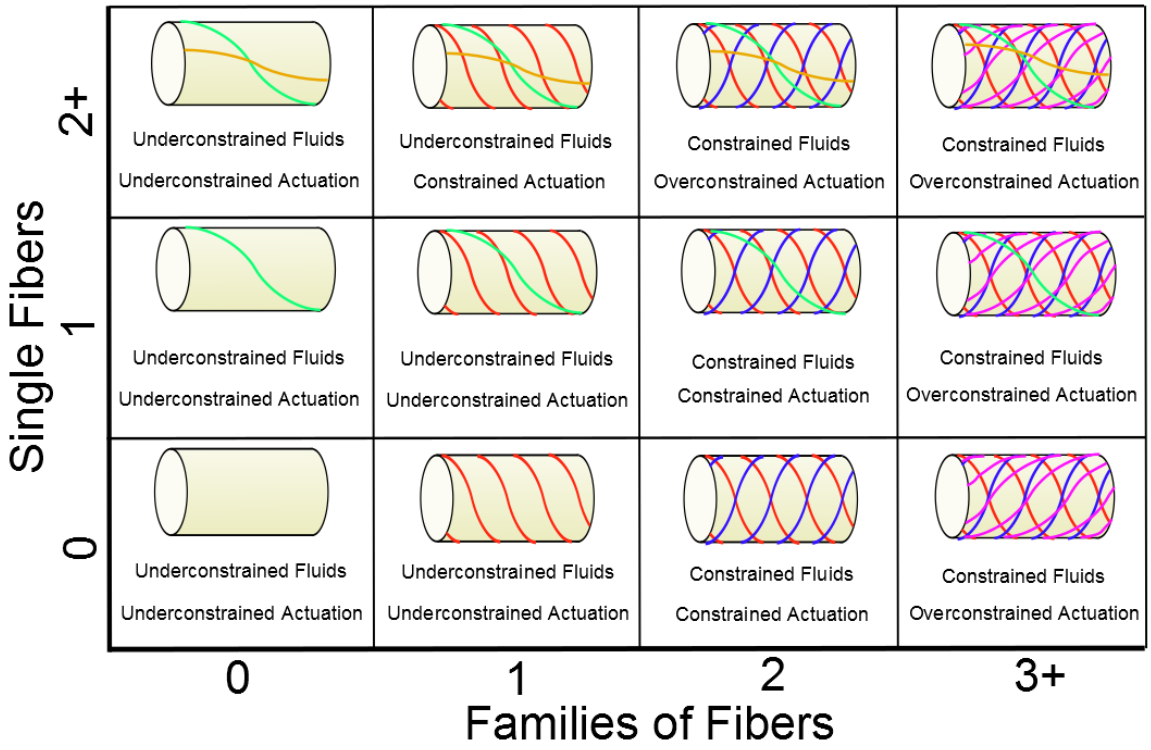

Figure 1.2: Possible fiber reinforcement configurations with their respective constraints of fluid expansion and actuation. Underconstrained fluids are able to expand between fibers. Underconstrained actuation is able to expand in multiple directions with the elastomer stiffness controlling the direction of motion. Overconstrained actuation either does not actuate or has no difference in behavior to the constrained case.

existing traditional rigid link mechanisms; this area was left to future work.

1.4.2 Organization of Thesis

This thesis is organized by chapters that each cover an aspect of the mechanics modeling and testing of fiber-reinforced elastomeric enclosures (FREEs), a subset of elastic-fluidic systems. Chapter 2 discusses the kinematics of the cylindrical FREEs containing one or two families of fibers. Also presented is the experimental verification of the kinematics and comparison to the model. Chapter 3 relates the deformation of the FREEs explored in Chapter 2 to their change in volume. An easy to use design chart mapping fiber layout to mobility is presented. Chapter 4 models the forces and moments generated for FREEs, experimentally verifies them, and then compares the experimental values to those predicted by the model. The design of an orthosis device provides an example of the use of the design tools for synthesizing FREEs. Chapter 5 describes a constraint based synthesis method for combining FREEs in parallel to generate desired actuation, freedoms, and constraints. A soft hexapod robot demonstrates the utility of FREEs and the design tools. Chapter 6 presents the kinematics of helical and bending deformation patterns through the use of a single fiber in addition to the existing families of fibers. Case studies and an example of a potential pipe inspection device are presented. Chapter 7 presents future work and potential applications for this research.

CHAPTER 2

Kinematics

The kinematics of fluid actuated fiber-reinforced elastomeric enclosures (FREEs) are controlled by the orientation of the fibers. The motion directions and magnitudes are extracted from an understanding of the underling geometry of the fiber motion as the FREE's enclosure changes in volume. This chapter first discusses the notation and assumptions used for modeling of the fiber-reinforcement. The second section shows a derivation of the FREE's kinematic behavior. The third section explains experiments used to verify the kinematic behavior. The final section presents the experimental results with a comparison to those predicted by the model.

2.1 Notation and Assumptions of Model

The scope of this study encompasses cylindrical FREEs that have circumferentially and longitudinally repeating fiber topologies. This manifests as sets of longitudinal, circumferential, and helical fiber orientations. These fibers can be described using the fiber helix angles α and β with respect to the axial direction. Figure 2.1 shows the helical fiber angle notation for a FREE with two families of fibers. α and β can each range from -90° to 90°, providing a large design space to explore. Angles that are $90^\circ < \alpha < 270^\circ$ can be written as $(\alpha - 180^\circ)$ and angles that are $270^\circ \leq \alpha < 360^\circ$ can be written as $(\alpha - 360^\circ)$. This allows all fiber to be described using the $-90^\circ \leq \alpha \leq 90^\circ$ notation. Helical and longitudinal fibers are arrayed around the cylinder, while circumferential fibers are repeated along the axial length of the cylinder.

The deformation and force behavior of FREEs are governed by the inextensibility of fibers and incompressibility of fluid. Some simplifying assumptions about the FREE's geometry and deformation behavior restrict the analysis and conclusions to a certain class of cylindrical FREEs. These are:

1. Fibers are inextensible with an infinite stiffness.

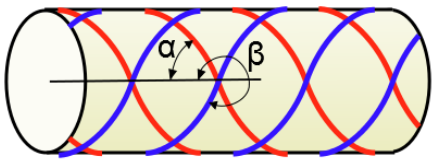

Figure 2.1: Fiber-reinforced elastomeric enclosure (FREE) with 2 families of helical fibers at angles α and β. β can also be written as $(\beta - 360°)$. In this example α is approximately $45°$ and β is $-45°$.

2. Initial and final geometries are perfect cylinders.

3. The fibers have zero thickness and are closely laid with large volume fractions. They do not interfere with the motion of the other fibers that they contact.

4. Fluid volume displacement is assumed to be the same as change in enclosed volume (fluid incompressibility).

5. Fluid pressure is evenly distributed.

6. The effect of the elastomer that encloses the fluid is ignored. The elastomer has zero stiffness effect on the fiber motion and infinite stiffness against bulging between fibers.

7. All analysis is quasi-static.

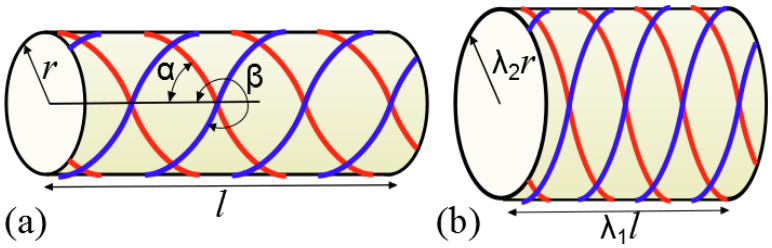

Figure 2.2: (a) Fiber-reinforced elastomeric enclosure (FREE) with 2 families of helical fibers showing the length and radius parameters. (b) Compressed FREE with stretch ratios λ_1 and λ_2 shown.

The length of the FREE is expressed as l, while the radius is r. These are shown in Figure 2.2(a). The axial and radial deformation of a cylinder are expressed as stretch ratios λ_1 and λ_2 respectively, seen in Figure 2.2(b). Stretch ratios λ_1 and λ_2 express the ratio of the deformed length to the initial length; thus a λ_1 of 1 would describe an undeformed axial length, while a λ_1 of 1.2 would describe an axial length that has extended by an engineering strain (ϵ) of 20%. θ is the number of rotations (in radians) that a fiber makes

while spiraling the length of an unactuated FREE, while θ^* is the number of rotations for a deformed FREE. δ is the rotation of one end of a FREE relative to the other due to the change in volume from the unactuated state (again in radians). This value can also be seen as the additional rotation of the fibers from the unactuated to actuated state. V is the volume enclosed in the unactuated state of the FREE, and V^* is the volume in the actuated state.

2.2 Kinematic Model

The kinematics of FREEs are understood by first exploring the effect of the inextensibility of a single fiber. Next, the effect of families of fibers is related to the deformation kinematics. Finally, the relationship between the contained volume of the enclosure and the kinematics of the FREE is analyzed.

2.2.1 Single Helical Fiber

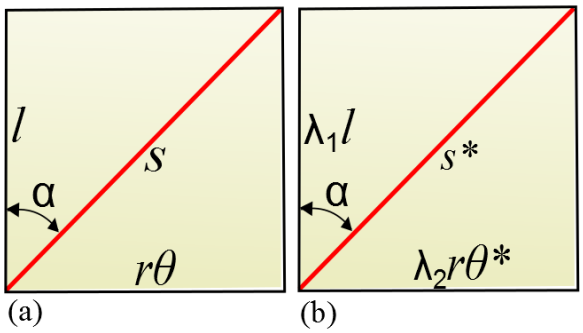

Figure 2.3: (a) A single fiber 'unrolled' or flattened from the cylindrical surface with key parameters shown. (b) The flattened single fiber shown in an actuated state with corresponding changes in parameters.

The inextensibility of a fiber implies that the length of the fiber is the same in the actuated and unactuated state. Figure 2.3(a) shows the fiber on an 'unrolled' or flattened surface, while Figure 2.3(b) shows the same fiber in an actuated state. The fiber may wrap around the cylinder multiple times, in which case the figures show a flattened surface that has multiple 'layers' of the cylindrical surface unrolled to flatten the entire fiber. Equation 2.1 shows the derivation of the parameter relationship that must hold for the fiber to remain constant in length.

$$
\begin{aligned}
l &= s\cos(\alpha) \\
r\theta &= s\sin(\alpha) \\
s = s* &= \sqrt{(\lambda_1 l)^2 + (\lambda_2 r\theta^*)^2} \\
s &= s\sqrt{\lambda_1^2(\cos(\alpha))^2 + \lambda_2^2(\sin(\alpha))^2(\frac{\theta^*}{\theta})^2} \\
\lambda_1^2(\cos(\alpha))^2 &+ \lambda_2^2(\sin(\alpha))^2(\frac{\theta^*}{\theta})^2 = 1
\end{aligned} \tag{2.1}
$$

Figure 2.3(a) shows the relationship between fiber rotations (θ), fiber angle (α), length (l), and radius(r); this equation is expressed in Eq. 2.2.

$$
\theta = \frac{\tan(\alpha) l}{r} \tag{2.2}
$$

2.2.2 Families of Fibers

When two families of fibers are used to constrain a FREE, the kinematics of the fiber deformation dictate the relationship between the radial expansion (λ_2) and the axial extension (λ_1) and between the rotation (δ) and axial extension (λ_1). With both of these relationships understood, the pitch (p) is also derived. Equation 2.1 is rewritten using the understanding that $\theta^* = \theta + \delta$; this is shown for both fiber angles, α and β, in Eq. 2.3

$$
\begin{aligned}
\lambda_1^2(\cos(\alpha))^2 &+ \lambda_2^2(\sin(\alpha))^2(\frac{\theta+\delta}{\theta})^2 = 1 \\
\lambda_1^2(\cos(\beta))^2 &+ \lambda_2^2(\sin(\beta))^2(\frac{\theta+\delta}{\theta})^2 = 1
\end{aligned} \tag{2.3}
$$

Substituting θ from Eq. 2.2 into Eq. 2.3 provides Eq. 2.4, which shows how λ_2 (the radial expansion) is a function of the angles α and β and the axial expansion λ_1. Equation 2.5 shows how δ (the rotation caused by actuation) is a function of α, β, and λ_1, as well as the length and radius of the FREE. Equation 2.4 is derived by setting δ to be equal for both families of fibers in the actuated state; Equation 2.5 uses the same method, except setting λ_2 to be equal for both families. Both of these equations assume that the length of the fiber remains constant and does not buckle. Relaxation of this assumption is explored in Chapter 3.

$$\lambda_2 = \frac{\frac{|\beta|}{\beta}\cos(\alpha)\sqrt{1-(\cos(\beta))^2\lambda_1^2} - \frac{|\alpha|}{\alpha}\cos(\beta)\sqrt{1-(\cos(\alpha))^2\lambda_1^2}}{\sin(\alpha-\beta)} \tag{2.4}$$

$$\delta = \frac{l}{r}\frac{\frac{|\beta|}{\beta}\sin(\alpha)\sqrt{1-\lambda_1^2(\cos(\beta))^2} - \frac{|\alpha|}{\alpha}\sin(\beta)\sqrt{1-\lambda_1^2\cos(\alpha)^2}}{\frac{|\alpha|}{\alpha}\cos(\beta)\sqrt{1-\lambda_1^2(\cos(\alpha))^2} - \frac{|\beta|}{\beta}\cos(\alpha)\sqrt{1-\lambda_1^2(\cos(\beta))^2}} \tag{2.5}$$

For most configurations, a well-defined relationship exists between the axial stretch and rotation, referred to as the pitch. This implies that the general form of deformation for these geometries is a *screw* motion. For small deformations about its initial configuration, the pitch is defined as Eq. 2.6. For FREEs with a single family of fibers ($\alpha = \beta$) and those that cause fiber buckling, this relationship does not hold, as the equation is indeterminate, and the pitch is dictated by the elastomer stiffness.

$$\begin{aligned} p &= \lim_{\lambda_1 \to 1} \frac{l d\lambda_1}{d\delta} \\ p &= \frac{r\sin(\alpha)\sin(\beta)\sin(\alpha-\beta)}{(\sin(\alpha))^2 - (\sin(\beta))^2} \end{aligned} \tag{2.6}$$

Figure 2.4 plots the screw pitch equation seen in Eq. 2.6. This shows the screw value (axial change per rotational change) as a function of α and β.

2.2.3 Volume

The volume contained in an unactuated FREE is simply the volume of a cylinder, $V = \pi r^2 l$. As the FREE is actuated, the new volume (V^*) is described using stretch ratios λ_1 and λ_2, shown in Eq. 2.7

$$\begin{aligned} V^* &= \pi(\lambda_2 r)^2(\lambda_1 l) \\ V^* &= \lambda_2^2\lambda_1\pi r^2 l \end{aligned} \tag{2.7}$$

The relationship between the enclosed volume and the axial expansion is shown in Eq. 2.8. This relationship ($dV/d\lambda_1$) is found by differentiating Eq. 2.7 at the undeformed position ($\lambda_1 = 1$), and substituting in Eq. 2.4. The equation again uses the assumption that the fibers do not buckle, which is addressed further in Chapter 3.

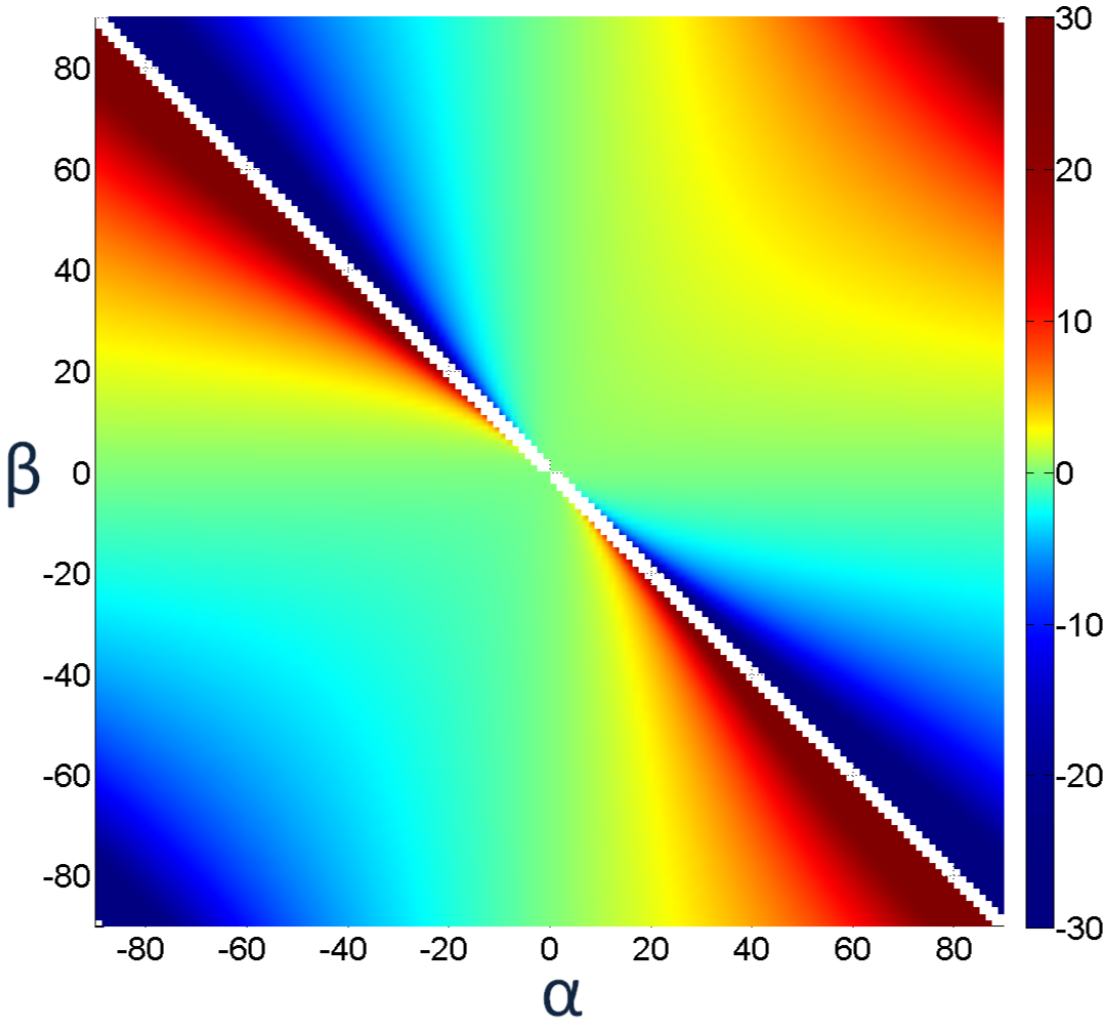

Figure 2.4: Pitch of the deformation of a FREE under increasing volume. Positive values indicate a left-hand screw, while negative values are a right-hand screw. Pitch is in $\frac{mm}{rad}$. Radius is set at 6mm. Plot is clipped (cut off at a threshold value) at ± 30.

$$\lim_{\lambda_1 \to 1} \frac{dV}{d\lambda_1} = (1 + 2\cot(\alpha)\cot(\beta))\pi r^2 l \tag{2.8}$$

2.3 Experimental Method

An experiment was run to validate the model of the deformation pitch. A detailed understanding of the variables and parameters of the experiment are explored in Section 2.3.1. The physical experimental setup is detailed in Section 2.3.2. Section 2.3.3 explains the experimental procedure, including the points tested.

2.3.1 Variables and Parameters

Half of the design space is redundantly labeled (e.g. $\alpha = 60°$, $\beta = 40°$ is the same configuration as $\alpha = 40°$, $\beta = 60°$ with the fiber labels switched). The design space of angle configurations is also symmetric about the $\alpha = -\beta$ line, leading to axial displacements that are equal, and rotations that are equal in magnitude and opposite in direction. For example, the axial displacement for $\alpha = 30°$, $\beta = 70°$ is the same as for $\alpha = -30°$, $\beta = -70°$, while the rotation about the axial direction of the later are equal in magnitude and opposite in direction to the former. An experiment was conducted to investigate the effect of helix angles α and β on the output variable of pitch, derived from the axial displacement and rotation generated about the axis. The radius parameter of the FREE actuators is fixed at 6 mm.

2.3.2 Experimental Setup

The test setup, shown in Figure 2.5, was used to measure the pitch of the FREE deformation. The rotational displacement was measured by a rotational optical encoder (US Digital H5-1250-NE-S 1250 CPR single ended ball bearing encoder). The linear displacement was measured with a linear encoder (US Digital EM1-0-250-N 250 LPI optical linear encoder, US Digital LIN-250-6-N 250 CPI encoder strip). Displacement measurements were recorded through two US Digital QSB-S Quadrature to USB Adapter boxes. Off-axis effects on each encoder (i.e. rotation on the linear encoder and linear motion on the rotational encoder) were tested prior to experimentation and found to be negligible.

A custom translation-rotation stage was fabricated to hold the encoders in place. Additional custom connections were fabricated to provide a $\frac{1}{8}$ NPT tapped hole connecting the

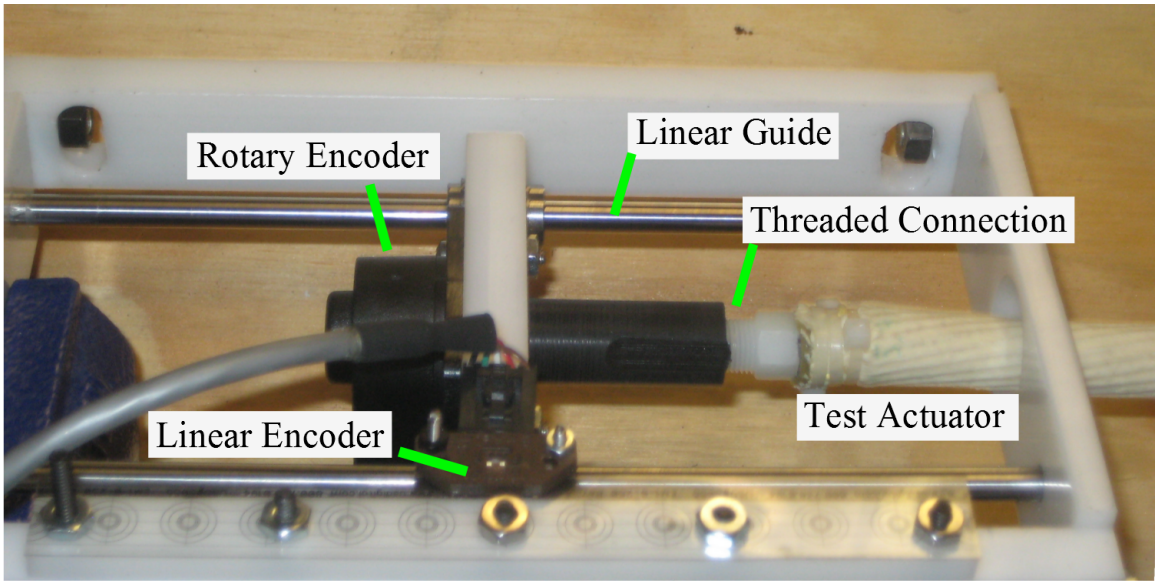

Figure 2.5: Image of experimental setup for pitch measurement with key components labeled.

actuator being tested to the encoder on one end and to the air inlet and pressure measurement on the other. The pressure was controlled manually from a regulated air compressor (Rigid 5-in-1 dual tank). A visual pressure gauge was attached to help with experimentation. The encoder setup and the pressure setup were fixed to a rigid surface using mounted clamps.

2.3.3 Experimental Procedure

The actuator for each test was installed by setting the distance between the threaded connections at the actuator's deflated length. The actuator was screwed into the threaded connection. The ends were tightened enough to ensure that there was no freedom to rotate, thus acting as fixed constraints. The pressure was manually adjusted and held at numerous pressures up to the maximum safe pressure each actuator could withstand without failing (maximum pressure ranged from 100 to 275 kPa for the different actuators). Five sweeps were made from zero to maximum pressure to zero pressure, with measurements taken in each sweep.

As described in Section 2.3.1, this experiment investigated the effect of α and β on the screw pitch. Only a quarter of this design space requires testing to investigate all α and β combinations. A checkerboard pattern of 45 α and β combinations were selected for experimental testing, with the chosen values shown in Figure 2.6. Test points very near the $\alpha = \beta$ line were not considered, as $\alpha = \beta$ points are degenerate cases that are

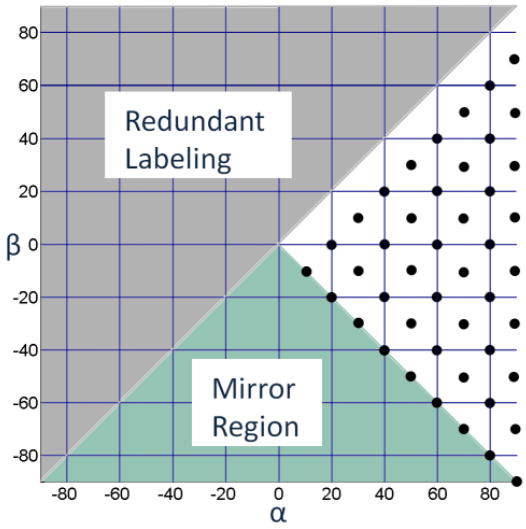

Figure 2.6: α and β points tested are shown as black dots (α and β in degrees). α and β combinations that are mirror images of tested ones are in the bottom region, and α and β combinations that are redundantly labeled are in the top left region.

underconstrained and exhibits much different behavior than surrounding points. These points have an additional degree of freedom, which allows the actuators to inflate in an uncontrolled manner until failure.

2.4 Experimental Results

The direct data from the experimental tests was processed to understand the kinemtic motion across the entire design space. This data processing is explored in Section 2.4.1. The resulting experimental screw pitch is shown in Section 2.4.2. Comparisons of the experimental results to the kinematic model are explored in Section 2.4.3

2.4.1 Data Processing

The ratios of the axial to rotational displacement measurements were highly linear for nearly all tests. Errors created by friction in the measurement equipment were normalized by increasing and decreasing pressure symmetrically. The resulting pitch ($\frac{axial\ displacement}{rotational\ displacement}$) was calculated for all tests, and these values were used for comparison across α and β values. The full pitch plot was obtained by taking the negative of the values mirrored across the $\alpha = -\beta$ line then mirroring the values across the $\alpha = \beta$ line.

A high resolution image was created from the data points by first interpolating the checkerboard pattern (seen in Figure 2.6) to a full grid of points spaced every 10° using a

cubic interpolation. This grid of points was then cubicly interpolation to obtain a final high resolution grid (every $1.25°$) of screw pitch values.

2.4.2 Experimental Screw Pitch

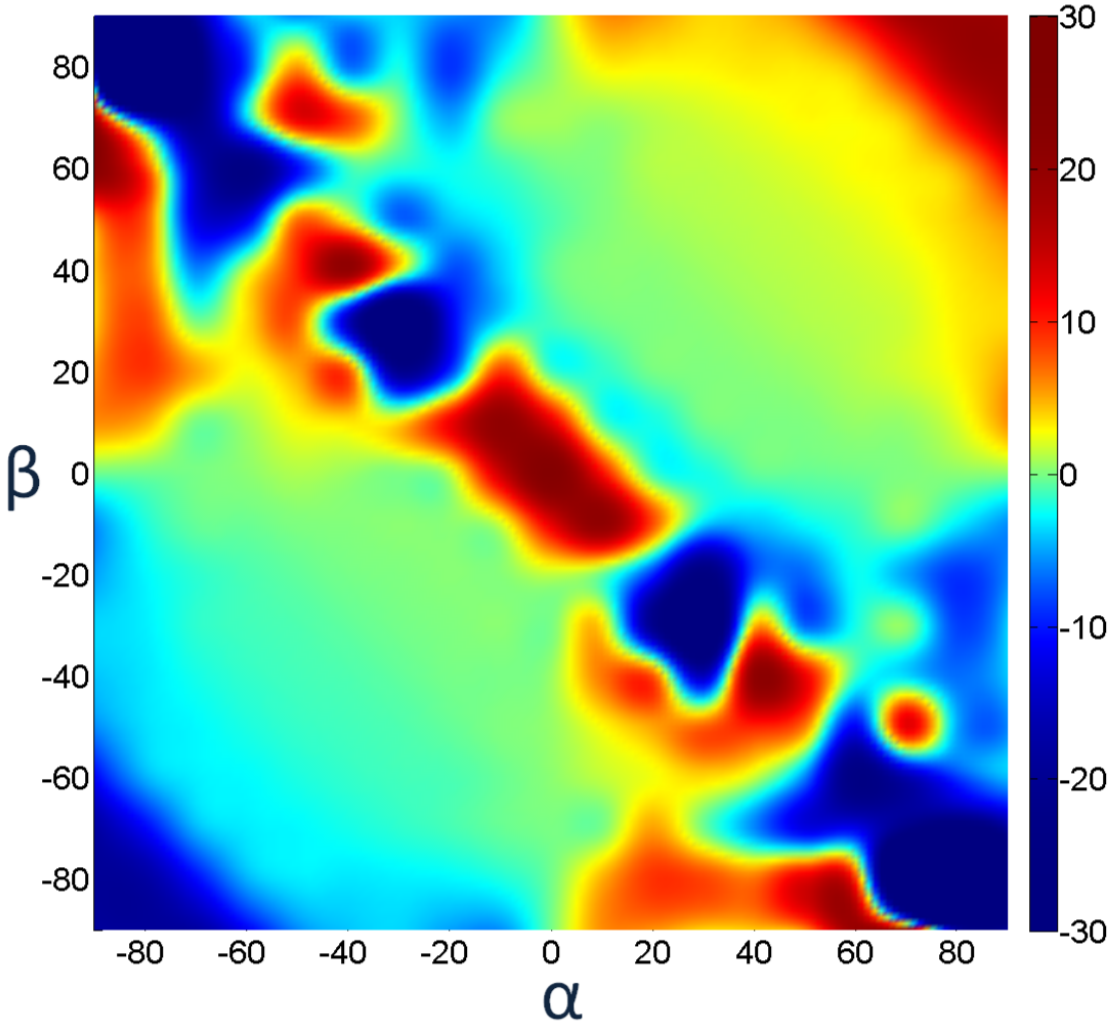

Figure 2.7: Experimental pitch of the deformation of a FREE under increasing volume. Positive values indicate a left-hand screw, while negative values are a right-hand screw. Pitch is in $\frac{mm}{rad}$. Radius is fabricated at 6mm. Plot is clipped at ± 30.

The resulting screw pitch is shown in Figure 2.7. The regions near the $\alpha = -\beta$ line show very high pitch values, indicating mostly translation motion, with minimal rotation. While these values switch between high positive and high negative values, both indicate a primarily translation motion, since pitch values asymptotically approach $\pm$infinity for pure translation. A pitch of 0 indicates pure rotation which is plotted in green. As the fiber

angles approach either $\alpha = -\beta$ or $\alpha = 90°$, $\beta = 90°$ the pitch gets larger in magnitude (more translation per rotation).

2.4.3 Comparison of Experimental to Predicted Pitch

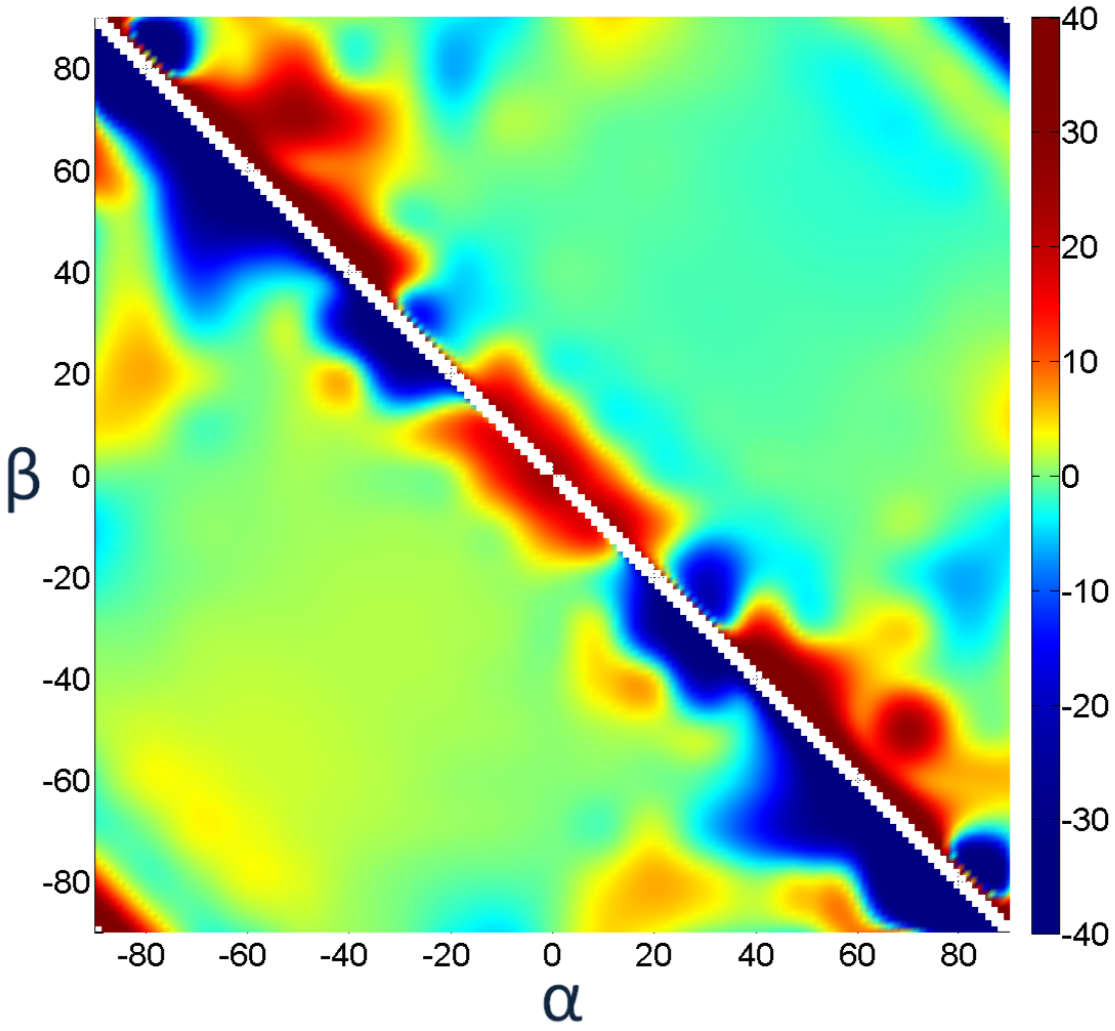

Figure 2.8: Residual error measured as difference between pitch of experimental and predicted deformations. Residual measured in $\frac{mm}{rad}$ and clipped at ± 40.

The first method to compare the experimental pitch presented in Section 2.4.2 to the modeled pitch is to observe residual pitch (difference between experimental results and model). The difference is also expressed as the percent error between the experimental and modeled values. Figure 2.8 shows the residual pitch value (experimental-model). Figure 2.9 shows the absolute percent error of the pitch values ($|\frac{experimental-model}{model}|$).

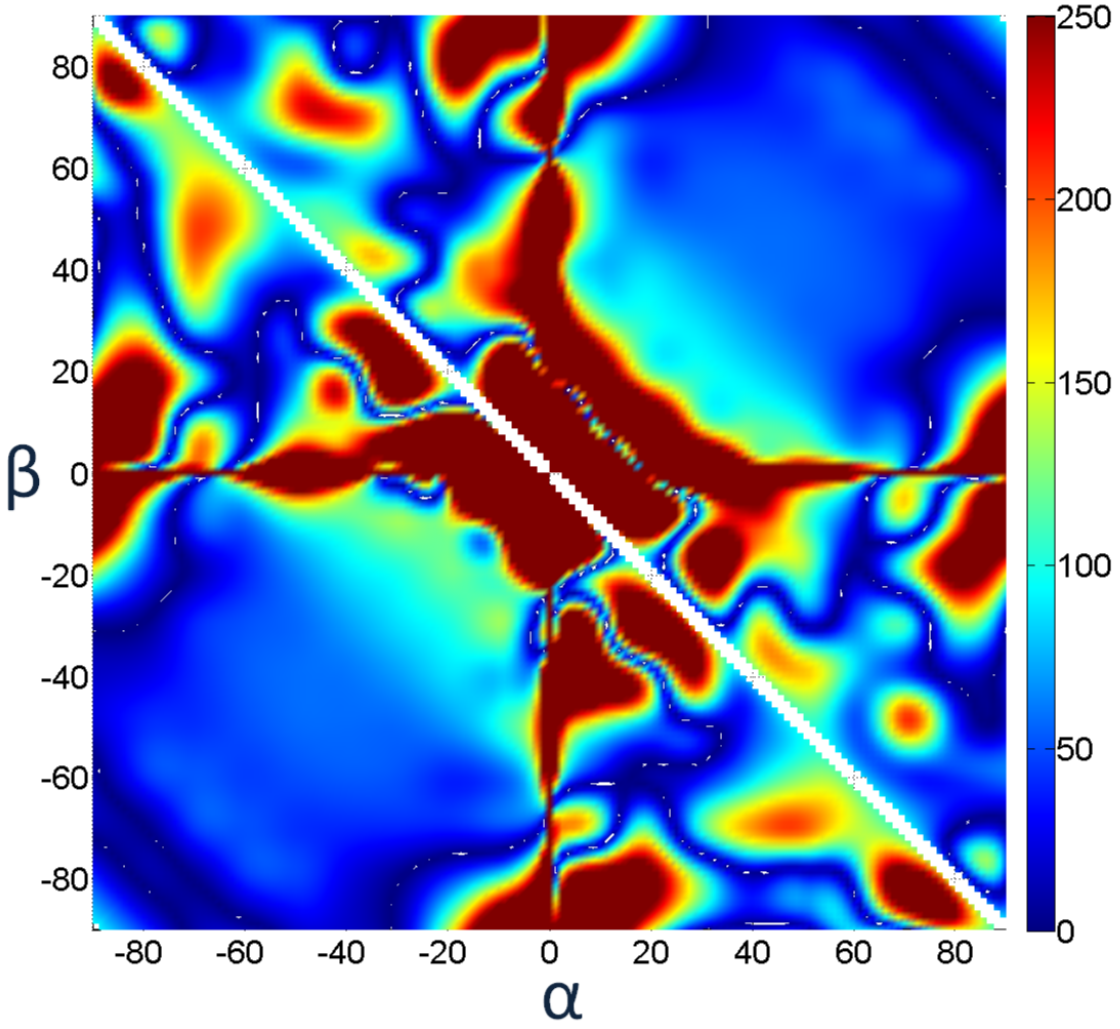

Figure 2.9: Percent error measured as the absolute value of the difference between pitch of experimental and modeled screw pitch, all over modeled value ($|\frac{experimental-model}{model}|$). Error shown in percent (%) and clipped at 250%.

These comparisons present a designer with an understanding of the error in the model. The plots are limited in their utility as the coordinate system presents asymptotic results. Pitch values that represent pure translation are infinite, and configurations with fiber angles close to pure translation have very high pitch values, so any nominal rotation causes a very large error in pitch. Configurations producing nearly pure rotation values have a modeled pitch of close to zero, thus any nominal translation cause very large percentage errors in pitch, as the denominator of the error fraction is near zero.

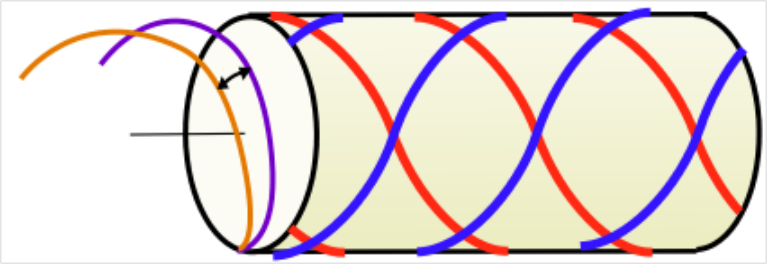

Figure 2.10: Visualization of the difference in helix angles of two different deformation trajectories. The purple line is one trajectory, while the orange is the other. The arrow shows the difference in the angle between them.

A second method to compare experimental values to predicted ones is to use the helix angle of deformation. This is done by taking $\tan^{-1}(\frac{pitch}{r})$. The helix angle comparison allows motions that are similar, such as primarily translation with small rotation in either direction, to result in similar values. The devices were all fabricated at the same radius, further removing any error from using this conversion. The helix angle measurement can also be visualized as observing the relative trajectories of a point placed on the cylindrical surface of the FREE. The difference of two helix angles is shown in Figure 2.10, with the trajectories shown in Figure 2.12. The residuals, the difference of the experimental and predicted helix angles from the model, are shown in Figure 2.11 as the difference in helix angle, and in Figure 2.13 as the modeled and experimental tangent vectors. The quadrants of measurements and predictions in Figure 2.11 are set to ensure residuals lie in quadrants 1 or 4. This is done by adding π radians to residuals in quadrants 2 and 3.

Figures 2.11 and 2.13 show discontinuous errors near the line expressed in Eq. 2.9. FREE configurations along this line cannot increase in volume, as the volume is maximized and no motion in any direction expands the volume. FREEs near this region generate small displacement; therefore, any error in motion is very large compared to expected deformation, thus generating discontinuous errors that are large in magnitude. A substantial portion of the design space with small, but consistent non-zero residuals are seen where α and β are both between $0°$ and $54.7°$ or both between $0°$ and $-54.7°$. This is likely due

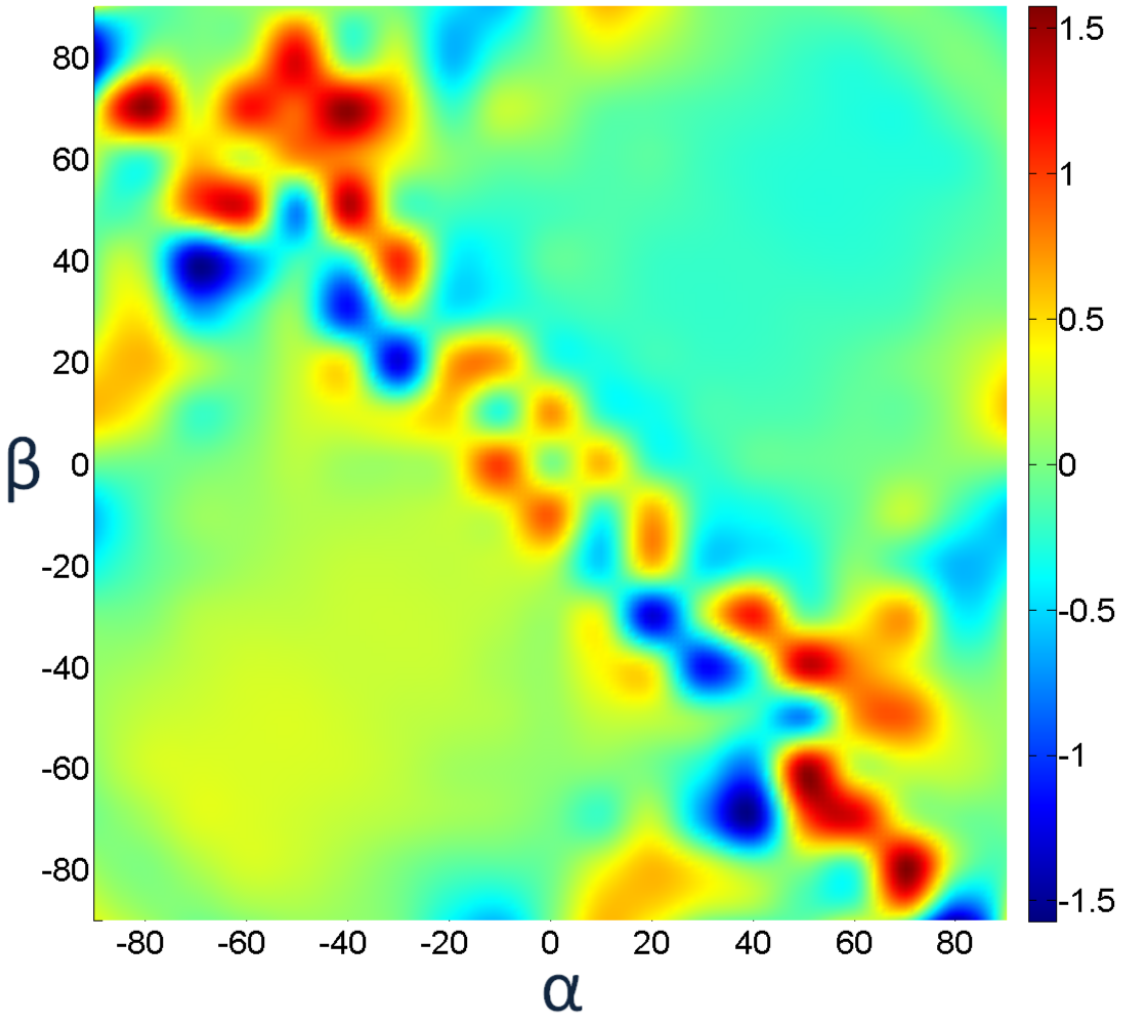

Figure 2.11: Residual error measured as difference between helix angle of experimental and predicted deformations. Quadrants of measurements and predictions are set to ensure residuals lie in quadrants 1 or 4. Residual measured in radians.

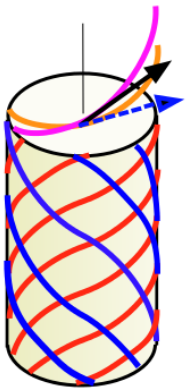

Figure 2.12: Visualization of the difference in helix angles of two different deformation trajectories. The pink line is one trajectory, while the orange is the other. The black arrow shows the vector tangent to the pink helical trajectory, while the dashed blue line shows the vector tangent to the orange trajectory.

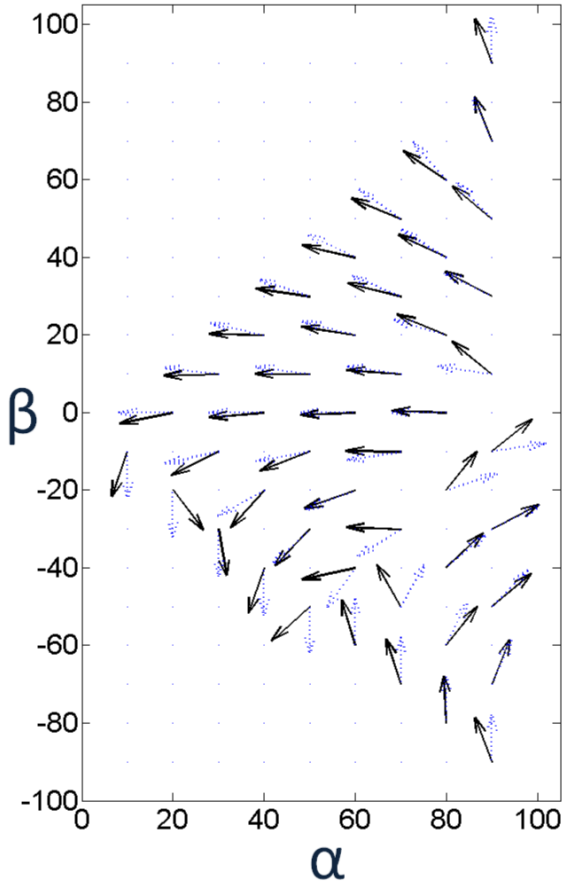

Figure 2.13: The tangent vector to the experimental and predicted helical deformations. The dotted line is the predicted tangent vector, while the solid line is the experimental.

to one of the families of fibers buckling, creating an underconstrained deformation that follows different equations than those in the model that does not consider buckling. This phenomenon and the significance of the -54.7° angle are explored in Chapter 3. Outside of these regions, the experimental pitch aligned closely with the predicted values.

$$\alpha = \cot^{-1}(\frac{-1}{2\cot(\beta)}) \tag{2.9}$$

2.5 Summary

This chapter presented an understanding of how the configuration of the fibers in a fiber-reinforced elastomeric enclosure (FREE) effect the deformation kinematics. The axial and radial expansion, rotation, volume change, and pitch are derived from the angles of the two families of fibers, α and β, and the unactuated radius and length. A pitch plot was created to provide an easy design tool for the synthesis of FREEs with desired deformation motion. The pitch model was tested across the entire design space of FREEs with two families of fibers, showing good agreement between the model and the experimental data.

CHAPTER 3

Volumetric Transduction

The volumetric transduction is defined here as the ratio between the motion of FREE output and the change in enclosed volume. The volumetric transduction is important both for controlling the displacement of FREEs and for providing an indication of relative stiffness values of the FREE in the actuated and unactuated directions. This stiffness is seen in the link between the output displacement and the volume that is held in by the elastomer surface, thus the fibers and fluid act as a virtual lever on the elastomer. The modeling of the volumetric transduction continues from the kinematics models explored in Chapter 2. There are three displacement categories that are considered:

1. Axial extension and compression, in Section 3.1
2. Clockwise and counter-clockwise rotation about the axial direction, in Section 3.2
3. Screw motion with either clockwise or counter-clockwise components combined with either extension or compression components, in Section 3.3

The final section of this chapter, Section 3.4, describes how the mobilities of all FREEs in the design space are discretized and mapped.

3.1 Axial Extension and Compression

The volume change per change in λ_1 (axial deformation) was shown to be $dV/d\lambda_1$ from Eq. 2.8. To examine only axial displacements and not screw motion containing axial motion, the rotation is locked at zero ($\delta = 0$). The resulting equation is shown in Eq. 3.1. For a single family of fibers in elongation ($\lambda_1 > 1$), $dV/d\lambda_1$ is taken directly, while for compression ($\lambda_1 < 1$) the negative of the $dV/d\lambda_1$ is used, as motion in the opposite direction has an equal and opposite effect on the volume for a single family of fibers.

$$\lambda_1^2(\cos(\alpha))^2 + \lambda_2^2(\sin(\alpha))^2(\frac{\theta^*}{\theta})^2 = 1$$
$$\delta = 0 \implies \theta^* = \theta \implies \frac{\theta^*}{\theta} = 1$$
$$\lambda_1^2(\cos(\alpha))^2 + \lambda_2^2(\sin(\alpha))^2 = 1$$
$$-\lambda_1^2(\cot(\alpha))^2 + (\csc(\alpha))^2 = \lambda_2^2$$
$$V^* = \lambda_2^2\lambda_1\pi r^2 l$$
$$-\lambda_1^2(\cot(\alpha))^2 + (\csc(\alpha))^2 = \frac{V^*}{\lambda_1\pi r^2 l}$$
$$V^* = ((\csc(\alpha))^2\lambda_1 - (\cot(\alpha))^2\lambda_1^3)\pi r^2 l$$
$$\lim_{\lambda_1\to 1}\frac{dV}{d\lambda_1} = \pi r^2 l((\csc(\alpha))^2 - 3(\cot(\alpha))^2)$$
$$\lim_{\lambda_1\to 1}\frac{dV}{d\lambda_1} = \pi r^2 l(1 - 2(\cot(\alpha))^2) \tag{3.1}$$

For FREEs with two families of fibers (other than for McKibben configurations of $\alpha = -\beta$), under the $\delta = 0$ condition, change in volume with respect to λ_1 is different for the two families of fibers. The family of fibers are assumed to lay on the same FREE radius as each other, thus the family of fibers that causes less decrease in volume (or a greater increase in volume) has excess fiber length if placed on the same radius as the other fiber family. This excess length causes the family of fibers to be in compression, buckle, and not affect the volume change. Fiber inextensibility prevents the other family of fibers from increasing in radius. External extension has different fiber angles in this buckled state than external compression has, leading to different behavior under extension and compression.

A fiber angle of approximately $54.74°$ has a volume change per axial extension of zero when the rotation is fixed. Higher fiber angles experience increasing volume and lower angles experience decreasing volume, with $54.74°$ serving as the transition angle. This phenomenon can be seen from Eq. 3.1. Figure 3.1 shows the volume change under extension for two families of fibers. This plot shows that for regions with fibers that are both far from axial ($|\alpha| > 54.74°$ and $|\beta| > 54.74°$), volume increases under axial extension. The maximum volume increase is proportional to πr^2, while the maximum volume decrease in other regions is theoretically infinite, though it is clipped in the figure for clarity. The dual diagonal symmetry of the plot indicates that a simple comparison of fiber angles determines which family of fibers drives the volume change. For axial extension the fiber angle closer to the axial direction acts as the driver. Figure 3.2 shows the volume change under compression for two families of fibers. Compression (Figure 3.2) presents a different

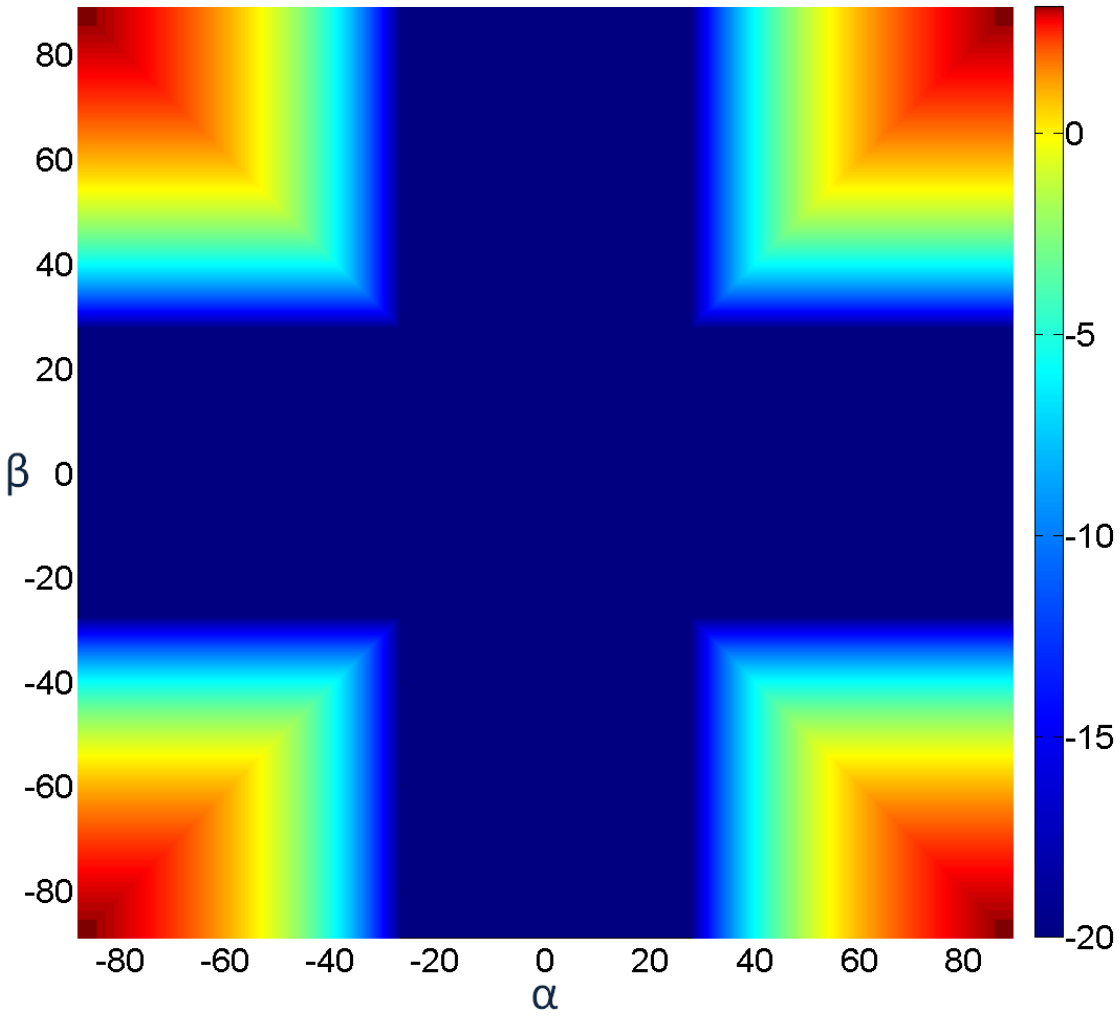

Figure 3.1: Volume change per unit motion in extension across α and β (in degrees). Plot is clipped below at -20. Radius is set to 1 and plot is normalized for length.

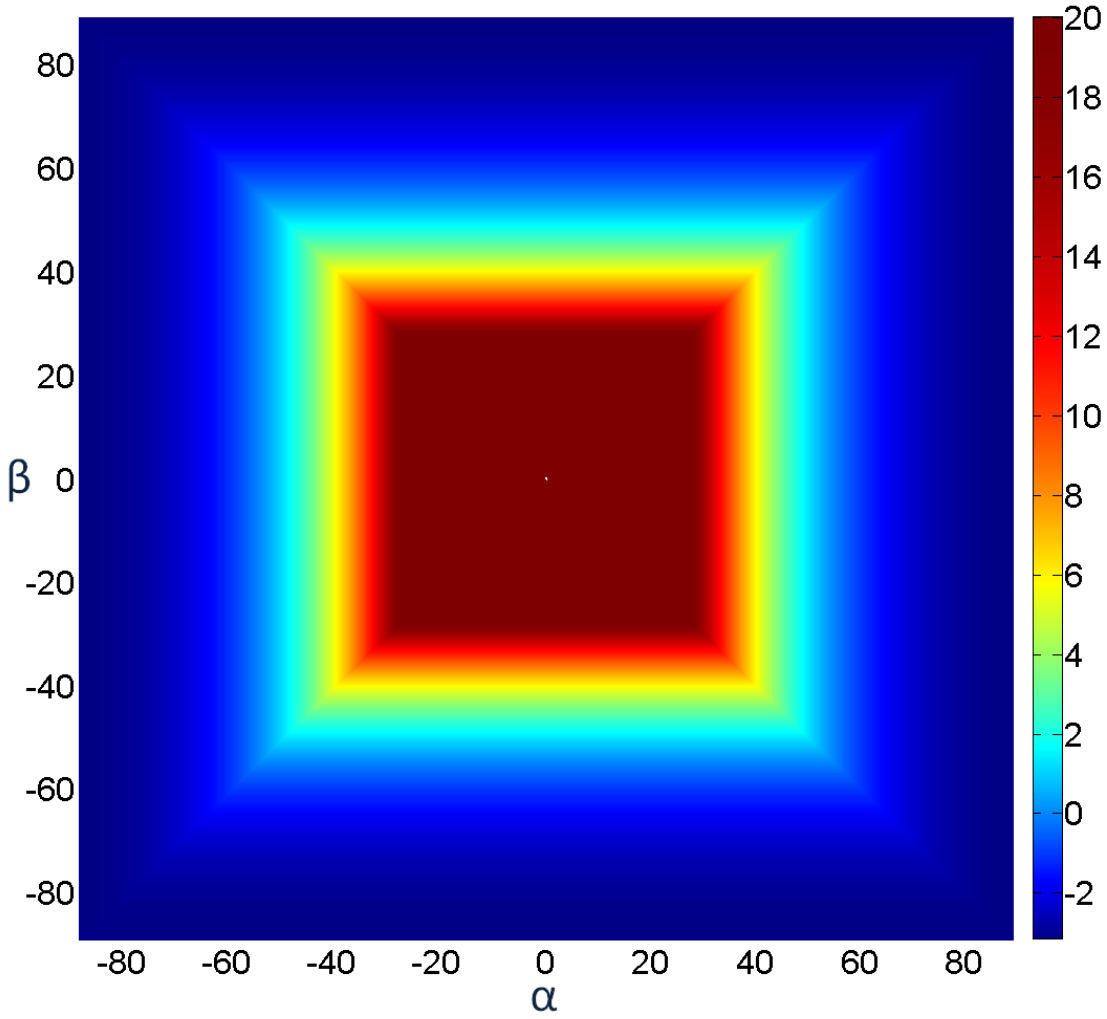

Figure 3.2: Volume change per unit motion in compression across α and β (in degrees). Plot is clipped above at 20. Radius is set to 1 and plot is normalized for length.

behavior than extension (Figure 3.1), as the volume change for compression is not simply the negative of volume change for extension when two families of fibers are used. Regions with both families of fibers near axial ($|\alpha| < 54.74°$ and $|\beta| < 54.74°$) experience volume increase, while all other regions decrease in volume, with the fiber angle further from axial driving volume change.

3.2 Rotation

The volume change per change in δ (rotation about the axial direction) is $dV/d\delta$. To examine only rotational displacements and not screw motions containing rotation, the extension is locked at the initial length ($\lambda_1 = 1$). The resulting equation is shown in Eq. 3.2. When the two sets of fibers are combined, the fiber angle causing the greatest drop in fluid volume (or smallest increase) drives the volume change, as the other fiber set is in compression, buckle, and not affect the volume change. For counter-clockwise (CCW) rotation ($\delta > 0$), $dV/d\delta$ is taken directly, while for clockwise (CW) rotation ($\delta < 0$), the negative of the $dV/d\delta$ is taken. $dV/d\delta$ for CCW rotation is shown in Figure 3.3, while $dV/d\delta$ for CW rotation is shown in Figure 3.4.

$$
\begin{aligned}
&\lambda_1^2(\cos(\alpha))^2 + \lambda_2^2(\sin(\alpha))^2(\frac{\theta^*}{\theta})^2 = 1 \\
&\lambda_1 = 1 \implies (\cos(\alpha))^2 + \lambda_2^2(\sin(\alpha))^2(\frac{\theta^*}{\theta})^2 = 1 \\
&\lambda_2^2 = \frac{1-(\cos(\alpha))^2}{(\sin(\alpha))^2(\frac{\theta+\delta}{\theta})^2} = \frac{(\sin(\alpha))^2}{(\sin(\alpha))^2(\frac{\theta+\delta}{\theta})^2} \implies \lambda_2^2 = (\frac{\theta}{\theta+\delta})^2 \\
&V^* = \lambda_2^2\lambda_1\pi r^2 l = \lambda_2^2\pi r^2 l = (\frac{\theta}{\theta+\delta})^2\pi r^2 l \\
&\theta = \frac{\tan(\alpha)l}{r} \implies V^* = \frac{\pi l^3(\tan(\alpha))^2}{(\frac{l\tan(\alpha)}{r}+\delta)^2} \\
&\lim_{\delta\to 0}\frac{dV}{d\delta} = -\frac{2\pi l^3(\tan(\alpha))^2}{(\frac{l\tan(\alpha)}{r}+0)^3} = -2\pi r^3\cot(\alpha)
\end{aligned}
\tag{3.2}
$$

Figure 3.3 shows the applied rotation causing different volume change patterns in each quadrant. Quadrant 1 has fibers wrapped with rotation in the opposite direction to the applied rotation, causing the volume to increase under deformation. The larger of the fiber angles (further from axial) limits the volume increase in this quadrant. Quadrant 3 has fibers wrapped with rotation in the same direction as the applied rotation, causing the volume to decrease under deformation. The smaller fiber angle (closer to axial) drives the

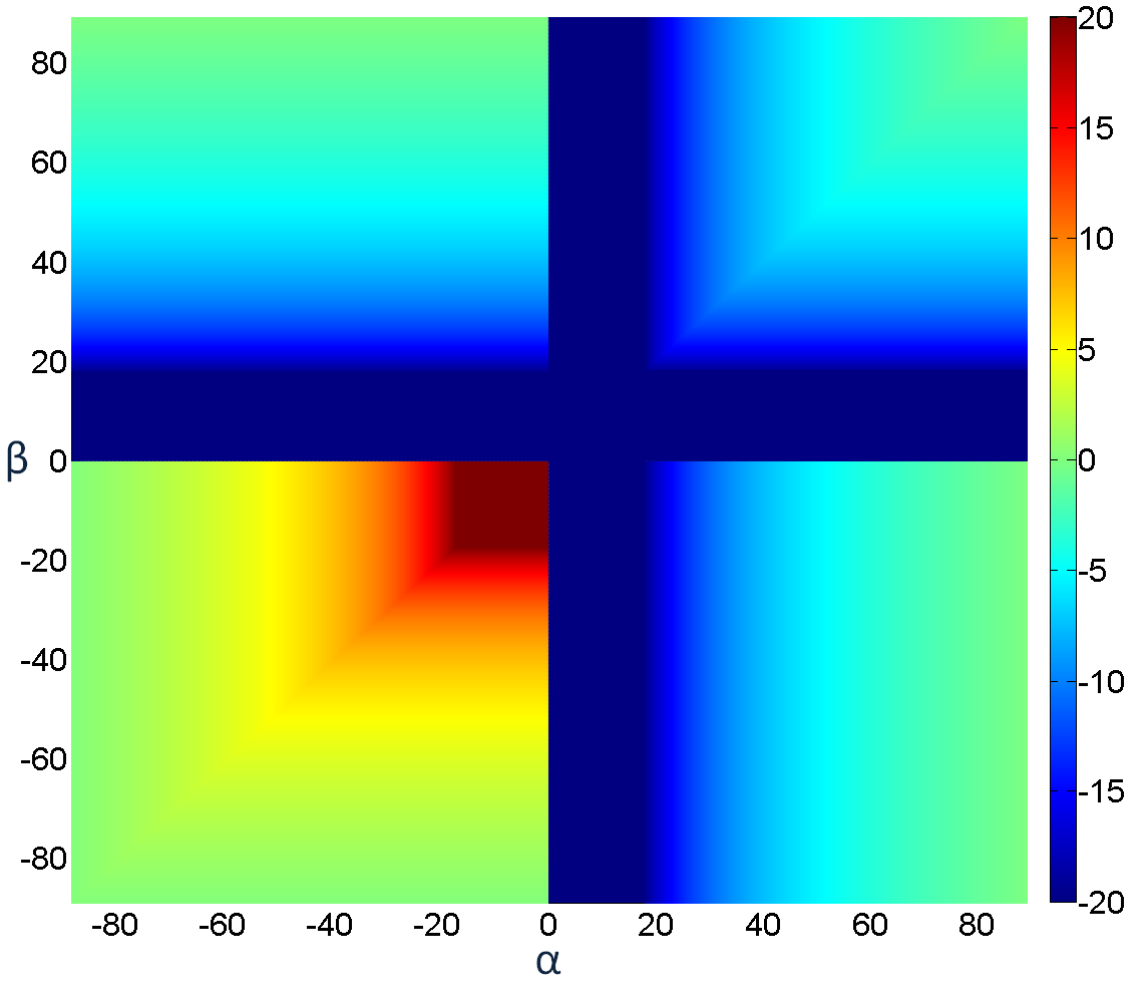

Figure 3.3: Volume change per radian of counter-clockwise rotation across α and β (in degrees). Plot is clipped at $\pm$ 20. Radius is set to 1 and plot is normalized for length.

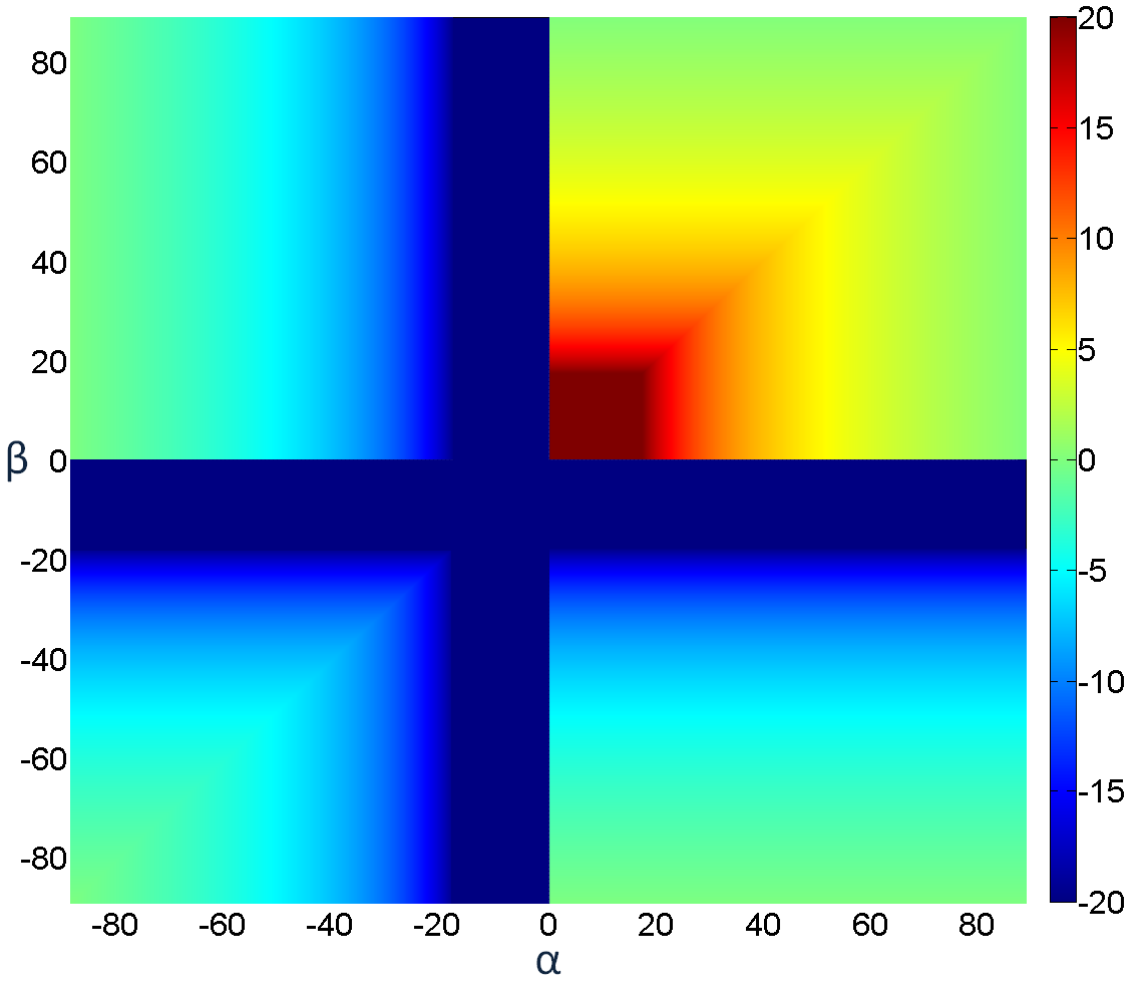

Figure 3.4: Volume change per radian of clockwise rotation across α and β (in degrees). Plot is clipped at $\pm$ 20. Radius is set to 1 and plot is normalized for length.

volume change. Quadrants 2 and 4 have one fiber family wrapped with rotation in the same direction as the applied rotation and the other in the opposite rotation, thus the volume is driven by the fiber with rotation in the same direction as the applied rotation, causing a decreasing volume. Figure 3.4 (CW rotation), is derived from the same analysis, but with opposite volume effects from each family of fibers, thus the figure is the mirror of Figure 3.3 about the $\alpha = -\beta$ line.

3.3 Screw Translation

Output motions that are screw motions (coordinated axial displacement and rotation) has differing effects on the volume of the FREE based on their screw path (S_{app}), which can be described using the pitch, denoted here as p_{app}. This pitch represents the proportion of the axial displacement to the rotational displacement being exerted on the FREE. This pitch is independent of, and in most cases different than, the actuation pitch of a FREE described in Eq. 2.6. The volume change per motion in a specified screw path, dV/dS_{app}, is shown in Eq. 3.3. The displacement along the path S_{app} is the arc length of the travel of a point on the surface (at the radius) of the FREE. dV/dS_{app} for screw motions with counter-clockwise (CCW) rotation and axial extension is shown in Figure 3.5. The absolute value for these screw motions is shown in Figure 3.6.

$$
\begin{aligned}
pnorm &= \sqrt{1 + r^2 p_{app}^2} \\
\frac{dV}{dS_{app}} &= \frac{r p_{app} \frac{dV}{d\lambda_1} + \frac{dV}{d\delta}}{pnorm} = \frac{r p_{app} \frac{dV}{d\lambda_1} + \frac{dV}{d\delta}}{\sqrt{1 + r^2 p_{app}^2}} \\
\frac{dV}{dS_{app}} &= \frac{r p_{app} \pi r^2 l (1 - 2(\cot(\alpha))^2) - 2\pi r^3 \cot(\alpha)}{\sqrt{1 + r^2 p_{app}^2}} \\
\frac{dV}{dS_{app}} &= \frac{\pi r^3 (l p_{app} - 2(\cot(\alpha))^2 (l p_{app} + 1))}{\sqrt{1 + r^2 p_{app}^2}}
\end{aligned}
\tag{3.3}
$$

There are four independent variables altering the volume change: α, β, extension (λ_1), and rotation (δ). This five-dimensional space determines the directions of maximum volume change, no volume change, and a wide range of positive and negative volume changes. This large space can be reduced to a simplified plot of (α or β) on one axis and p_{app} (or shown here as $ln(p_{app})$) on the other axis. This reduction is possible because the magnitude of deformation in a specified screw pitch (p_{app}) linearly scales the magnitude of the volume change, thus reducing the need for both extension (λ_1) and rotation (δ). Either α or β is

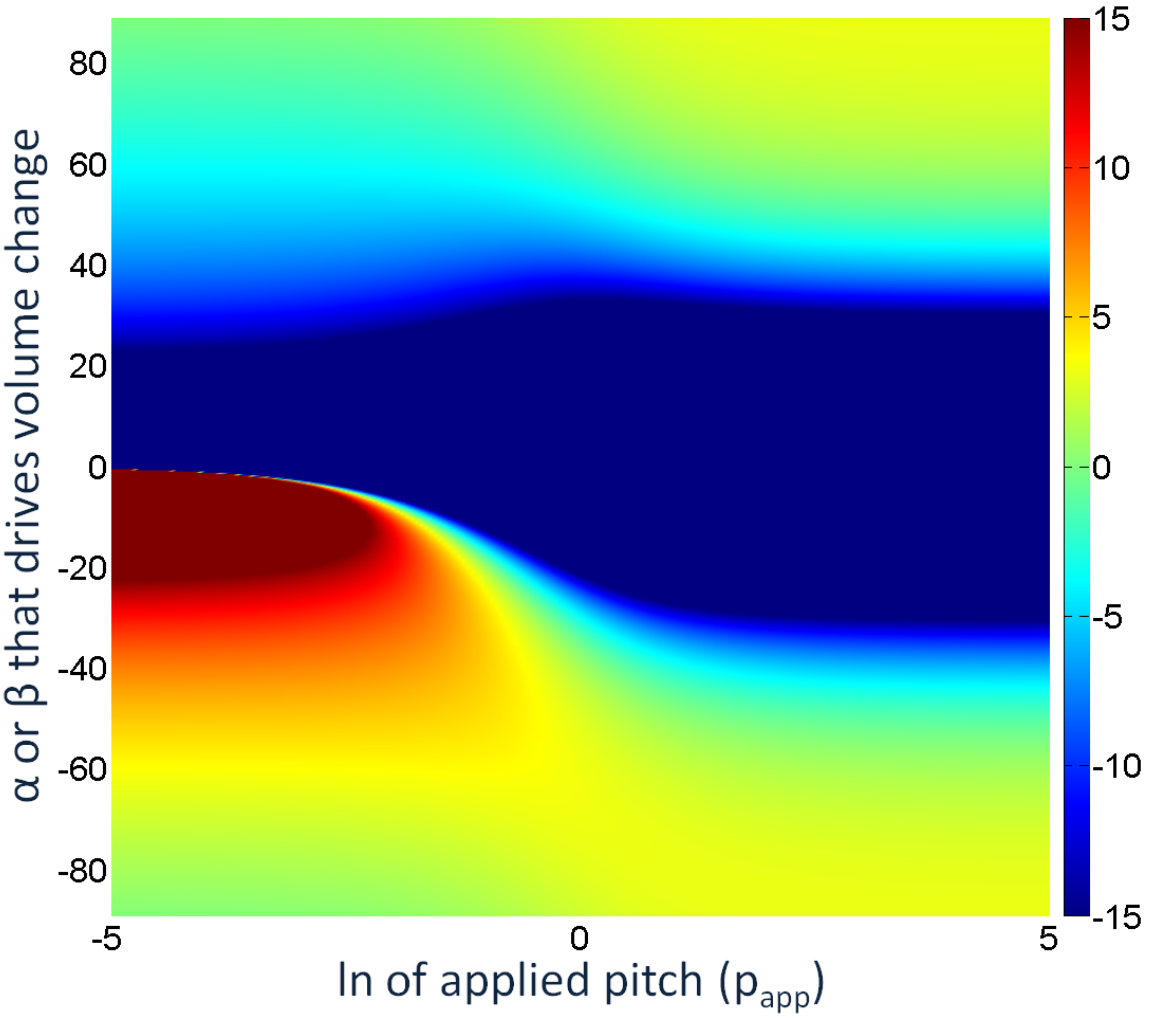

Figure 3.5: Volume change per unit screw motion with counter-clockwise rotation and axial extension across the natural log of applied pitch ($ln(p_{app})$) and the α or β (in degrees) that drives volume change. Plot is clipped at $\pm$ 15. Radius is set to 1 and plot is normalized for length.

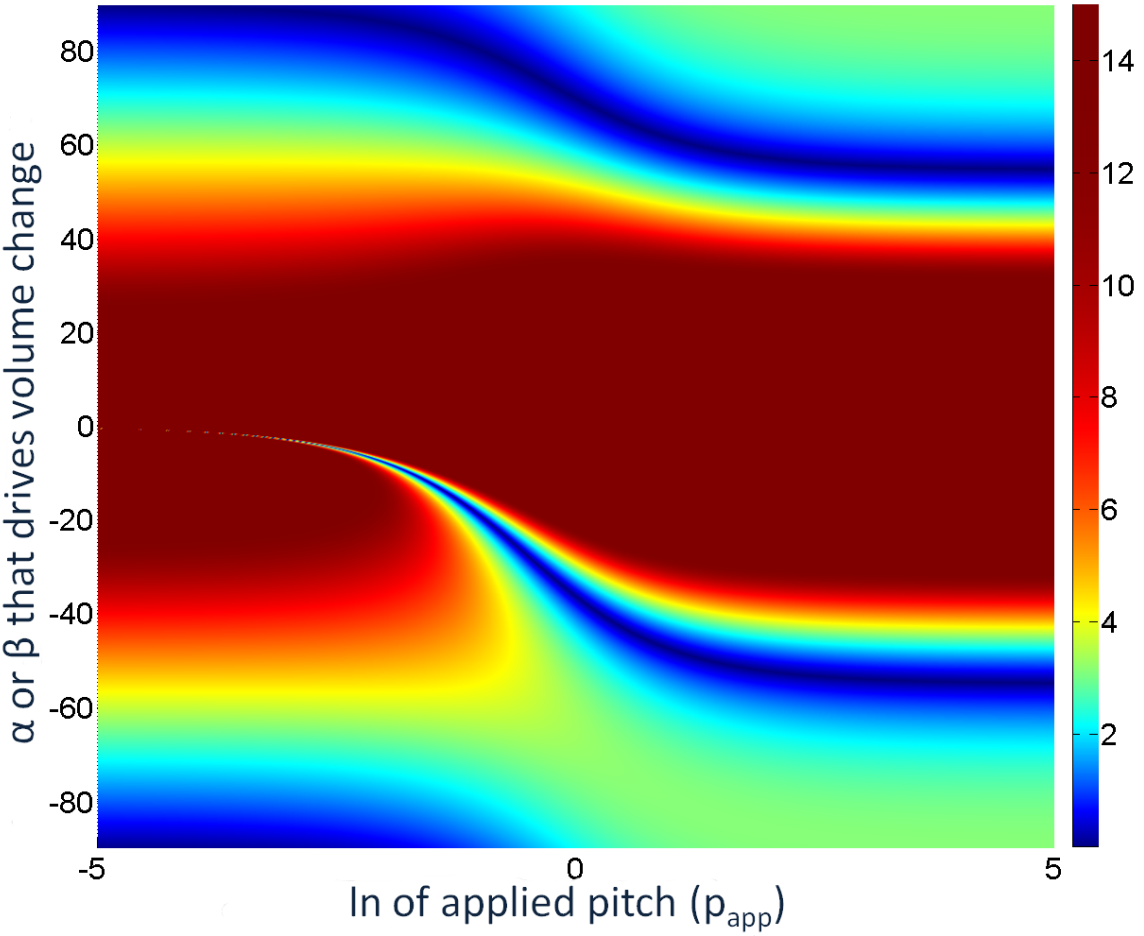

Figure 3.6: Absolute value of volume change per unit screw motion with counter-clockwise rotation and axial extension across the natural log of applied pitch ($ln(p_{app})$) and the α or β (in degrees) that drives volume change. Plot is clipped above at 15. Radius is set to 1 and plot is normalized for length.

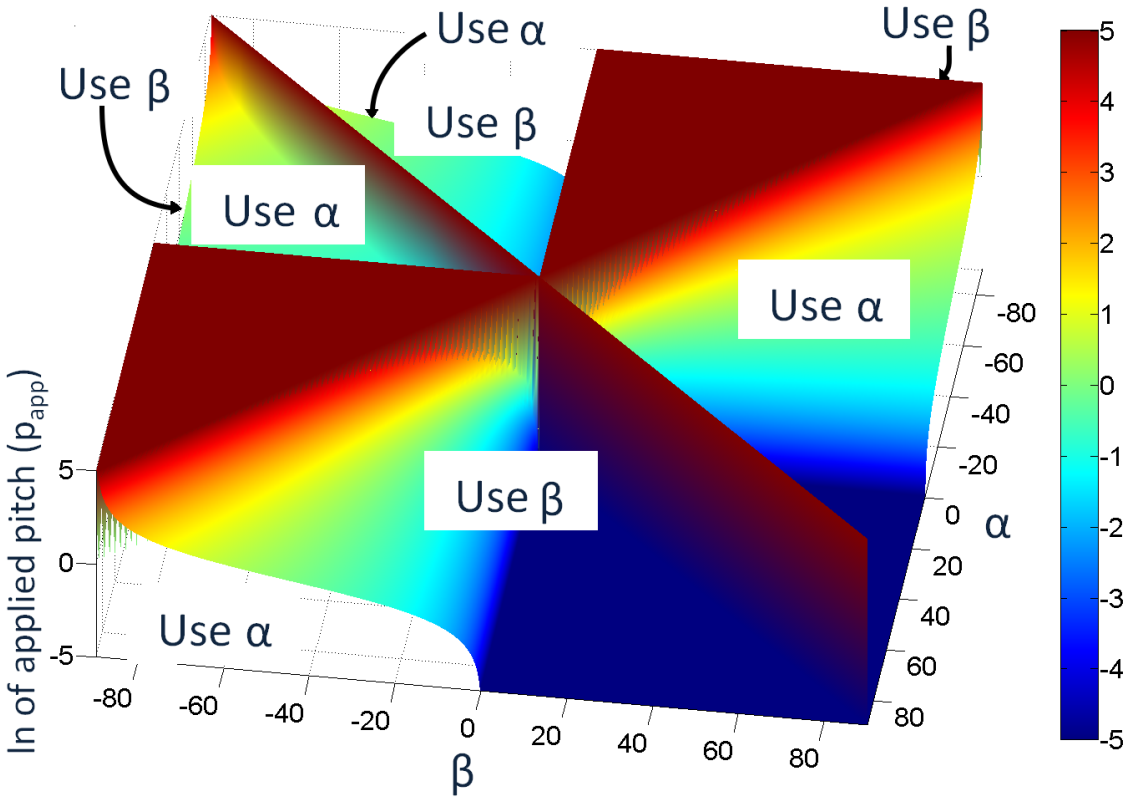

Figure 3.7: Graphical determination of whether α or β (in degrees) is driving volume change under an applied screw with pitch "p_{app}" on a FREE with fiber angles α and β for extending counter-clockwise screws. Plot is clipped at $\pm$ 5. Radius is set to 1.

		α or β to drive dV/dS_{app}	
		α if	β if
extention and CW rotation	$\alpha > \lvert\beta\rvert$	$\lvert p_{app}\rvert < p$	$\lvert p_{app}\rvert > p$
	$\lvert\beta\rvert > \alpha > \beta$	$\lvert p_{app}\rvert > p$	$\lvert p_{app}\rvert < p$
extention and CCW rotation	$\alpha > \lvert\beta\rvert$	$\lvert p_{app}\rvert < -p$	$\lvert p_{app}\rvert > -p$
	$\lvert\beta\rvert > \alpha > \beta$	$\lvert p_{app}\rvert > -p$	$\lvert p_{app}\rvert < -p$
contraction and CW rotation	$\alpha > \lvert\beta\rvert$	$\lvert p_{app}\rvert > -p$	$\lvert p_{app}\rvert < -p$
	$\lvert\beta\rvert > \alpha > \beta$	$\lvert p_{app}\rvert < -p$	$\lvert p_{app}\rvert > -p$
contraction and CCW rotation	$\alpha > \lvert\beta\rvert$	$\lvert p_{app}\rvert > p$	$\lvert p_{app}\rvert < p$
	$\lvert\beta\rvert > \alpha > \beta$	$\lvert p_{app}\rvert < p$	$\lvert p_{app}\rvert > p$

Table 3.1: Determination of whether α or β is driving volume change under an applied screw with pitch "p_{app}" on a FREE with fiber angles α and β. Magnitude of $|p_{app}|$ ($\frac{|ld\lambda_1|}{d|\phi|}$) is compared to p from Eq. 2.6 for each permutation of rotation and axial directions of p_{app} and relevant α to β relationship.

used on the other axis, since one of the families of fibers buckles under the applied screw, causing only a single family to drive the volume change. An additional figure or table describes whether α or β is the family of fibers causing the greatest decrease in fluid volume (or smallest increase), consequently driving the volume change. The family of fibers that causes the greatest decrease in fluid volume depends on α, β, and p_{app}. Figure 3.7 is a plot indicating whether to use α or β for analysis in extending, CCW rotating screws. The plot is used by first locating the α or β of the FREE being analyzed, which determines the X and Y axis location on the plot. Next, the natural log of the applied pitch, $ln(p_{app})$, being exerted on the FREE is found on the Z axis of the plot. The volumetric section of the plot that the X, Y, Z point falls in determines which fiber angle, α or β, drives the volume change, and should consequently be used in the Y axis of Figures 3.5 and 3.6. The use of α or β transitions depending on the screw pitch of the actuation direction (Eq. 2.6) for a given α and β, and Table 3.1 shows which α or β to use for all possible p_{app}. This is an analytical representation of the determination shown graphically in Figure 3.7. Screws that are contracting axially ($\lambda_1 < 1$) modify Eq. 3.3 to use the contraction values for $\frac{dV}{d\lambda_1}$ rather than extension, and these plots are shown in Figures 3.8 and 3.9. dV/dS_{app} for screw motions with extension and CW rotation components is shown in Figure 3.10.

Figure 3.5 shows the large range of volumetric transduction that can be achieved as the screw path, α, and β are altered. The left side of the plot shows a very small pitch, which is approximately pure rotation, while the right side has a very large pitch, which is approximately pure extension. The volume change passes through zero, and Figure 3.6 provides an easy visualization of these regions with no volume change under displacement. These

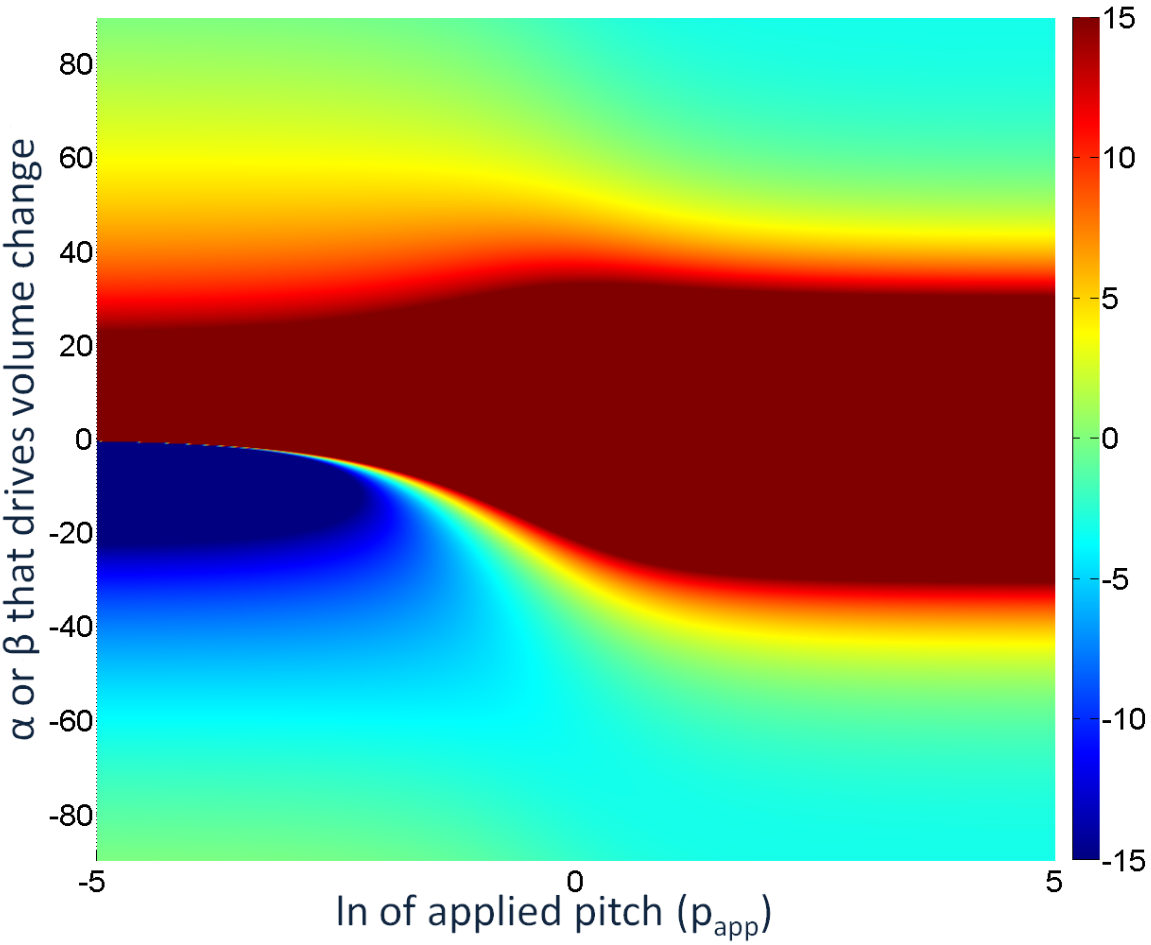

Figure 3.8: Volume change per unit screw motion with clockwise rotation and axial contraction across the natural log of applied pitch ($ln(p_{app})$) and the α or β (in degrees) that drives volume change. Plot is clipped at $\pm$ 15. Radius is set to 1 and plot is normalized for length.

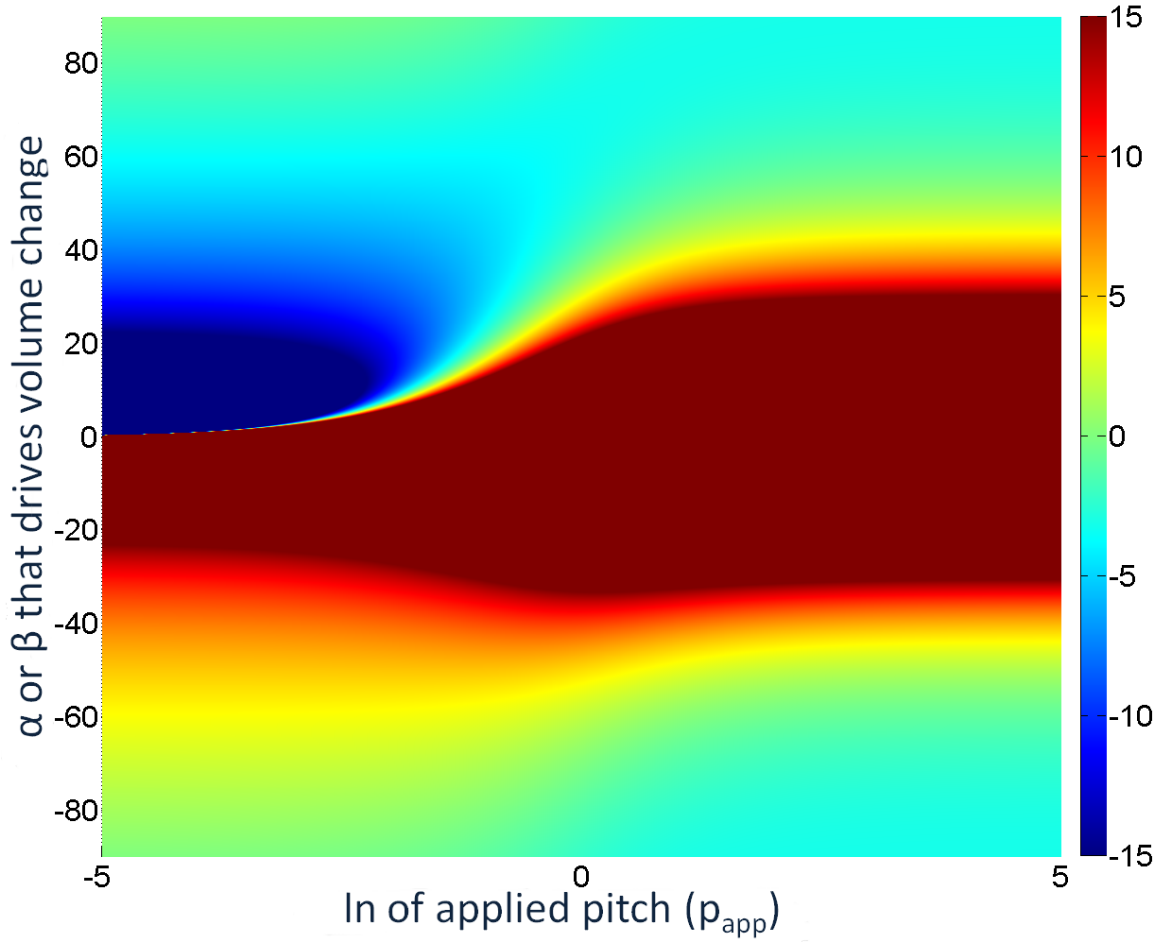

Figure 3.9: Volume change per unit screw motion with counter-clockwise rotation and axial contraction across the natural log of applied pitch ($ln(p_{app})$) and the α or β (in degrees) that drives volume change. Plot is clipped at $\pm$ 15. Radius is set to 1 and plot is normalized for length.

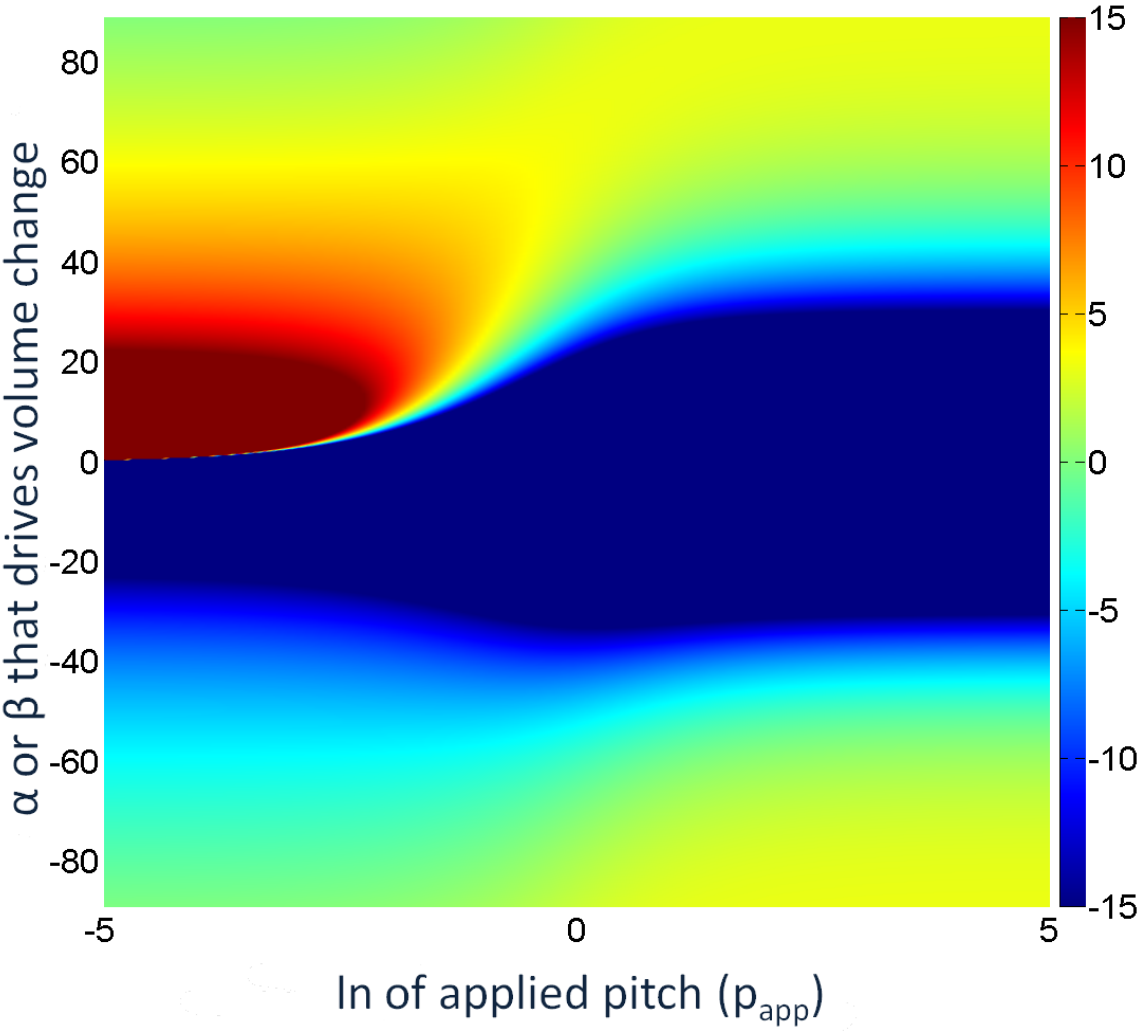

Figure 3.10: Volume change per unit screw motion with clockwise rotation and axial extension across the natural log of applied pitch ($ln(p_{app})$) and the α or β (in degrees) that drives volume change. Plot is clipped at $\pm$ 15. Radius is set to 1 and plot is normalized for length.

plots are important for determining the degree to which different directions of FREEs resist external motion, especially regions that have zero volume change, as those are freedoms.

3.4 Kinematic Design Space

The motion directions and volumetric effects of the kinematics are mapped to provide a designer with an intuitive set of tools to synthesize FREEs with desired properties. To provide an intuitive design tool and a computationally efficient method of synthesizing FREEs, the continuum design space of FREEs has been discretized into groups with similar properties.

3.4.1 FREE and Mobility Design Space

The kinematics are discretized into axial, rotational, and screw motions. The degrees of freedom and constraint are found by discretizing the volumetric transduction. Directions of motion that provide zero volume change are set to be freedoms, as motion in those directions does not change the volume. Directions of motion that provide positive volume change are seen as actuation directions, since increasing volume moves the FREE along these motions. Directions of motion that provide negative volume change are seen as constraint directions, as motion in these directions is resisted by fluid, especially if fluid incompressibility is assumed. An additional direction of motion not addressed is transverse bending, the bending of the FREE about an axis perpendicular to its axial direction. Along with this direction is transverse bending coupled with rotation. FREEs with longitudinal fibers ($\alpha = 0^\circ$ or $\beta = 0^\circ$) are constrained against transverse bending, since the volume decreases under deformation in bending. Rotational motion of these FREEs may increase the contained volume, which combined with a volume decrease from bending, results in no net volume change. In these cases, a transverse bend combined with a rotation is a degree of freedom.

Figure 3.11 visualizes the expansive design space of mobilities possible with FREEs, with 30 FREE regions that have different mobilities than their neighboring regions. For instance, region 6 extends and rotate, region 14 purely rotates with no extension or contraction, and region 25 produces no motion. Regions 17, 25, and 26 do not actuate in any direction, since the volume is maximized in the fabricated state.

Regions 16, 17, and 18 exhibit pure contraction, no motion, and pure extension, respectively. These types are called pneumatic air muscles (PAMs) or McKibben actuators. They do not rotate, exhibiting only contraction, no motion, and extension, respectively.

Figure 3.11 expands beyond McKibben actuators to show the entire design space for two fiber family FREEs, with each numbered region exhibiting a set of actuation and freedom directions.

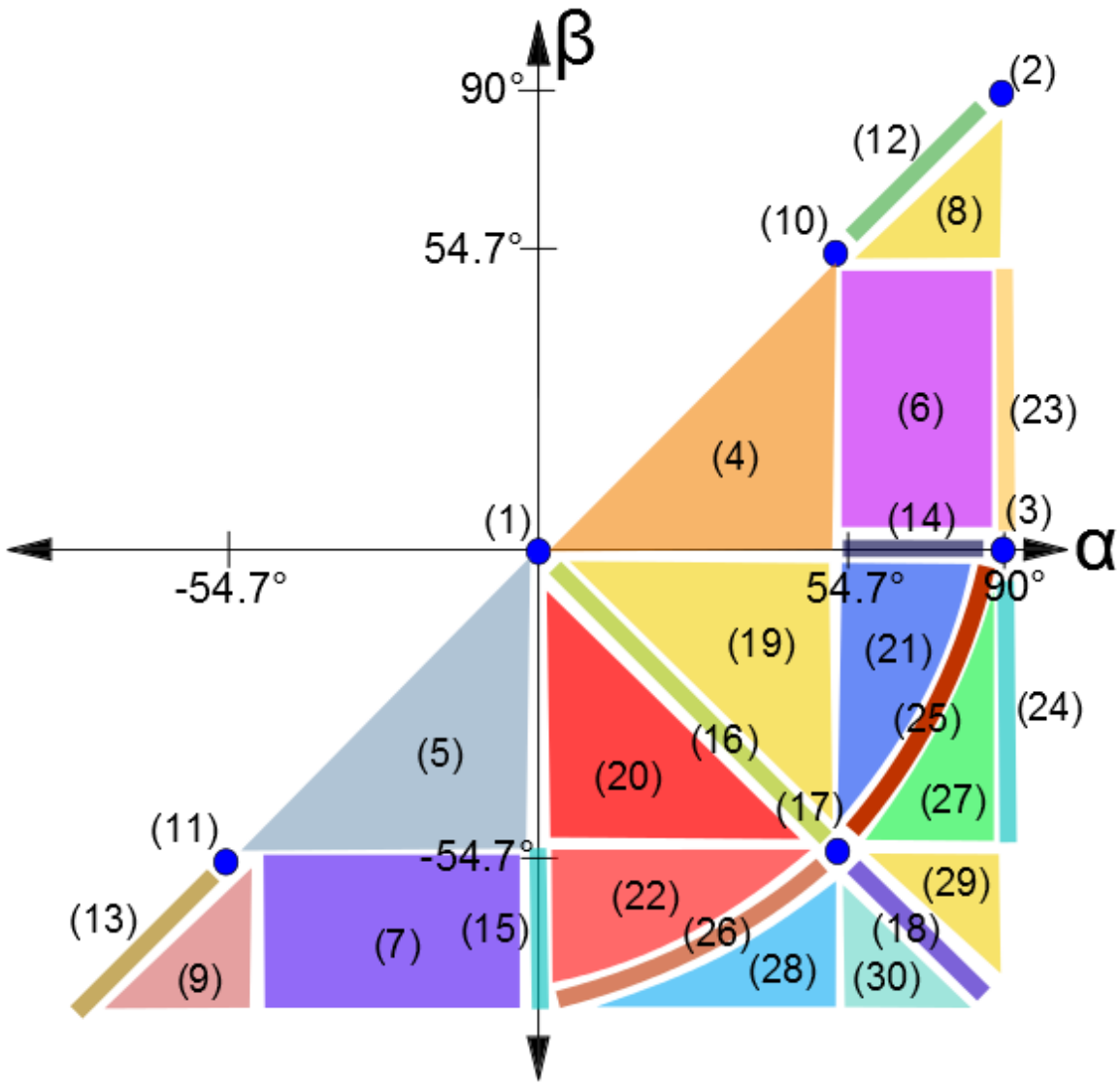

Figure 3.11: Regions of the two fiber family FREE design space. Each region spans a set actuation and freedom directions. Neighboring regions will differ in at least one actuation or freedom direction.

The space of possible mobility directions is shown in Figure 3.12. The regions that are not along an axis of this figure are screw motions, and have a mobility that is a specific combination of the motions along the axes. Region (F), for example, has a mobility in which the FREE simultaneously extends and rotates counter-clockwise in an interconnected manner. Rotation is defined as the direction of motion of the ends of the FREE when viewed from the center looking outward. The regions of this figure are also discretized as

discussed above.

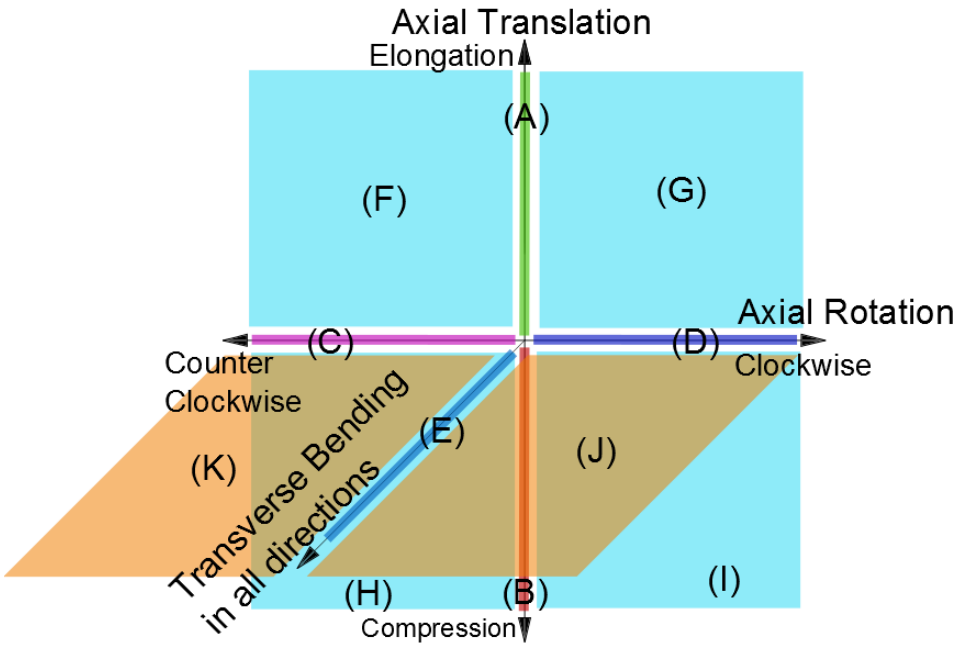

Figure 3.12: All mobility directions possible for two fiber family FREEs, shown on a 3-dimensional plot with each axis representing a mobility direction. Regions shown in cyan and orange are screw motions.

3.4.2 Mapping FREE to Mobility

A matrix mapping the FREE types to their respective mobility directions for both actuation and freedoms is shown in Table 3.2. 'A' indicates a mobility that the FREEs move under increasing volume, while 'F' indicates a mobility that the FREE is free to move without changing the volume or extending any fibers. 'AF' are directions for underconstrained FREEs that combine an actuation direction with a freedom direction, thus the FREEs increase in volume in these directions, but it is not in the direction of maximum volume increase. Unlabeled cells are constraints.

3.5 Summary

The expressions for the volumetric transduction provide an easy method to evaluate the volume displaced by an external motion. This volume is useful for understanding the response of the FREE to motions other than the actuation direction. The volumetric transduction equation is essential in equating the stiffness of the elastomer surface to stiffness at the

Table 3.2: The mobility mapping for all single FREEs. 'A' is an actuation direction that increases volume; 'F' is a freedom direction that keeps volume constant. 'AF' is a direction that combines actuation and freedom components. Unlabeled cells are constraints.

FREE Type	Mobility Direction (from Figure 3.12)										
(from Figure 3.11)	A	B	C	D	E	F	G	H	I	J	K
1	.	F	F	F	.	.	.	.	.	.	.
2	A	.	F	F	F	AF	AF	.	.	F	F
3	.	.	F	F	.	.	.	.	.	.	.
4	.	A	A	.	F	F	.	A	F	.	AF
5	.	A	.	A	F	.	F	F	A	AF	.
6	.	.	AF	.	F	A	.	F	.	.	AF
7	.	.	.	AF	F	.	A	.	F	AF	.
8	AF	.	AF	.	F	A	.	F	.	.	AF
9	AF	.	.	AF	F	.	A	.	F	AF	.
10	.	.	A	.	F	F	.	F	.	.	AF
11	.	.	.	A	F	.	F	.	F	AF	.
12	A	.	A	.	F	A	F	F	.	.	AF
13	A	.	.	A	F	F	A	.	F	AF	.
14	.	.	A	.	.	.	.	F	.	.	F
15	.	.	.	A	.	.	.	.	F	.	.
16	.	A	.	.	F	.	.	F	F	.	.
17	F	F	.	.	F	.	.	.	.	.	.
18	A	.	.	.	F	F	F	.	.	.	.
19	.	AF	.	.	F	.	.	A	F	.	.
20	.	AF	.	.	F	.	.	F	A	.	.
21	.	.	.	.	F	.	.	A	.	.	.
22	.	.	.	.	F	.	.	.	A	.	.
23	.	.	F	.	F	A	.	.	.	.	F
24	.	.	.	F	F	.	A	.	.	F	.
25	.	.	.	.	F	.	F	F	.	.	.
26	.	.	.	.	F	F	.	.	F	.	.
27	.	.	.	.	F	.	A	.	.	.	.
28	.	.	.	.	F	A	.	.	.	.	.
29	AF	.	.	.	F	F	A	.	.	.	.
30	AF	.	.	.	F	A	F	.	.	.	.

FREE output. The volumetric transduction plots provide a designer with an intuitive understanding of the range of possibilities for quick analysis and synthesis of FREEs. The plot showing the absolute value of the screw volumetric transduction allows a designer to quickly understand which directions are freedoms (mobility directions unconstrained by fluid or fiber constraints), as they show up as having no volume change. The mobility mapping further allows for rapid synthesis of desired mobility sets.

CHAPTER 4

Force and Moment Generation

The force and moment generation of fluid actuated fiber-reinforced elastomeric enclosures (FREEs) are controlled by the fluid pressure and the orientation of the fibers. This chapter describes modeling and experimental validation of force and moments generated by different FREE configurations. The first section of this chapter continues the modeling of Chapter 2, using virtual work of the fluid in the derivation of the force and moment models. The second section explains the experimental procedure used to test the force and moment generation. The third section describes the experimental results and compares them to the force models. The fourth section provides an example of the application of Chapters 2 through 4 to the design of an orthosis.

4.1 Force and Moment Models

Force and moment models were developed as an extension of the kinematics models. Relationships between volume and output displacements of the FREEs were determined. The addition of the virtual work of the fluid contained by the FREE can be applied to the volume expansion per unit motion to determine the magnitude of the forces and moments exerted.

4.1.1 Moment Model

The kinematics of the *unconstrained* FREE determines pressure normalized moment of the FREE about the axial direction. Equation 4.1 shows how the moment term can be derived starting from the virtual work equation for an expanding fluid, leading to the full expression of the moment in Eq. 4.2. The figure for this model is shown in Figure 4.1. Pitch, seen in Eq. 2.6, captures the kinematics of two fiber family FREEs, and is used in the moment derivation.

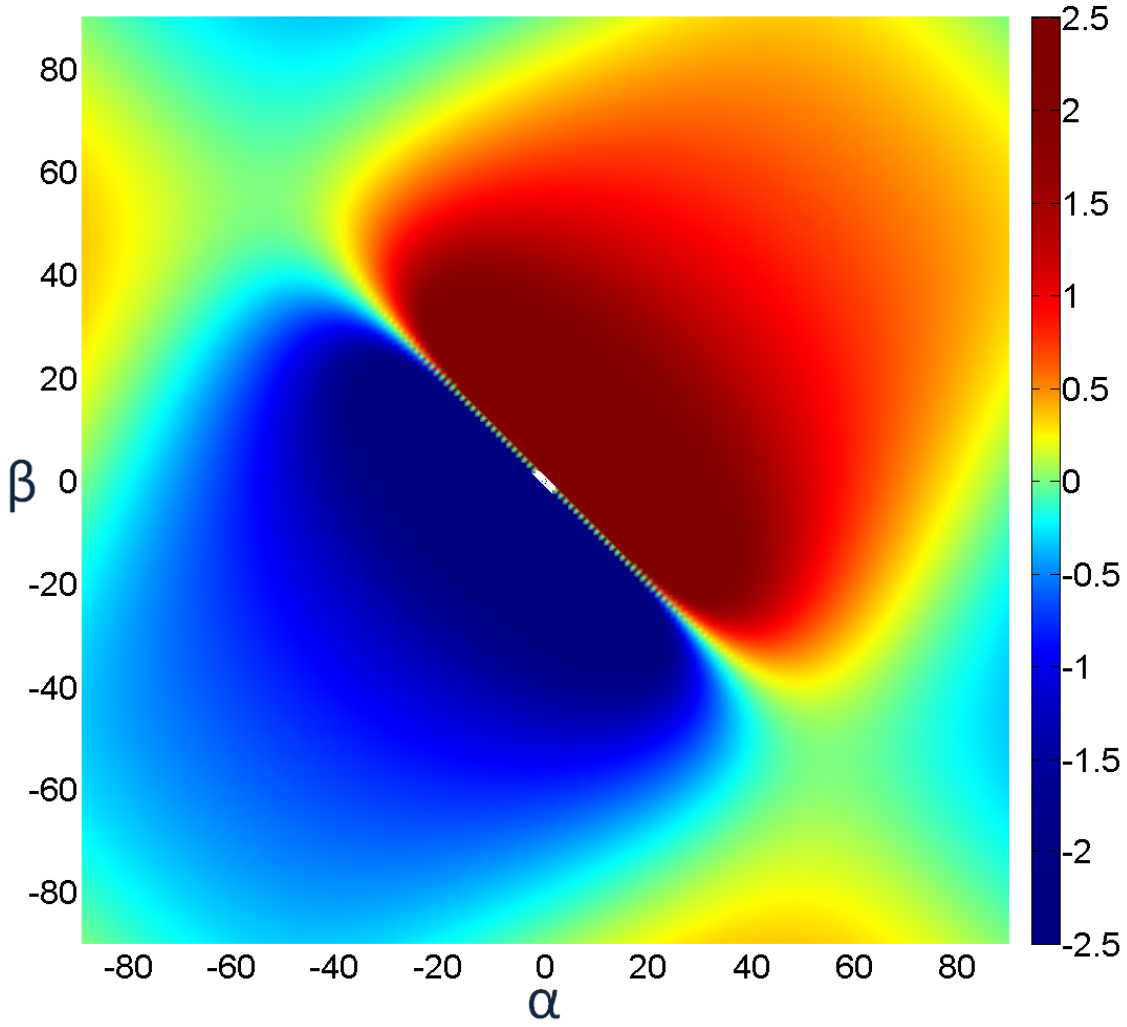

Figure 4.1: Analytical model of the moment per pressure ($\frac{N-mm}{kPa}$) across α and β (in degrees). Radius is set at 6mm. Plot is clipped at ± 2.5.

$$PdV = Fdl + Md\delta$$

(4.1)

$$PdV = \frac{M}{q} ld\lambda_1 + M\frac{ld\delta}{p} = Mld\lambda_1(\frac{p}{r^2} + \frac{1}{p})$$

$$where: q = \frac{r^2}{p}$$

$$M = \frac{P}{l}\frac{dV}{d\lambda_1}\frac{1}{p + \frac{r^2}{p}}$$

$$M = \frac{P}{l}(1 + 2\cot(\alpha)\cot(\beta))\pi r^2 l\frac{pr^2}{r^2 + p^2}$$

$$M = P\frac{\pi r^3((1 + 2\ \cot(\alpha)\cot(\beta))\sin(\alpha)\sin(\beta)\sin(\alpha - \beta)((\sin(\alpha))^2 - (\sin(\beta))^2)}{(\sin(\alpha))^2(\sin(\beta))^2(\sin(\alpha - \beta))^2 + (\sin(\alpha)^2 - (\sin(\beta))^2)^2}$$

(4.2)

4.1.2 Force Model

Similar to the moment model, the force model assumes that the volume expansion per unit motion, through virtual work, determines the magnitude of the force. For the force model, two different additional assumptions are considered, resulting in two differnt models for the force behavior. In Model #1, the assumption that the kinematics of the *unconstrained* FREE determines the pressure normalized force of the FREE is again used. Model #2 uses a different assumption, that the kinematics are determined using a *constrained rotation* that is fixed at zero (no rotation). The resulting change in volume is driven by pure linear motion, in this case the negative of compressive motion. Note that additional models can be created by modifying any of the underlying assumptions. The relative magnitudes of the force in Model #1 are governed by the pitch, while for Model #2, the compression leads to one family of fibers buckling, while the other one drives the motion.

This simple change in assumptions, from unconstrained kinematics to constrained rotation, substantially alters the resulting force model. Model #1 is derived in a similar manner to the moment model (Eqs 4.1 and 4.2), but for force instead. The derivation is seen in Eq. 4.3. The figure for Model #1 is shown in Figure 4.2. The derivation for Model #2 is shown in Eq. 4.4. $\frac{dV}{d\lambda_1}$ only acts in the axial direction, since the rotation, and consequently volume change from rotation, is fixed at zero. The figure for Model #2 is shown in Figure 4.3.

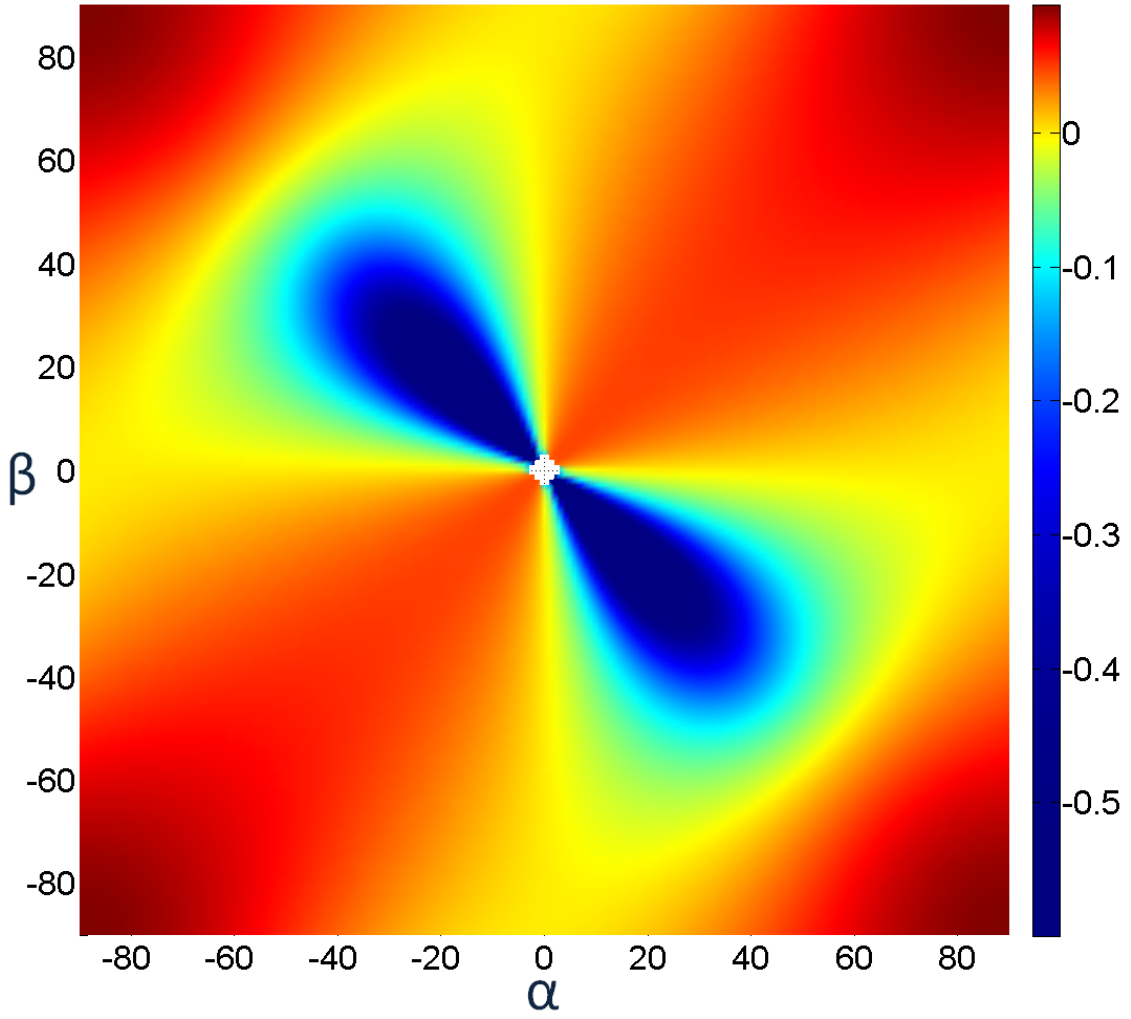

Figure 4.2: Analytical Model #1 of the force per pressure ($\frac{N}{kPa}$) across α and β (in degrees). Radius is set at 6mm. Model #1 assumes unconstrained kinematics drives the volume change magnitude and resulting force magnitude and direction. Plot is clipped below at -0.6.

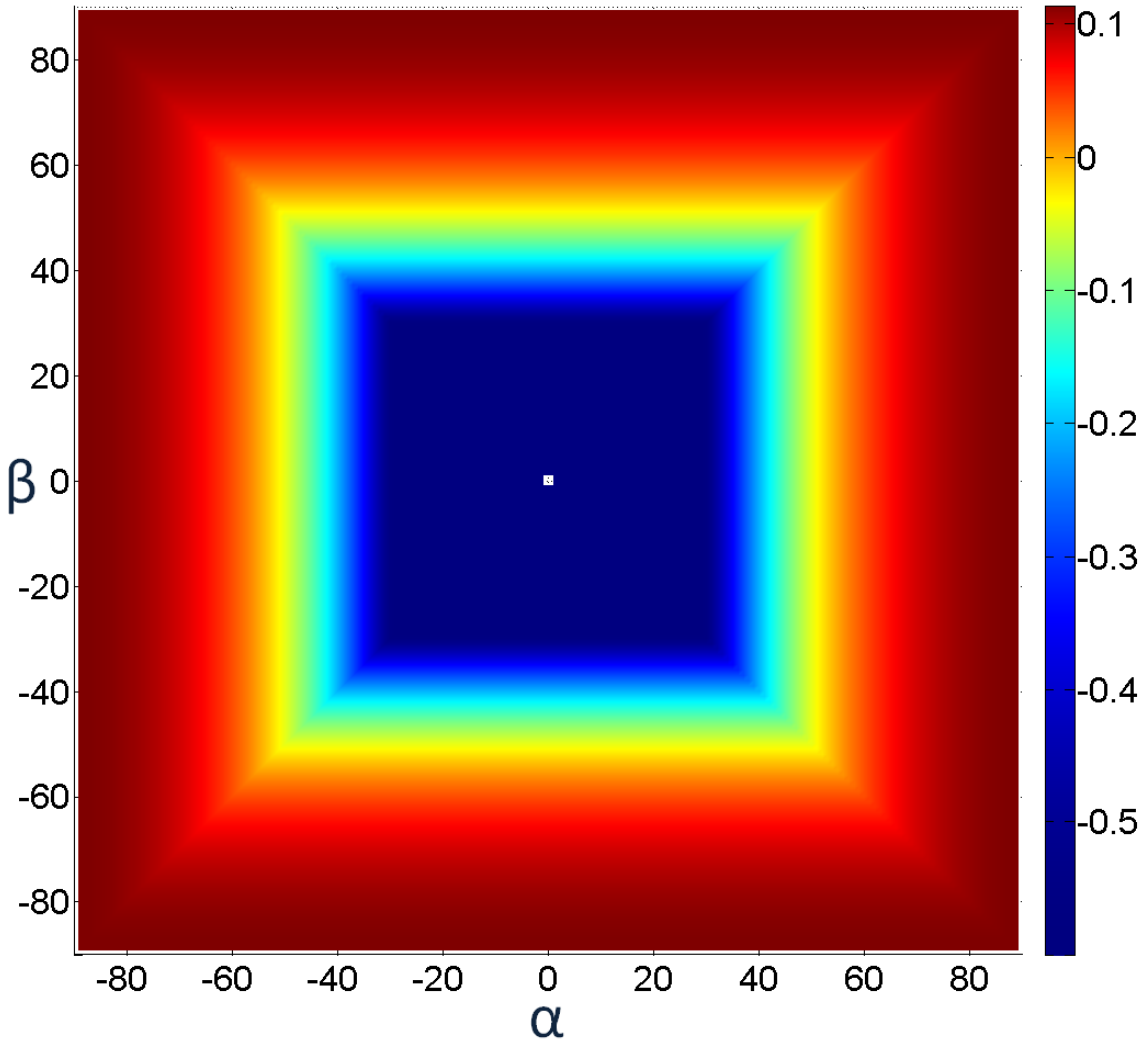

Figure 4.3: Analytical Model #2 of the force per pressure ($\frac{N}{kPa}$) across α and β (in degrees). Radius is set at 6mm. Model #2 assumes kinematics of fibers with a fixed rotation drives the volume change magnitude and resulting force magnitude and direction. Plot is clipped below at -0.6.

$$PdV = Fdl + Md\delta = Fld\lambda_1 + M\frac{ld\delta}{p}$$
$$PdV = Fld\lambda_1 + Fq\frac{ld\delta}{p} = Fld\lambda_1(1 + \frac{r^2}{p^2})$$
$$where: q = \frac{r^2}{p} F = \frac{P}{l}\frac{dV}{d\lambda_1}\frac{1}{1+\frac{r^2}{p^2}}$$
$$F = \frac{P}{l}(1 + 2\cot(\alpha)\cot(\beta))\pi r^2 l\frac{p^2}{r^2+p^2}$$
$$F = P\frac{\pi r^2((1 + 2\ \cot(\alpha)\cot(\beta))(\sin(\alpha))^2(\sin(\beta))^2(\sin(\alpha-\beta))^2)}{(\sin(\alpha))^2(\sin(\beta))^2(\sin(\alpha-\beta))^2 + ((\sin(\alpha))^2 - (\sin(\beta))^2)^2} \tag{4.3}$$

$$\lambda_1^2(\cos(\chi))^2 + \lambda_2^2(\sin(\chi))^2(\frac{\theta^*}{\theta})^2 = 1$$
$$\delta = 0 \implies \frac{\theta^*}{\theta} = 1$$
$$\lambda_2^2 = (\csc(\chi))^2 - (\cot(\chi))^2\lambda_1^2$$
$$V^* = ((\csc(\chi))^2\lambda_1 - (\cot(\chi))^2\lambda_1^3)\pi r^2 l$$
$$\lim_{\lambda_1 \to 1}\frac{dV}{d\lambda_1} = \pi r^2 l(1 - 2(\cot(\chi))^2)$$
$$PdV = Fdl = Fld\lambda_1 \implies F = P\frac{dV}{ld\lambda_1}$$
$$F = P\pi r^2(1 - 2(\cot(\chi))^2) \tag{4.4}$$

where: χ is α or β that is further from axial

4.2 Experimental Method

The physical experimental setup is detailed in Section 4.2.1. Section 4.2.2 explains the experimental procedure, including the values of α and β that were experimentally tested.

4.2.1 Experimental Setup

The test setup, shown in Figure 4.4, was used to measure the force and moment. The force was measured by a steel S beam resistive load cell (Loadstar RAS1-025S Resistive Load Cell, 25 Lbs capacity, $\pm 0.02\%$ FSO accuracy, universal mode digital calibration). The moment was measured with a reaction torque sensor (Loadstar RST1-006NM Resistive

Torque Sensor with 6 Nm max capacity, $\pm 0.2\%$ FSO accuracy, digital torsion calibration). Force and moment measurements were sent to the computer through two Loadstar DI-1000 Digital Load Cell Interface boxes. Off axis effect on each load cell (e.g. load on the torsion sensor and torsion on the load cell) were tested prior to experimentation and found to be negligible.

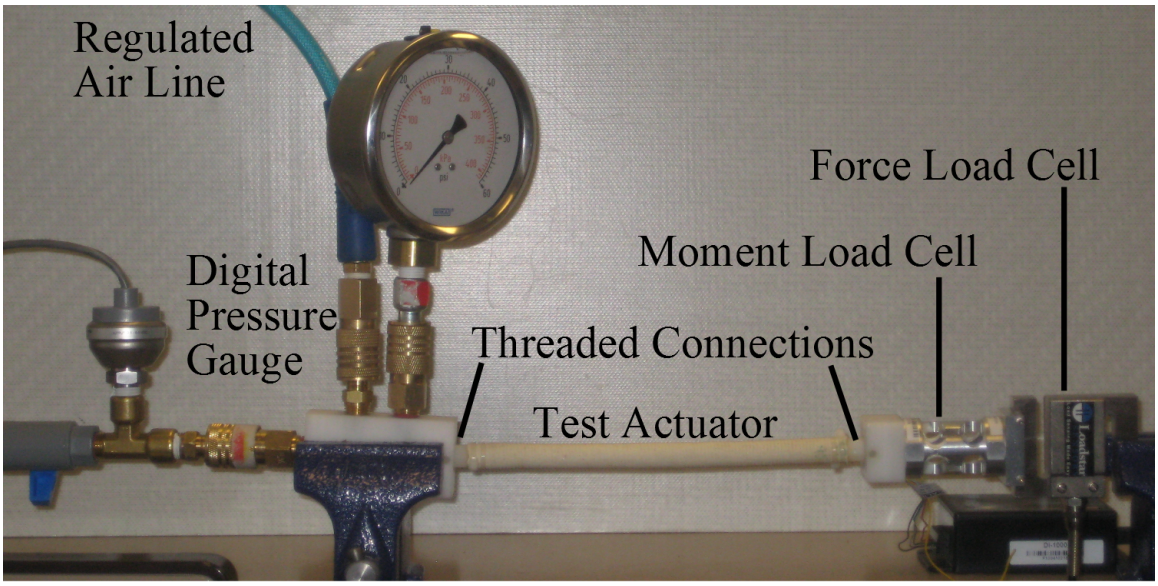

Figure 4.4: The experimental force and moment setup with key components labeled.

Custom mounting brackets were fabricated to hold the load cells together in series. Additional custom connections were fabricated to provide $\frac{1}{8}$ NPT tapped holes connecting the actuator being tested to the load cells on one end, and to the air inlet and pressure measurement on the other. The pressure was controlled manually from a regulated air compressor (Rigid 5-in-1 dual tank). The resulting pressure was measured using a digital pressure gauge (Cole Parmer 0 to 50 psig ± 0.25 PSI accuracy gauge transmitter, 0.5 to 5.5V output, P/N 68075-46). Measurements were sent to a computer using a Phidget 2/2/2 interface kit. An additional visual pressure gauge was attached to help with experimentation. The load cell setup and the pressure setup were fixed to a rigid surface using mounted clamps. The actuators consist of a hollow rubber core, cotton fibers, and a latex outer coating with $\frac{1}{8}$ NPT threaded connections on either side.

4.2.2 Experimental Procedure

The actuator for each test was installed by setting the distance between the threaded connections at the actuator's deflated length. The actuator was screwed into the threaded connection with no relative rotation between the ends. The ends were tightened enough to

ensure no freedom to rotate, thus acting as fixed constraints. The pressure was manually increased, then held at numerous pressures up to the maximum safe pressure each actuator could withstand without failing or buckling (maximum pressure ranged from 100 to 275 kPa for the different actuators). The pressure was fixed until variables remained near constant over time, and the values at that point were recorded. Three sweeps were made from zero to maximum pressure, with measurements taken in each sweep.

This experiment investigated the effect of α and β on the force and moment generation. Only a quarter of this design space requires experimental testing in order to understand all α and β combinations. A checkerboard pattern of 45 α and β combinations were selected for experimental testing, with the chosen values shown in Figure 4.5. Red dots indicate α and β values with six actuators tested, while hollow black dots had one actuator tested. Points very near the $\alpha = \beta$ line were not considered, as $\alpha = \beta$ points are degenerate cases that are underconstrained, which allows the actuators to inflate in an uncontrolled manner until failure. The radius parameter of the FREE actuators is fixed at 6 mm.

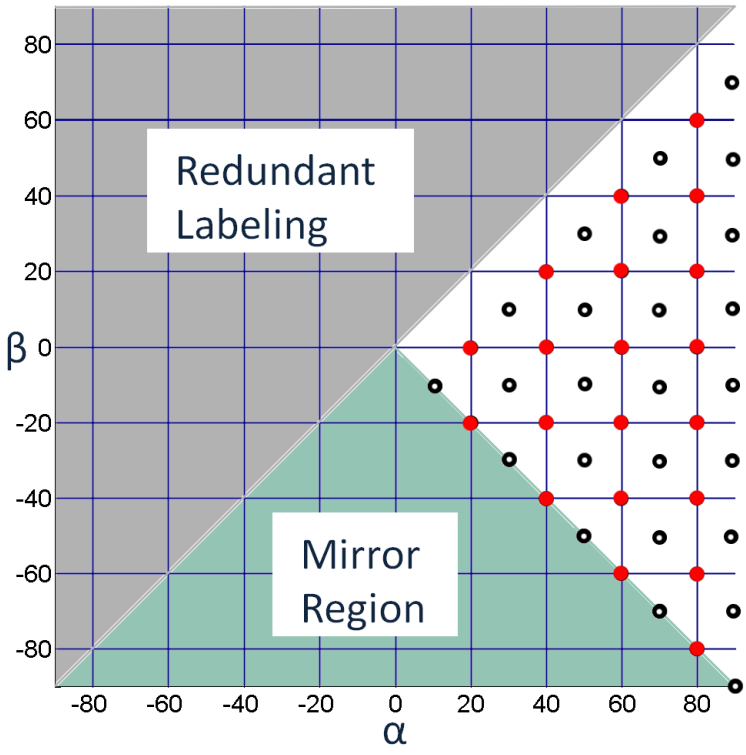

Figure 4.5: α and β points tested are shown as red dots for α and β combinations with six actuators tested, while hollow black dots had one actuator tested. α and β combinations that are redundantly labeled are in the top left region, and α and β combinations that are mirror images of tested ones are in the bottom region.

4.3 Results

The direct data from the experimental tests was processed to understand the forces and moments across the entire design space. This data processing is explored in Section 4.3.1. The resulting experimental force measurements are shown in Section 4.3.2, while the moment measurements are shown in Section 4.3.3.

4.3.1 Data Processing

The force and moment measurements were highly linear with pressure for nearly all tests, most with an R^2 (coefficient of determination) over 0.990. The resulting slopes ($\frac{force}{pressure}$ and $\frac{moment}{pressure}$) were calculated for all tests, and these values were used for comparison across α and β values. The full force plot was obtained by mirroring the values collected in the quarter of the design space across the $\alpha = \beta$ and $\alpha = -\beta$ lines. The full moment plot was obtained by mirroring the values across the $\alpha = \beta$ line, then taking the negative of the values mirrored across the $\alpha = -\beta$ line.

A high resolution image was created from the data points by first interpolating the checkerboard pattern (seen in Figure 4.5) to a full grid of points spaced every 10° using a cubic interpolation. This grid of points was then cubically interpolation to obtain a final high resolution grid (every 1.25°) of force or moment per pressure values.

4.3.2 Experimental Force Results

The plot of the force normalized by pressure ($\frac{force}{pressure}$) across α and β helix angles (in degrees) is shown in Figure 4.6. Positive force indicates the actuator is exerting a force in the axial elongation direction, while negative is a contraction force. The normalized force is in Newtons per kilopascal ($\frac{N}{kPa}$).

The force appears to take a square shape, with the forces trending towards contraction as α and β both head towards zero (fibers aligned along the axial direction). The square shape indicates that the fiber angle furthest from zero (closer to 90° or -90°) is driving the force term. An example of this effect is seen in Figure 4.6 where $\alpha = 10^\circ$, $\beta = -80^\circ$ has a similar force to $\alpha = 50^\circ$, $\beta = -80^\circ$, since the angle furthest from zero ($\beta = -80^\circ$) is the same for both points.

The force crosses the zero line at approximately 54 degrees, which can be seen in orange in Figure 4.6. This aligns closely with existing knowledge about McKibben actuators, which at $\alpha = 54.74^\circ$, $\beta = -54.74^\circ$ produce no force when pressurized (the actuator will stiffen, but it will not exert force from its uninflated length). Beyond the $\alpha = 54.74^\circ$,

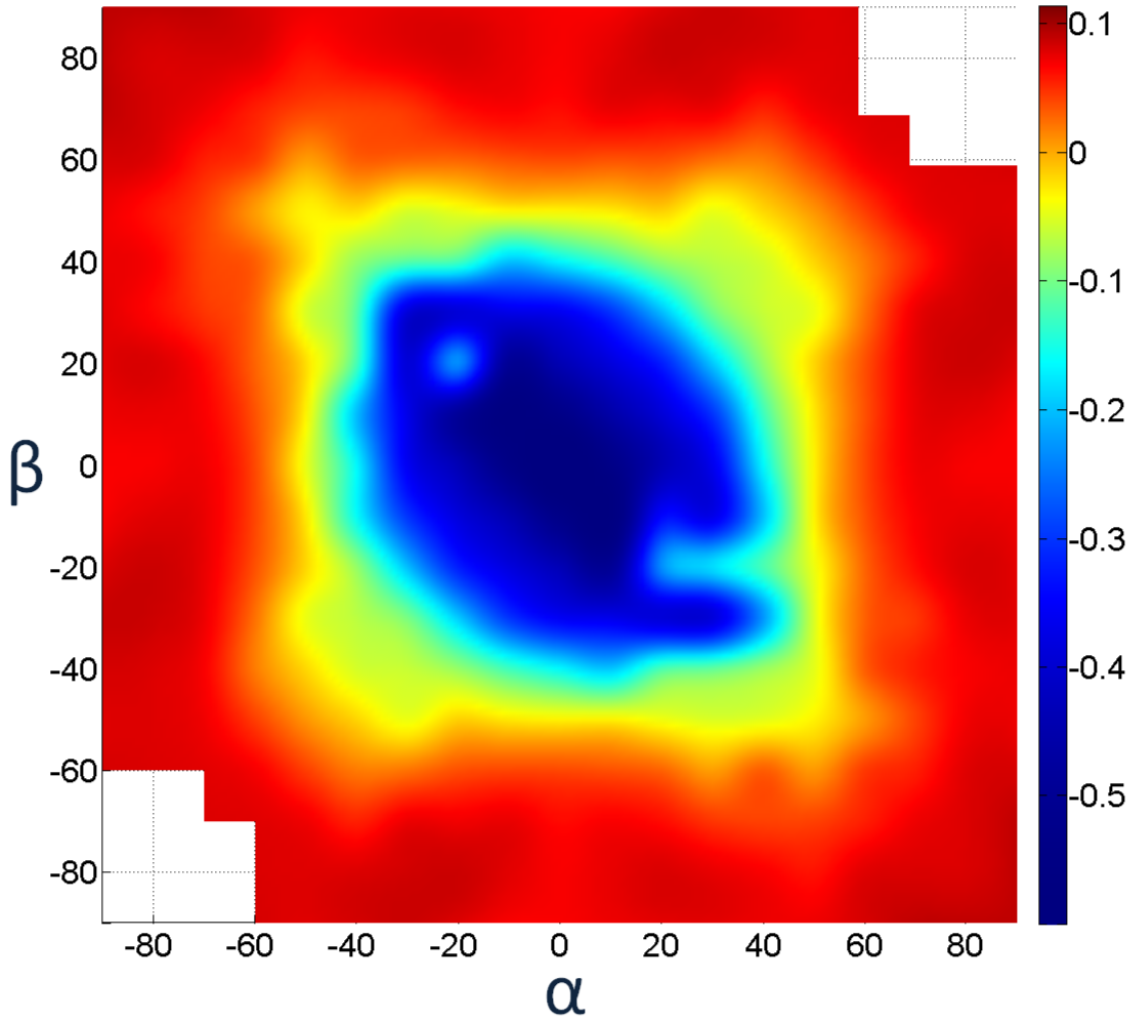

Figure 4.6: Experimental force per pressure ($\frac{N}{kPa}$) across α and β (in degrees). Mirroring and cubic interpolation are used to obtain the entire design space from measured points seen in Figure 4.5. Radius is set at 6mm.

$\beta = -54.74°$ point, the entire McKibben actuator line of $\alpha = -\beta$ shows force values that align very closely with those expected from prior literature [78].

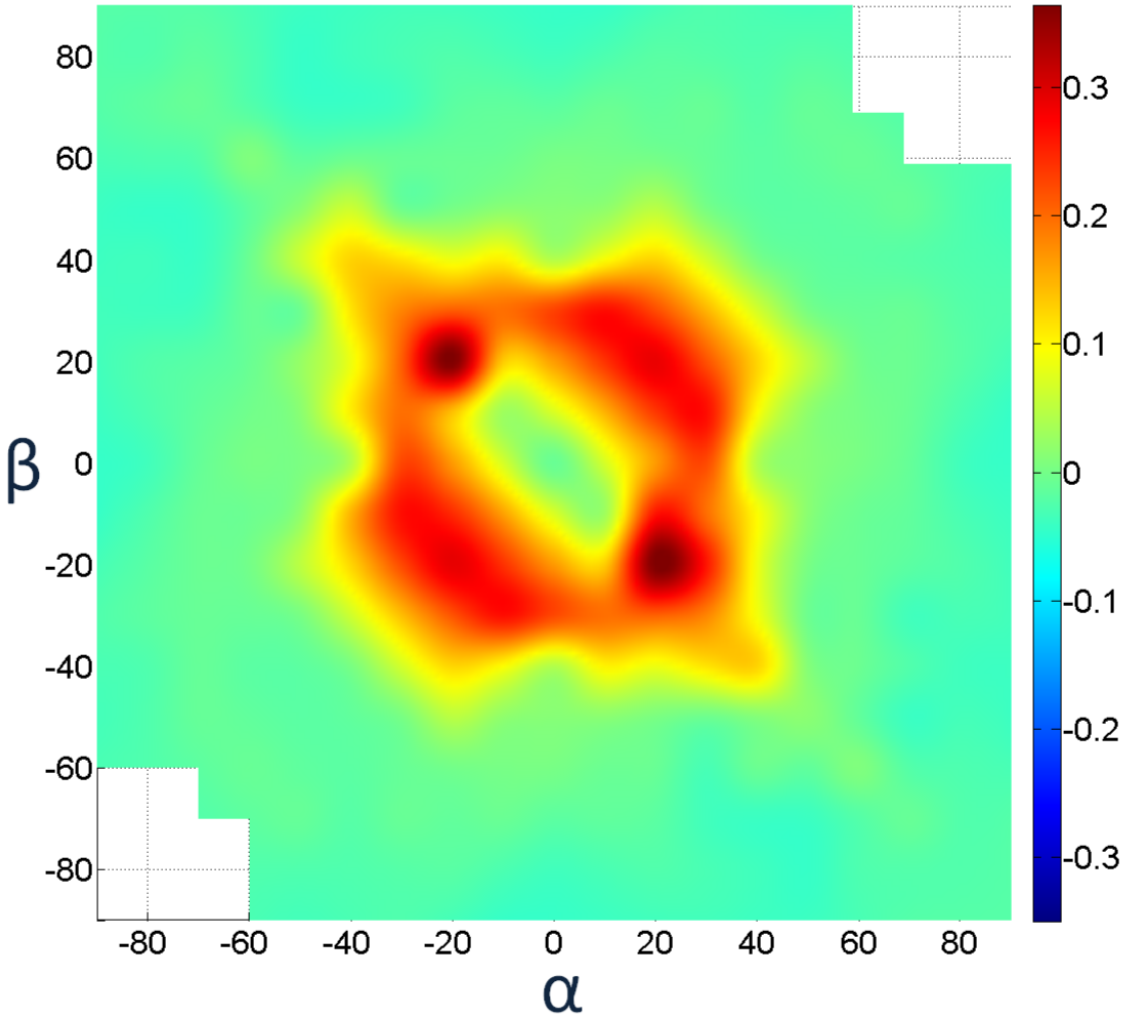

Figure 4.7: Residual of the experimental and analytical Model #2 of the force per pressure ($\frac{N}{kPa}$) across α and β (in degrees). Radius is set at 6mm.

Force Model #2 appears to closely predict the experimental values, while Model #1 substantially deviates. This shows that the assumption underlying Model #2, of using the fixed rotation and the negative volume change of compression, accurately reflects the behavior of a constrained, actuated FREE in force generation. This result is non-intuitive, as the assumptions that underlie the force model are different from those that represent the experimental moment values. To verify the quality of the prediction for Model #2, the residual is computed for all points, and is seen in Figure 4.7. The residual is largest in the region near the $\alpha = \beta$ line, which as discussed in Section 4.2.2, were not tested for. The remaining regions have a low residual, with exceptions from a few data points, implying

this analytical model is a very good representation of the experimental data.

4.3.3 Experimental Moment Results

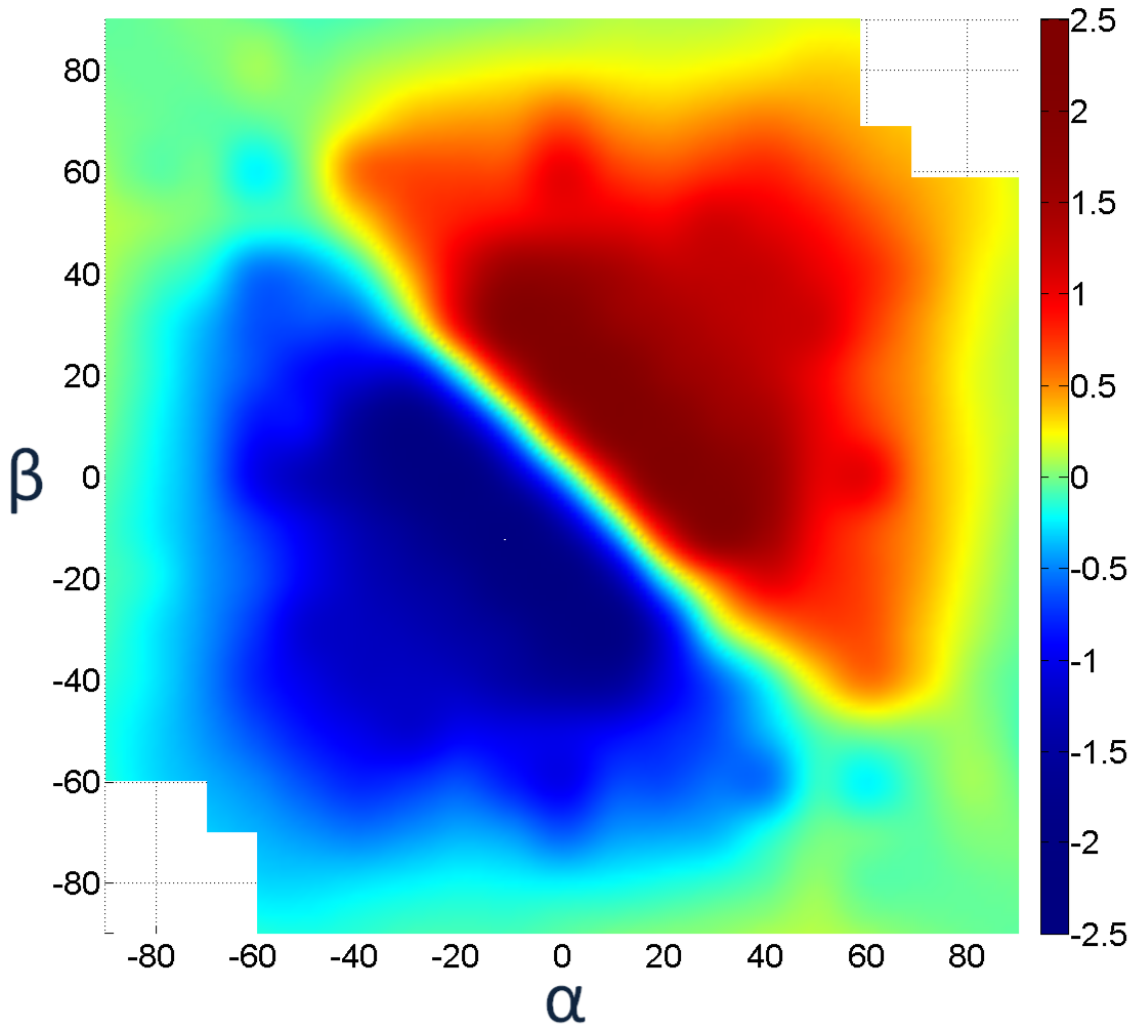

Figure 4.8: Experimental moment per pressure ($\frac{N-mm}{kPa}$) across α and β (in degrees). Mirroring and cubic interpolation are used to obtain the entire design space from measured points seen in Figure 4.5. Radius is set at 6mm.

The plot of the moment normalized by pressure ($\frac{moment}{pressure}$) across α and β helix angles (α and β in degrees) is shown in Figure 4.8. Positive moment indicates the actuator is exerting a moment in the counter-clockwise direction when viewed from the actuator facing outward, while negative is a clockwise moment, again from the middle of the actuator looking towards the ends. The normalized moment is in Newton-millimeters per kilopascal ($\frac{N-mm}{kPa}$).

One region in which the moment reaches zero is down the $\alpha = -\beta$ line, seen in green. This aligns closely with existing knowledge that McKibben actuators ($\alpha = -\beta$) produce no moment when pressurized (the actuator will stiffen, but it will not exert moment from its deflated length and rotation).

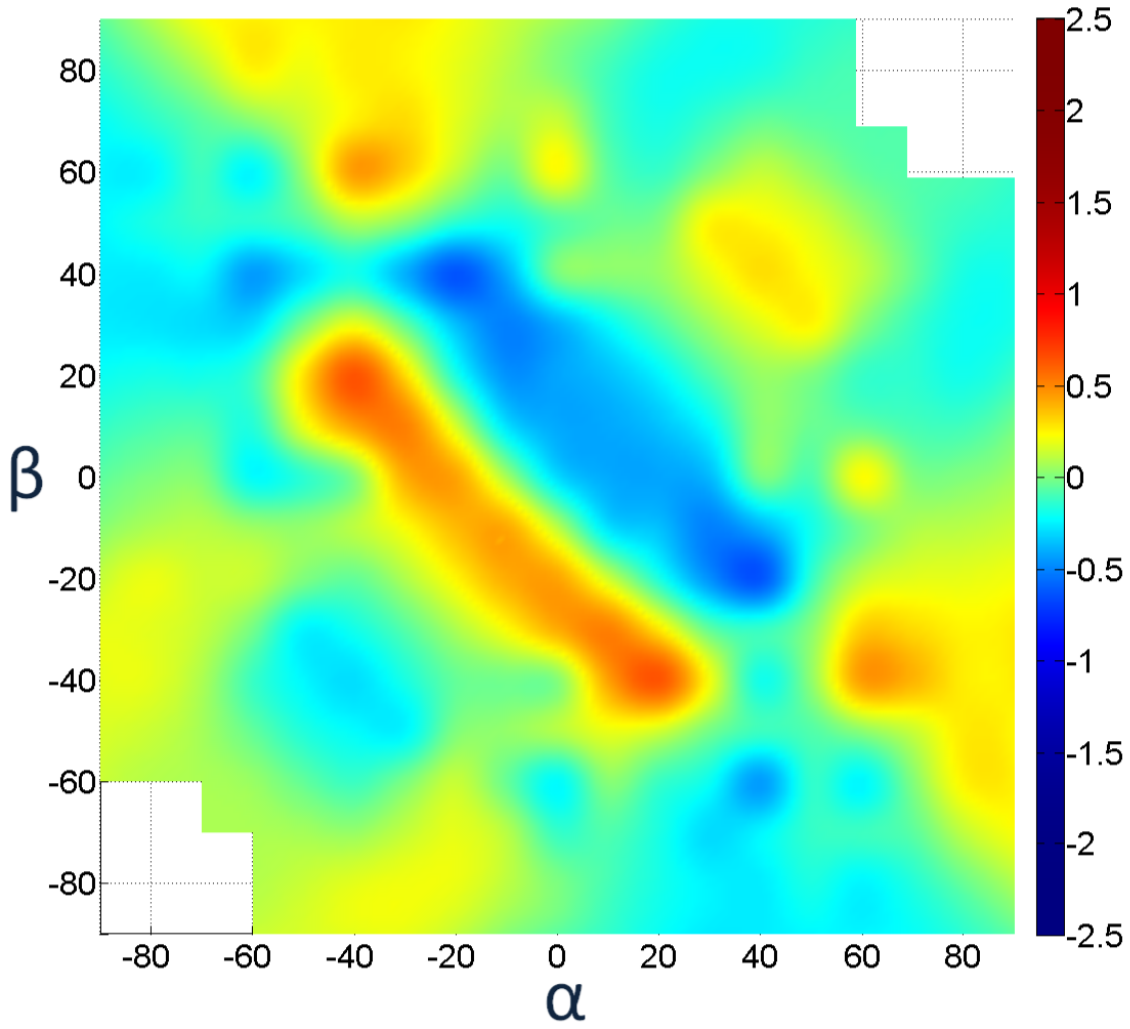

Figure 4.9: Residual of the experimental and analytical model of the moment per pressure ($\frac{N-mm}{kPa}$) across α and β (in degrees). Radius set at 6mm.

The moment model appears to accurately predict the experimental values. To verify the quality of the prediction, the residuals were computed for all points, and is seen in Figure 4.9. The residual is largest in the region near the $\alpha = \beta$ line, which as discussed in Section 4.2.2, were not tested, as these actuators have a tendency to expand uncontrollably. The remaining regions have a low residual, with exceptions from a few data points, implying this analytical model is a very good representation of the experimental data. This further shows that the model assumption of using the unconstrained kinematics and the volume change

per motion with virtual work accurately reflects the behavior of a constrained, actuated FREE in moment generation.

4.4 Orthosis for Limb Torsion

The application of Chapters 2 through 4 is used to design an orthosis device for limb torsion. The clinical need is addressed in Section 4.4.1, the design of the device is examined in Section 4.4.2, and the final device is shown in Section 4.4.3.

4.4.1 Clinical Need

Incorrectly positioned limbs can have a detrimental effect on quality of life. These conditions affect either the lower limbs (leg torsion) or upper limbs (arm torsion). Some conditions cause the incorrect rotation of limbs, especially in children, while other conditions prevent the actuation of the muscles that generate the torsion. For arm torsion, injury to C6 vertebrae and above causes paralysis in arm rotation.

This device will focus on arm torsion contractures. This condition is caused by muscles, tendons, ligaments, joint areas, or skin forcefully rotating the arm. The function and range of motion of the arm are consequently impaired. There is currently no good orthosis for arm torsion issues, and existing attempts have been large, heavy, and dangerous. The clinical requirement for an arm torsion orthosis is summarized as:

1. Generation of a rotational moment at the wrist in a controlled manner.
2. Does not adversely affect other degrees of freedom.
3. Lightweight.
4. Low profile, to the extent of fitting under clothing.
5. Does not risk injury to patient or surrounding environment.
6. Low cost.

4.4.2 Orthosis Design

FREEs provide a good solution to the clinical need, as they are lightweight, low cost, and safe for human interaction. With a high moment generation per pressure, the device can be made small enough to maintain a low profile while generating sufficient rotational

moments. Correct design of fiber reinforcement is necessary to create this high moment generation while ensuring the remaining degrees of freedom of the arm are not restricted.

To generate a pure rotation without creating adverse extension or contraction, an actuator that is in regions 14 or 15 of Figure 3.11 is selected. The design focuses on the counter-clockwise rotation of the arm, which is found in region 14; the opposite rotation is simply the mirror fiber reinforcement of this design. The next requirement is a high moment creation, without any contraction or extension force. Region 14 has a family of fibers at an angle of $0°$, thus the design focuses on the other family of fibers. Figure 4.1 shows that the family of fibers should be as close to $0°$ as possible to generate maximum moment, while Figure 4.3 shows the family of fibers should be placed at $54.74°$ from axial. This configuration creates a pure torsion force.

The contact point with the body is placed on the wrist at one end, and on the upper arm on the other. This connection to the upper arm requires the device to traverse the elbow region, and the device must not restrict or actuate the elbow bending motion. To do this the fiber reinforcement must generate no rotation or translation forces or motion at the joint, while allowing for easy bending of the elbow. Figures 3.11, 4.1, and 4.3 all show that setting the fiber angles to be $\alpha = 54.74°$, $\beta = -54.74°$ generates these desired properties. The continuation of one family of fibers at $54.74°$ ensures ease of fabrication. The resulting fiber reinforcement for the device is shown in Figure 4.10.

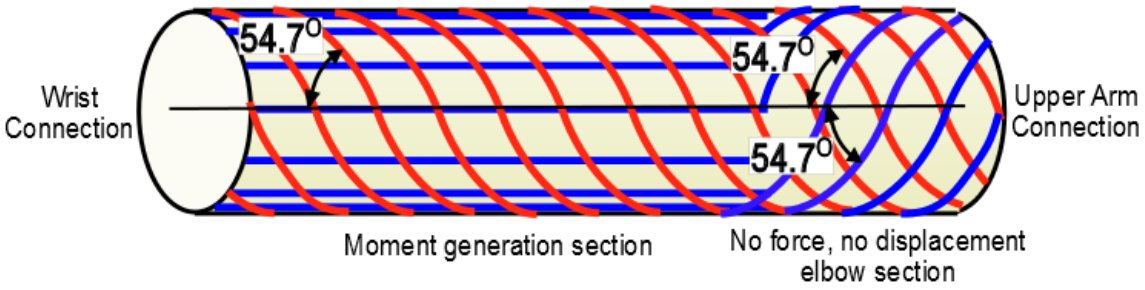

Figure 4.10: Fiber angles of a FREE for use as an arm torsion orthosis. The section on the left generates torsion, while the section on the right allows for rotation at the elbow without displacement or force generation.

4.4.3 Orthosis Device

Figure 4.11 shows the device attached to the arm. The device was able to successfully generate large rotational forces at pressures below 250 kPa. There was sufficient flexibility in the elbow section with no detectible moment, extension, or contraction forces. Further refinement of this application to a full orthosis system including air pumps and feedback

control is future work. Further refinement of attachment points to the body, component integration, and FREE fabrication, as well as human testing are all needed to realize this application in a clinical environment.

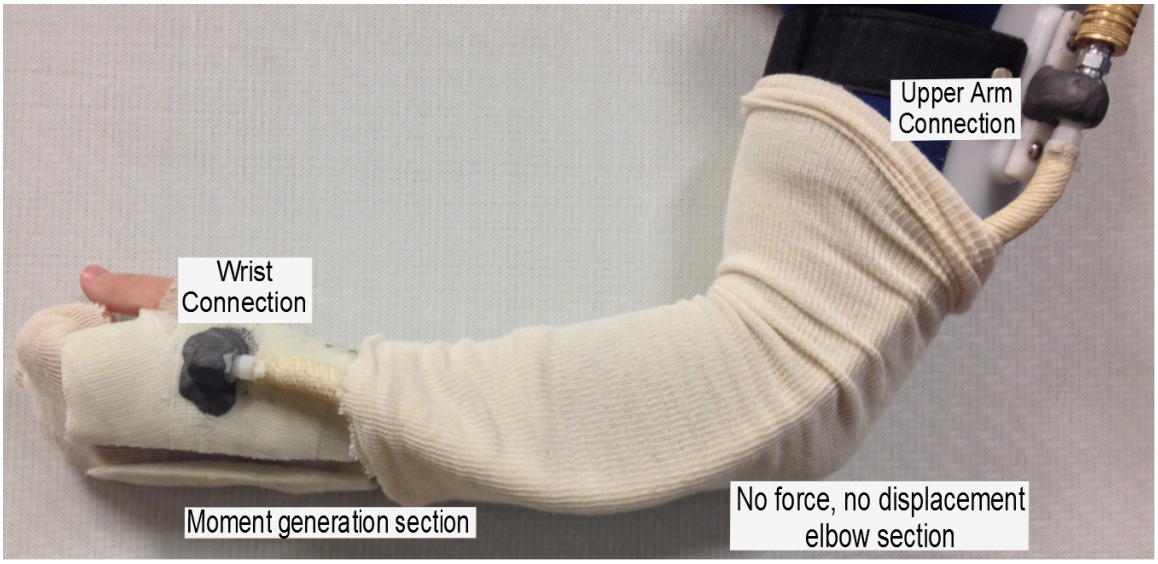

Figure 4.11: Arm torsion orthosis using FREEs for actuation. The section along the forearm generates torsion, while the section near the elbow allows for rotation at the elbow without displacement or force generation.

4.5 Summary

This chapter used kinematics in conjunction with virtual work to determine analytical models of the force and moment. Experimental force and moment generation for FREEs with two families of fibers were tested across the entire design space using a blocking-load based test. The kinematics of an unconstrained actuator best predicts the moment generation, while the kinematics of a rotation constrained, compressive load best predicts the force generation. The results also compared favorably to existing research on McKibben actuators. This chapter provided:

1. Experimental determination of the force and moment for FREEs with two families of fibers.

2. Analytical models of the force and moment of FREEs.

3. Graphical representation of the force and moment design spaces, allowing for fast and intuitive synthesis of FREEs with desired force and/or moment.

4. Application of the force analysis methods to the development of a soft orthosis.

The experimental and analytical model plots allow a designer to understand the sensitivity of the design to changes in fiber angle. By addressing the full range of FREEs, beyond just McKibben actuators, a wide range of actuation types are possible, including pure moment and every type of wrench (combination of moment and force).

CHAPTER 5

Parallel Combinations

Combining FREEs in parallel allows for complex motions, multiple degrees of actuation, and freedoms and constraints not possible with single FREEs. To model and generate synthesis methods for parallel FREEs, the design space and mobility mapping seen in Figure 3.11 and Table 3.2 are used. The first section of this chapter discusses the constraint based method for analyzing and synthesizing FREEs in parallel. The second section describes the graphic user interface synthesis tool, and the final section provides an example of a walking robot created with a continuum spine made of parallel FREEs.

5.1 Parallel Synthesis

The design spaces of kinematics, volumetric transductions, and forces are all continuum for FREEs. To provide a computationally fast and conceptually simple method of synthesizing FREEs in parallel, these continuum design spaces have been discretized. This discretization allows for the implementation of a constraint based design method for FREEs in parallel. The discretized system was shown in Section 3.4. A designer will specify the necessary degrees of actuation, freedom, and constraint for the parallel FREE system. While a discretized system will not provide as accurate of motion and constraint predictions, it allows for the rapid synthesis across the entire design space.

In order to determine the mobility of parallel FREEs, the mobility of all constituent elements is combined. This is accomplished by combining the four mobility types that are possible for cylindrical FREEs, with the parallel mobility spanning permutations of these types. These types are axial translation, bending, rotation, and screw.

5.1.1 Constraint Synthesis

The constraints are determined for triangular triplets of actuators, seen in Figure 5.1. The parallel system can axial translate, rotate, screw, bend, and/or bend-screw (combination of

bending and rotating). When treating the pressurization of the actuators as binary (pressurize or unpressurized), there are 44 coordinate dependent mobility directions for triangular triplets of actuators.

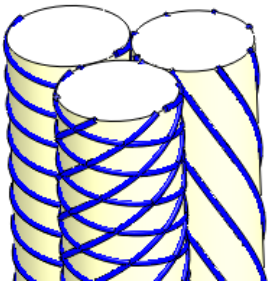

Figure 5.1: Trianglular triplet of parallel FREEs (or actuators).

Four of the motions follow a rather simple set of rules:

1. Axial translation is a parallel mobility if and only if all actuators have mobility in axial translation in the parallel mobility direction.

2. Rotation is a parallel mobility if and only if all actuators have mobility in rotation in the parallel mobility direction.

For mobility directions that are screw motions, screw coupling needs to be considered. For parallel screw mobilities that combine rotation with axial translation, three conditions need to be met:

1. Each actuator must either axially translate in the parallel mobility direction or have a coupled translation and rotation identical to the parallel mobility direction.

2. Each actuator must either rotate in the parallel mobility direction or have a coupled translation and rotation identical to the parallel mobility direction.

3. At least one of the actuators must have a coupled translation and rotation identical to the parallel mobility direction.

For bending motions, three different planes may serve as the neutral axis. Figure 5.2 shows the two fundamental bending directions for triangular triplets as well as their respective neutral axis planes. For a parallel mobility in bending, the following rules must be met:

1. All actuators must have mobility in bending.

2. For bending direction 1, one or more of the following must be true:
   (i) Actuator 2 is axially compressing and Actuator 3 is axially extending.
   (ii) Actuator 1 and Actuator 3 are axially extending.
   (iii) Actuator 1 and Actuator 2 are axially compressing.

3. For bending direction 2, one or more of the following must be true:
   (i) Actuator 1 and Actuator 2 are axially compressing.
   (ii) Actuator 3 is axially extending.

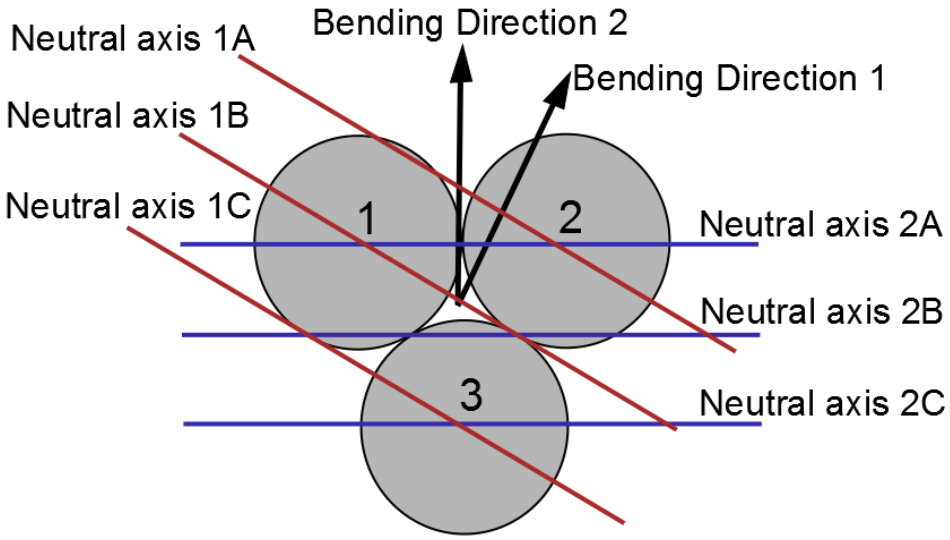

Figure 5.2: Notation for actuator number, actuation directions, and neutral planes in bending for triangular triplet actuators. Top view shown.

There are additional mobility sets in the direction opposite to bending directions 1 and 2 by reversing axial extensions and axial compressions in each of their respective set of rules. For 120° rotation of the coordinates defining the bending direction and associated actuator numbering, the same rules will hold true. Rules for screw motions that coordinate bending and rotation are the following:

1. The actuators must have axial translations and bending according to the rules used to determine parallel mobility bending in the correct direction. These mobilities may be coupled with rotations in the parallel mobility direction.

2. Each actuator must either rotate, have a coupled bend and rotation, or a coupled axial translation and rotation, with the rotation components all in the parallel mobility direction and the translations forming the correct bending direction.

3. At least one of the actuators must have either a coupled translation and rotation or a coupled bending and rotation, with the rotation components all in the parallel mobility direction and the axial translations forming the correct bending direction.

5.1.2 Actuation and Freedom

With multiple actuators placed in parallel, constituent actuators undergoing volumetric expansion will be referred to here as 'active' actuators. The parallel rules determined the mobility directions of the system, while a mechanical designer is interested in the freedom and actuation directions. In order to determine freedom and actuation directions from the mobility directions, the properties of the active and inactive actuators are considered. To accomplish this, the freedom ('F'), the actuation ('A'), and the actuation-freedom ('AF') directions taken from the mobility mapping in Table 3.2 are used to determine mobility directions for all actuators in the rules that dictate the motion of the parallel combination.

The freedom directions are determined by taking the freedom ('F') as the mobility direction for all actuators. The actuation direction may be different depending on which actuators are active. For a motion direction of the parallel combination to be an actuated direction, two mobility conditions for the actuators must both be met. First, the mobility of the active actuators is the union of the freedom ('F'), the actuation ('A'), and the actuation-freedom ('AF') directions. The inactive actuators' mobility is again set to the freedom ('F') direction. The second condition requires that at least one active actuator has actuation ('A') or actuation-freedom ('AF') in a mobility direction that meets one of the parallel direction rules. An example of a triangular triplet parallel FREE is shown in Figure 5.3.

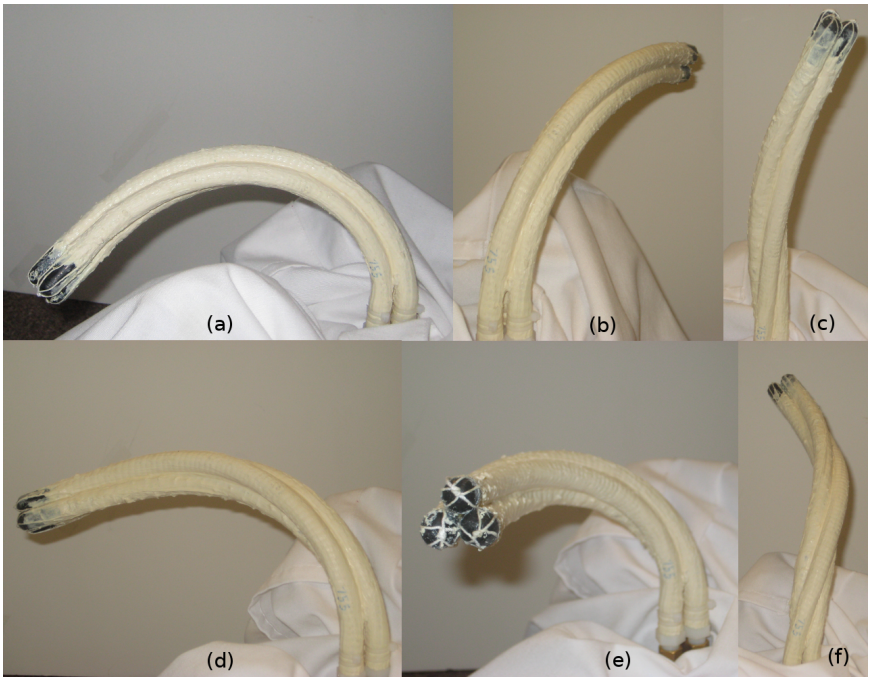

Figure 5.3: Deformation of a prototype with FREE types 13, 13 and 24 captured to indicate the combination of bending and screw motion. All images are looking in the same direction. Active actuators: (a) 1 (b) 2 (c) 3 (d) 1 and 2 (e) 1 and 3 (f) 2 and 3

5.2 Graphic User Interface

The parallel mobility rules provide a full mapping from all actuator type permutations to all parallel mobility combinations under all activation permutations. The challenge for kinematic synthesis remains, as there are 27,000 (30^3) possible coordinate dependant actuator configurations for the triangular triplet. A search algorithm is able to parse this large set to find viable actuator combinations that have a desired parallel mobility. A graphic user interface (GUI) has been created, allowing users to specify freedom and actuation directions that are desired for all actuation permutations. The GUI allows users to input the problem specifications: the desired freedoms, constraints, and actuations for all activation permutations. Figure 5.4 shows the GUI for a triangular triplet of actuators, with sample inputs selected and key features labeled. When "Find possibilities" is selected, the output shown in Figure 5.5(a) is displayed.

The first selection row of the input GUI in Figure 5.4 allows the user to select which freedom directions the manipulator should have. The second selection row is forbidden freedoms, which can also be described as required constraints. If a direction is not selected as necessary or forbidden, it is seen as not important, and can be either a freedom or a constraint. The third selection row contains necessary directions for the manipulator to

move when the first actuator (actuator numbering shown in Figure 5.2) is active. The fourth selection row determines the directions that are forbidden under the same activation pattern. All the following rows are configured in the same manner. Bend directions are expressed as polar coordinate angles in the plane perpendicular to the actuator's axial direction, with the orientation shown in Figure 5.2 (e.g. bend direction 1 is 60°).

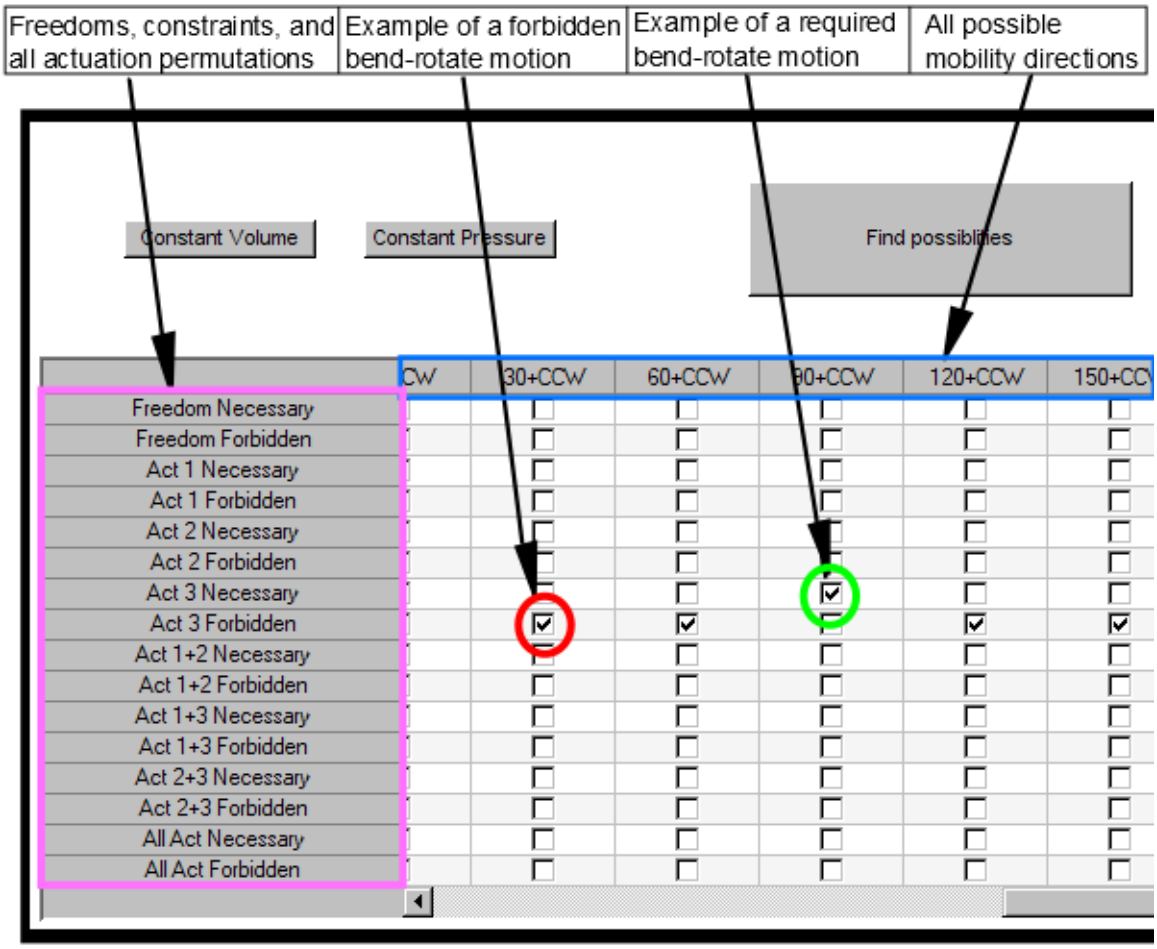

Figure 5.4: Screenshot of the GUI for triangular triplets of actuators. Sample inputs are selected, and the key features are labeled.

The output of the GUI, seen in Figure 5.5(a), displays all the viable solutions, one per column. Figure 5.5(b) shows a viable output solution in detail, with the first three rows displaying a diagram of the fiber orientations for the constituent actuators. The next row displays the freedom directions, and the following rows show the actuation directions for each permutation of actuator activation. Figure 5.5(a) demonstrates that there are a range of possible solutions for a given parallel FREE specification. Some solutions have no freedom directions (solutions 1-4, 6, and 7), which is shown by the lack of any mobility arrow in

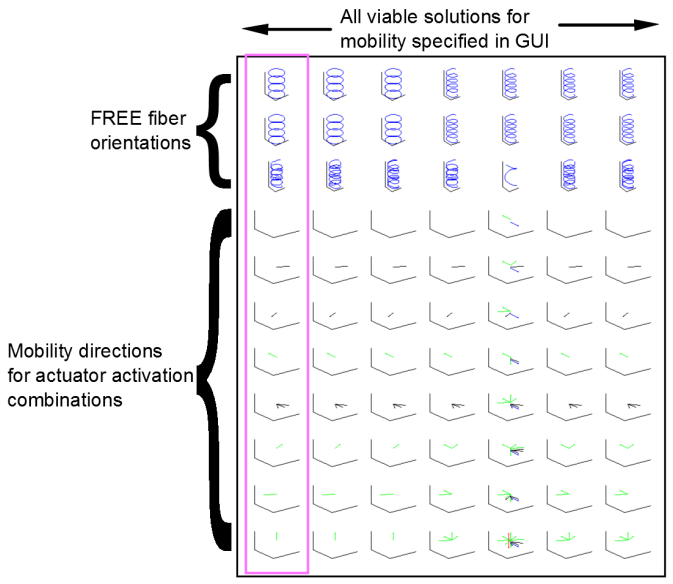

(a)

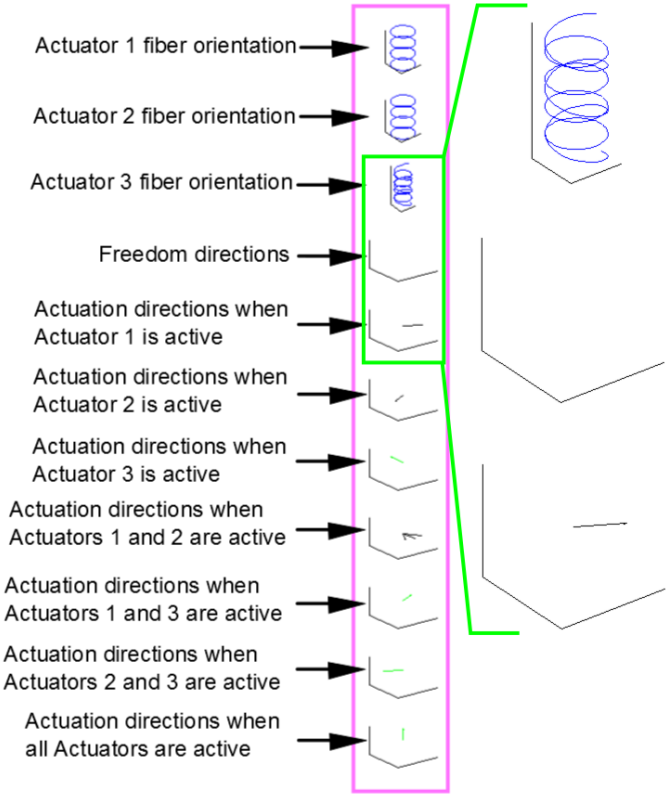

(b)

Figure 5.5: (a) Screenshot of the output of the GUI for triangular triplets of actuators with sample inputs selected. The green arrows are the bend directions of counter-clockwise bend-screw motions, black arrows are bend directions, and blue arrows are the bend directions of clockwise bend-screw motions. (b) Detailed view of GUI output components.

the freedom row, while others have multiple freedom directions (solution 5). This output allows the user to quickly determine not only the viable solutions, but also the detailed mobility of each one. An ideal solution can be selected from this chart, or if there are too many solutions, the GUI is still active, and the desired mobility can be refined.

5.2.1 Pick and Place Manipulator

An example of a pick and place manipulator demonstrates the ability of the GUI and embedded method to select viable solutions for practical problems. Pick and place manipulators are the arms attached to end effectors that can move across a desired workspace to transport objects from one location and orientation to another. They are commonly used in manufacturing automation and robotics. The use of a soft robotic pick and place manipulator could potentially enable close human-robot interaction in these fields.

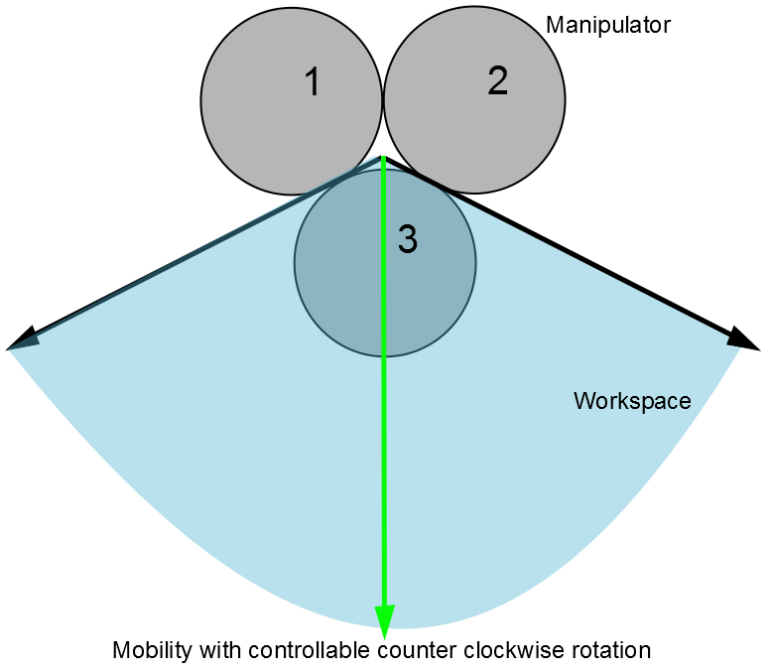

Figure 5.6: Top view of the pick and place manipulator case study. The desired workspace of bend directions and bend-screw motions are shown.

Figure 5.6 shows the desired actuation mobilities for the case study. The manipulator is mounted vertically, with a desired bend actuation throughout the range from 210° to 330°. The device should be able to perform a bend-screw motion of rotating counter-clockwise (CCW) while bending towards 270°. This combination of motions allows a large workspace and enables the target object to be rotated CCW a desired amount. This set of motions would be useful for a food processing manipulator that grabs food from random locations

on a conveyor belt and places it at the correct orientation in a package. These translate to parallel FREE design requirements of:

1. No freedom directions
2. Activating Actuator 1 enables actuation towards $330°$
3. Activating Actuator 2 enables actuation towards $210°$
4. Activating Actuators 1 and 2 enables actuation towards $240°$ through $300°$
5. Activating Actuator 3 enables actuation in a CCW bend-screw motion towards $270°$

Figure 5.7 shows the solutions that meet the given specifications. Each of the four columns is a different solution, and Figure 5.5(b) describes what each row represents. The first specification of no freedom directions is verified by row 4 (the first row showing mobilities), as there are no vectors indicating any freedom directions. Specification 2 can be seen in row 5, with a translational actuation direction pointing towards $330°$. Specification 3 can be seen in row 6, and specification 4 is shown in row 8, as there are actuation direction vectors pointing towards $240°$, $270°$, and $300°$. Row 7 is a green vector indicating a CCW bend-screw motion, and it points towards $270°$, thus verifying specification 5.

While all 4 solutions completely meet the specifications and provide viable options, rows 1 and 4 provide better solutions for this pick and place applications because when actuator 3 is active, the solutions in rows 2 and 3 have vectors pointing in multiple directions. This output indicates that the manipulator can move in the linear combination of two independent directions when actuator 3 is active. The resulting motion is under-constrained and is a function of the elastomer stiffness and external loads on the manipulator. Solutions 1 and 4 instead have only one actuation direction when actuator 3 is active, thus their motion is fully constrained to one direction, regardless of elastomer properties and external conditions. The user can input additional requirements into the GUI to narrow results until a practical number of viable solutions is found.

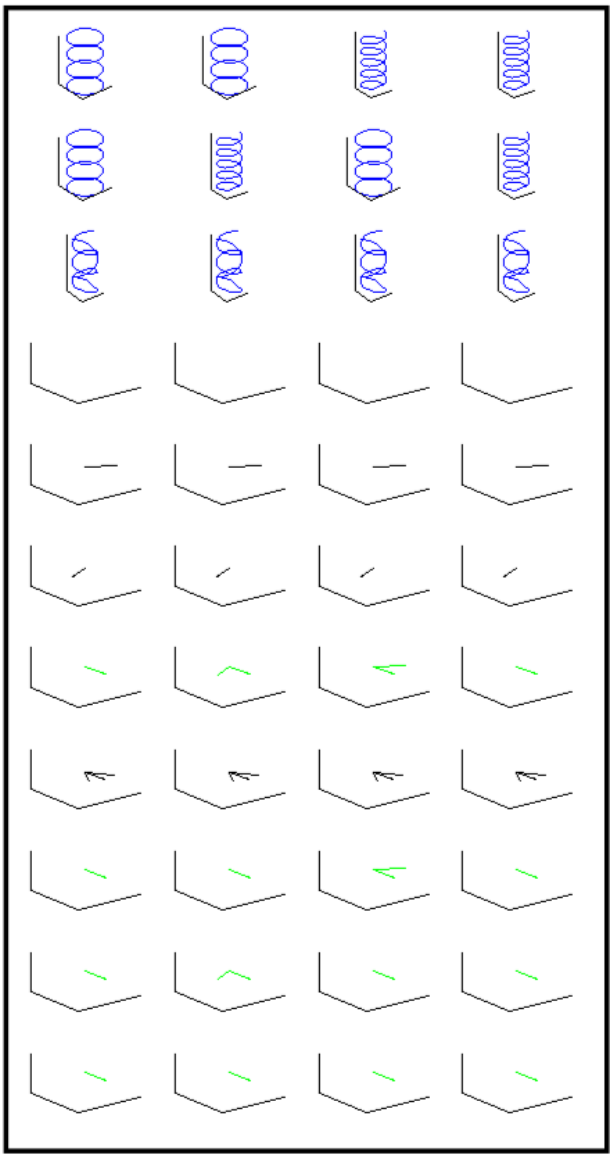

Figure 5.7: Screenshot of the GUI output for the pick and place manipulator case study. All solutions meet the specified criteria.

5.3 Soft Hexapod

A walking hexapod robot is created to demonstrate the application of the parallel FREE design method to practical uses. Hexapod (6-legged) robots have applications in search and rescue, exploration, military, infrastructure monitoring, and a range of other areas. Creating a lightweight, low cost, and robust robot that is adaptive to its environment poses a substantial challenge. Existing rigid link mechanisms with numerous actuators are heavy and expensive. Living hinge based hexapods (e.g. DASH robot [5]) add some compliance and bring down cost, but they still do not have high levels of environmental adaptability or the ability to independently control multiple degrees of freedom. Using parallel FREEs as the spine of a hexapod utilizes the inherent advantages of FREEs, such as low weight and cost, with high robustness and adaptability.

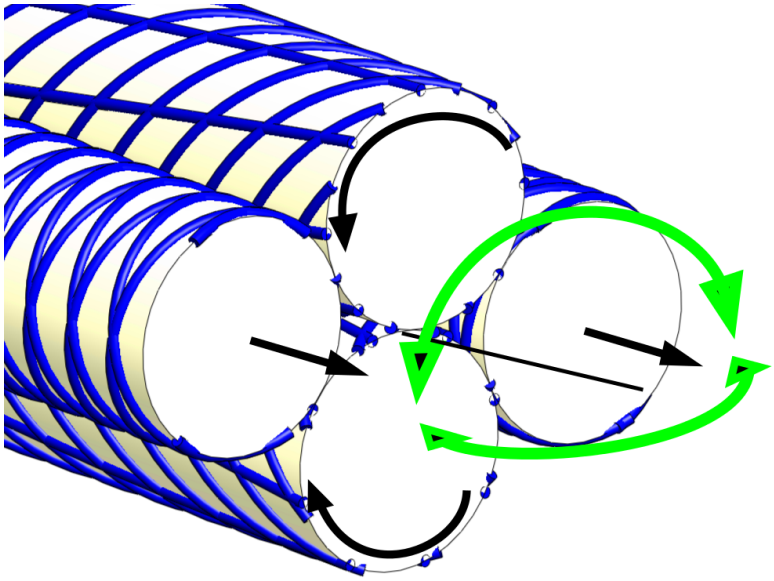

Figure 5.8: Fiber layout for a parallel FREE spine that generates a walking gait in a hexapod robot through selective pressurization of individual FREEs. Black arrows show actuation direction of individual FREEs, while green arrows show actuation directions of the combined parallel system.

To generate a walking gait in a sprawl posture robot, rotation about the spine in both directions is necessary for lifting the legs and applying normal force to the ground. Bending of the spine in the ground plane generates translation of the feet parallel to the ground. Bending left and right generates the necessary forward and backward translation for each foot. These requirements combine to necessitate a parallel FREE system for the spine that allows for actuation in both rotation and bending, each in two directions.

Four FREEs are combined in parallel. To generate rotation, two FREEs are placed

Figure 5.9: Hexapod robot with a parallel FREE spine that generates a walking gait through selective pressurization of individual FREEs.

above and below the center of the spine axis. These actuators must actuate in rotation, not resist the bending necessary for the other two actuators, and not elongate or contract substantially, as that would adversely affect the bending motion created by extension or compression of the other two actuators. To generate rotation for the CCW direction, a type 6 actuator from Figure 3.11 near the $\alpha = 54.7°$, $\beta = 0°$ point is selected. This generates mostly rotation, with minimal elongation, while allowing for bending. A type 7 actuator is selected to generate the opposing rotation. The bending actuators are placed on either side of the center of the spine, thus extension or elongation generate a bending motion. Elongation was chosen to ensure the actuation would not buckle the rotational FREEs. Type 18 FREEs have been selected near the $\alpha = 90°$, $\beta = 90°$ point. The resulting parallel FREE design is shown in Figure 5.8. The resulting robot is shown in Figure 5.9. Additional research is required to obtain a robust walking robot from this design concept, including an understanding of the dynamics and controls of FREEs, tuning of the walking gait, and creation of a self-contained pressure source.

5.4 Summary

The challenge this chapter addressed was synthesizing FREEs in parallel to obtain a desired mobility set. There are three main contributions of this chapter:

1. The development of a universal set of rules for determining the parallel mobilities of FREE structure with any set of fiber angles in triangular configurations.
2. The creation of a GUI that maps the desired mobility to a full set of viable solutions.
3. Application example of a walking robot using FREEs to generate a flexible actuated spine.

CHAPTER 6

Helices and Bending

This study expands on the previous chapters by adding a single fiber to the two fiber family FREE structure. The two fiber family FREE is fully constrained to one degree of actuation, with the exception of $\alpha = \beta$ configurations and those along the line seen in Eq. 2.9. All configurations also have a degree of freedom in bending, with the exception of configurations with axial fibers. For configurations that are not in one of these exception groups, the addition of the single fiber will utilize the degree of freedom in bending and cause a controlled bending when pressurized. The angle of the added single fiber, referred to as γ, and the rotation of the FREE from the two families of fibers will cause the bending direction to spiral around the FREE. The resulting shape of this new manipulator will be a helical pattern. Pure bending is still possible, as it is simply a spiral with a helix angle of zero.

The first section of this chapter develops the kinematic model, including the volumetric effects, for helical FREEs. The second section displays select regions of the design space spanned by these FREEs. The third section experimentally verifies multiple points in the design space to validate the kinematic model. The final section explores the application of helical FREEs to pipe inspection robots.

6.1 Kinematic Model

The addition of a single fiber causes a FREE with two families of fibers to bend due to the additional constraint imposed by the single fiber. Since this is a single fiber, rather than a family of fibers, the equation for the inextensibility of the fiber will be different from the one shown in Eq. 2.1 due to the FREE's ability to bend toward the fiber constraint. Figure 6.1 shows how the axial extension component of the fiber length constraint is modified when there is a single fiber added. The two families of FREEs will determine λ_1, λ_2, and δ, seen in Figure 6.1(a). The addition of the single fiber will interact at a single point for any given cross-section, shown in Figure 6.1(b) as point "S". λ_1, λ_2, and δ combine with

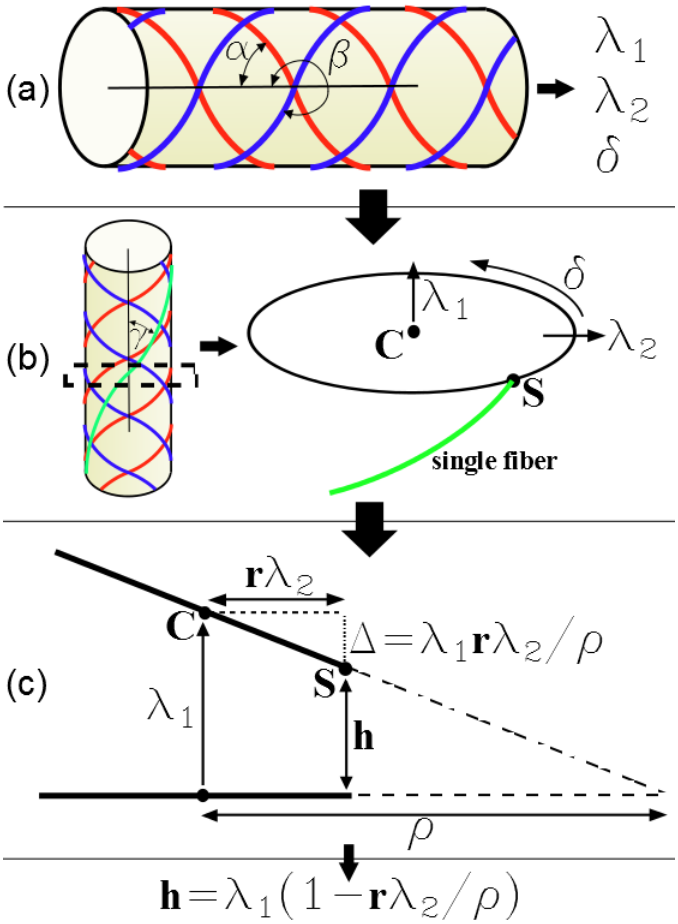

Figure 6.1: Derivation of the effect of a single fiber on bend radius ρ. (a) The two families of the fibers determine stretch ratios λ_1, λ_2, and rotation δ. (b) The resulting free body diagram of a small section when a single fiber is applied to the two fiber family FREE. (c) Diagram of a length normalized section of the FREE, showing the relationship between ρ and change in displacement in the axial direction.

the bend radius (ρ), as shown in Figure 6.1(c), to determine the length normalized axial extension at the single fiber. Equation 6.1 is the fiber inextensibility equation for the single fiber. It is derived in the same manner as Eq. 2.1, by setting the length before and after deformation to be equal. Equation 6.2 is Eq. 6.1 rewritten with ρ as the dependent variable, and α, β, γ, λ_1, λ_2, and δ as the independent variables. Equation 6.3 further refines ρ to an expression that is only dependent on the parameters of α and β, γ, and the operational variable of λ_1. This simplification is done using the equations for λ_2 and δ (Eqs. 2.4 and 2.5 respectively). Equation 6.4 shows curvature, κ, which is the inverse of ρ. With these equations in place, the effect of α, β, and γ on the relationship between axial expansion and bending is established.

$$\lambda_1^2(1-\frac{r\lambda_2}{\rho})^2(\cos(\gamma))^2+\lambda_2^2(\sin(\gamma))^2(\frac{\theta^*}{\theta})^2=1 \tag{6.1}$$

$$\rho=\frac{r\lambda_1\lambda_2}{\lambda_1-\sqrt{(\sec(\gamma))^2-\lambda_2^2(\tan(\gamma))^2(\tan(\gamma)+\frac{r\delta}{l})^2}} \tag{6.2}$$

$$\rho=\frac{r\lambda_1 X}{\sin(\alpha-\beta)\lambda_1-\sqrt{(\sin(\alpha-\beta)\sec(\gamma))^2-(\tan(\gamma))^2(\tan(\gamma)X+W)^2}} \tag{6.3}$$

$$\kappa=\frac{\sin(\alpha-\beta)\lambda_1-\sqrt{(\sin(\alpha-\beta)\sec(\gamma))^2-(\tan(\gamma))^2(\tan(\gamma)X+W)^2}}{r\lambda_1 X} \tag{6.4}$$

$$where:$$

$$X=\frac{\alpha}{|\alpha|}\cos(\beta)\sqrt{1-\lambda_1^2(\cos(\alpha))^2}-\frac{\beta}{|\beta|}\cos(\alpha)\sqrt{1-\lambda_1^2(\cos(\beta))^2}$$

$$W=\frac{\beta}{|\beta|}\sin(\alpha)\sqrt{1-\lambda_1^2(\cos(\beta))^2}-\frac{\alpha}{|\alpha|}\sin(\beta)\sqrt{1-\lambda_1^2(\cos(\alpha))^2}$$

The relationship between the extension (λ_1) and the change in volume is derived, as the controlled variable is volume, not λ_1. Equation 6.5 shows λ_1 as a function of λ_2, which is derived by rewriting Eq. 2.4. Equation 6.6 is an implicit function defining the relationship between λ_1 and the volume of the FREE. This is derived by substituting the value of λ_2 into Eq. 6.5. λ_2 is found by rewriting Eq. 2.7 as $\lambda_2^2=\frac{V}{\lambda_1\pi r l}$. Equation 6.6 can be solved explicitly for λ_1 as a function of volume. The resulting equation is too large to display. The explicit form of Eq. 6.6 can be substituted into Eq. 6.3 to derive ρ as a function of volume; the resulting equation is again too large to display.

$$\lambda_1 = \frac{\sqrt{2\lambda_2^2((\cos(\alpha))^2 + (\cos(\beta))^2) - (\sin(\alpha+\beta))^2 - \lambda_2^4(\cos(\alpha-\beta))^2}}{2\cos(\alpha)\cos(\beta)\lambda_2} \tag{6.5}$$

$$-\frac{4V(\cos(\beta))^2(\cos(\alpha))^2}{\pi r^2 l}\lambda_1^3 - (\sin(\alpha+\beta))^2\lambda_1^2 + ...$$
$$\frac{2V((\cos(\alpha))^2 + (\cos(\beta))^2)}{\pi r^2 l}\lambda_1 - \frac{V^2(\sin(\alpha-\beta))^2}{\pi^2 r^4 l^2} = 0 \tag{6.6}$$

The deformed shape of the FREE is a helix, and the two key parameters of the helix for many applications are the helix angle, ϕ, and the helix radius, R. Equation 6.7 defines ϕ in terms of the rotation caused by the two families of fibers (δ), the number of rotations of the single fiber (θ), the bend radius (ρ), and the axial length (l) of the FREE. Equation 6.8 defines R using these same variables. Equation 6.9 shows how θ is derived, and it takes the same form as Eq. 2.2. Equation 6.10 shows ϕ as a function of parameters α, β, and γ, and variable λ_1. ϕ is further modified to be a function of α, β, and γ, and the control variable, volume, by substituting in Eq. 6.6 and Eq. 6.3 into Eq. 6.10. The detailed equation for R is computed in a similar manner, but these equations are too large to display.

$$\phi = \arctan(\frac{\delta_{eff}}{l\kappa}) = \arctan(\frac{(\delta+\theta)\rho}{l}) \tag{6.7}$$

$$R = \frac{\rho}{1+(\frac{\delta_{eff}}{l\kappa})^2} = \frac{\rho}{1+(\frac{(\delta+\theta)\rho}{l})^2} \tag{6.8}$$

$$\theta = \frac{\tan(\gamma)l}{r} \tag{6.9}$$

$$\phi = atan(\frac{\lambda_1(W + X\ \tan(\gamma))}{\sin(\alpha-\beta)\lambda_1 - \sqrt{(\sin(\alpha-\beta)\sec(\gamma))^2 - (\tan(\gamma))^2(\tan(\gamma)\,X + W)^2}}) \tag{6.10}$$

$$where:$$

$$X = \frac{\alpha}{|\alpha|}\cos(\beta)\sqrt{1-\lambda_1^2(\cos(\alpha))^2} - \frac{\beta}{|\beta|}\cos(\alpha)\sqrt{1-\lambda_1^2(\cos(\beta))^2}$$
$$W = \frac{\beta}{|\beta|}\sin(\alpha)\sqrt{1-\lambda_1^2(\cos(\beta))^2} - \frac{\alpha}{|\alpha|}\sin(\beta)\sqrt{1-\lambda_1^2(\cos(\alpha))^2}$$

6.2 Design Space

There are three main design variables of the helical FREEs: α, β, and γ, and one operational variable of normalized volume (normalized to the unactuated volume). The axial length of the FREE does not affect the helix angle or helix radius. Radius of the FREE does not affect the helix angle and is linearly proportional to the helix radius. Material and geometric properties determine stiffness, which likely have some effect on the motion, but are left to future work. Assumptions made in Section 2.1 remain in effect. While it is difficult to simultaneously visualize the effect of four independent variables on the output values, plots have been created to illustrate various sections of the design space.

Figure 6.2 explores how the helix angle, ϕ, is effected by the parameters α and β and the operational variable of volume. This is done by arbitrarily fixing the remaining variable, γ, at a value of 10°. The volume is set at five different values, and α and β are plotted over their entire non-redundantly labeled range. The plot shows α and β on the X and Y axes and the resulting ϕ on the Z axis. This is done for the five different volumes, shown in different colors. Figure 6.3 explores how the helix radius, R, depends on the same independent variables (α, β, and volume). The helix radius has been normalized for FREE radius in the plot. The single fiber angle, γ, is arbitrarily set at 7°. Blank regions with no color are regions where fiber buckling occurs, thus creating underconstrained motion and preventing helix variables from being determined.

Figures 6.2 and 6.3 show the wide range of helix angles and radii that are possible, even without changing the angle of the single fiber. With an increased volume, the helix angle in Figure 6.2 ranges from $\frac{\pi}{2}$ to $\frac{-\pi}{2}$ depending only on the angles of the families of fibers. Some regions, such as those seen for α and β both greater than zero, have a helix angle that is highly sensitive to volume, while other regions have minimal sensitivity. The helix radius exhibits similar properties, with the region where α and β are both greater than zero showing high sensitivity to volume changes. The dependence on volume is highly non-linear, with some regions expanding in helix radius and then contracting as the volume is increased.

Figure 6.4 illustrates the effects of the fiber angles β and γ on ϕ. To do this, α (one of the two families of fibers) is arbitrarily fixed at 65° and volume increase is arbitrarily fixed at 10%. The resulting contour plot shows the values of ϕ with respect to β on the X axis and with respect to γ on the Y axis. The large range of possible ϕ values, even with both α and volume fixed, can be seen in the plot. The sensitivity of the helical FREE configuration to changes in fiber angle can also be readily understood. Small errors are seen in the region with β between 0° and 5°, as the single fiber passes through the axial configuration.

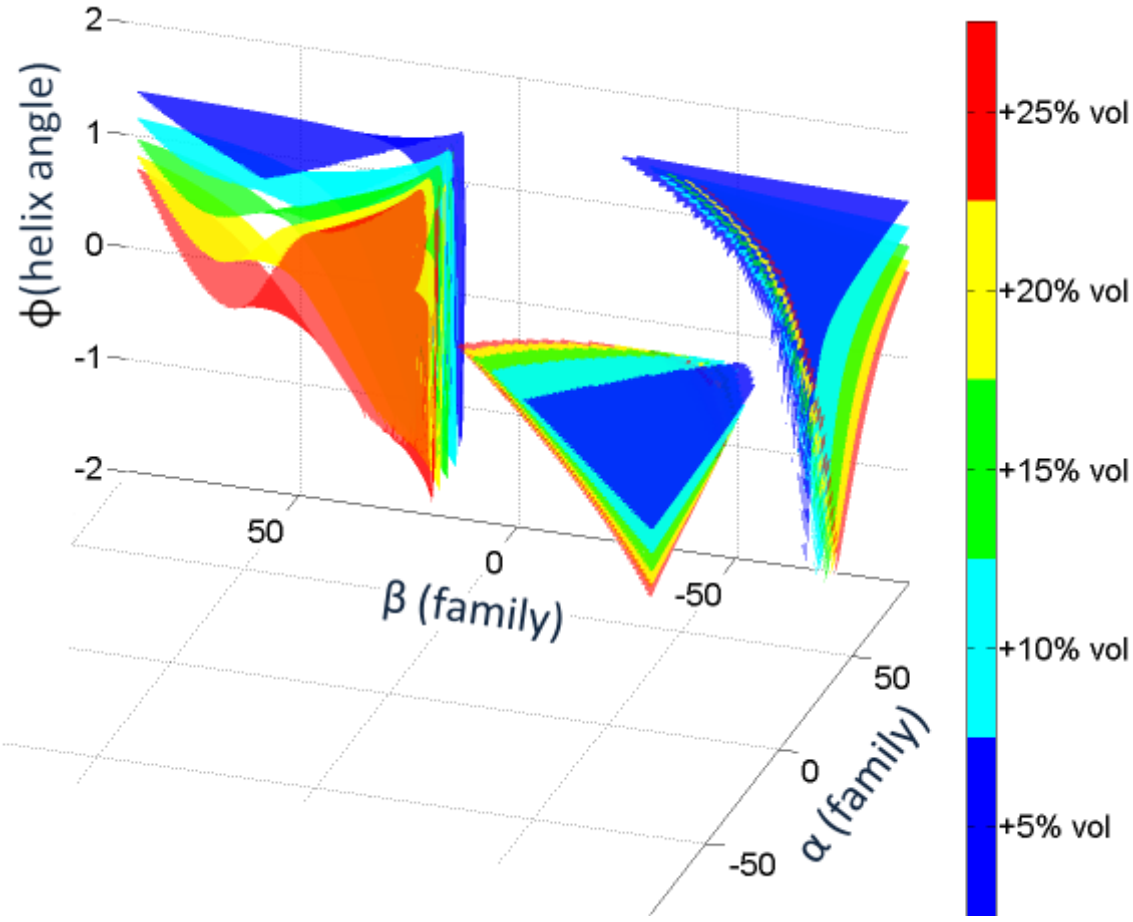

Figure 6.2: The effect of percent volume increase and fiber angles α and β (in degrees) on the device's helix angle, ϕ (in radians). The single fiber, γ, is set at 10°, and the radius of the device is set at 6mm. Five volume change values: +5%, +10%, +15%, +20%, and +25% are set and the resulting ϕ as a function of α and β is plotted.

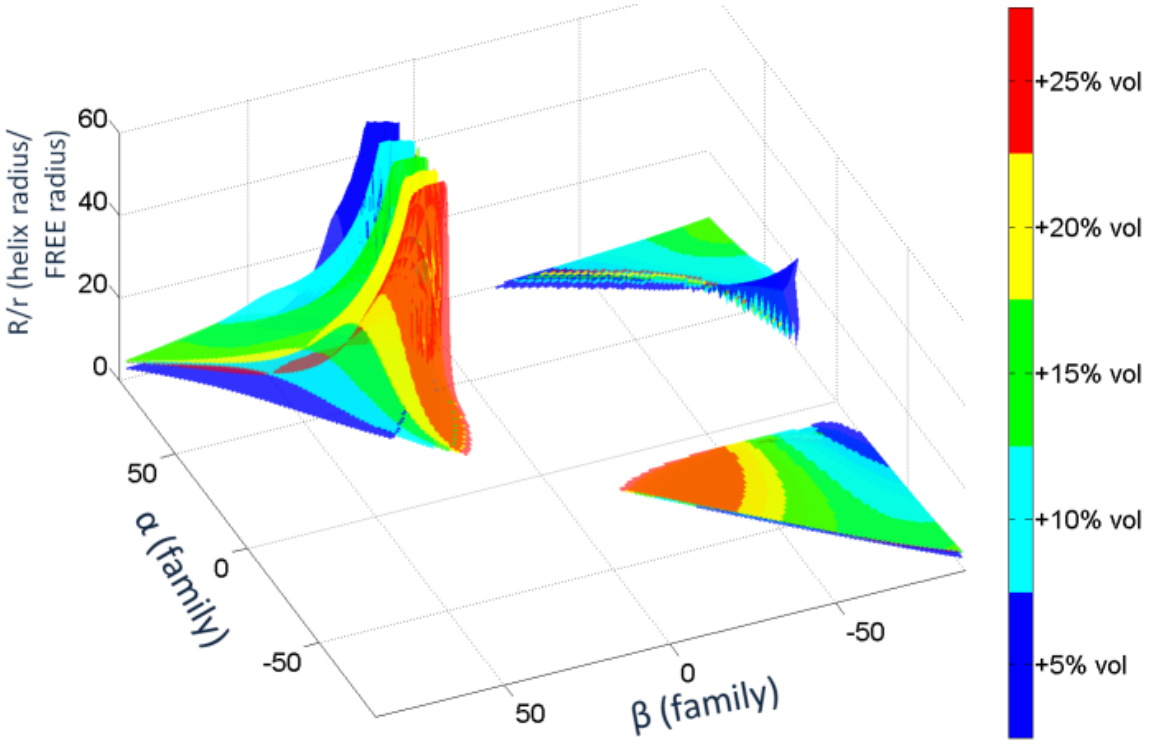

Figure 6.3: The effect of percent volume increase and fiber angles α and β (in degrees) on the device's helix radius (relative to the radius of the FREE), R/r (normalized radius). The single fiber, γ, is set at 7°, and the radius of the device is set at 6mm. Five volume change values: +5%, +10%, +15%, +20%, and +25% are set and the resulting R/r as a function of α and β is plotted. Plot is clipped above at 50.

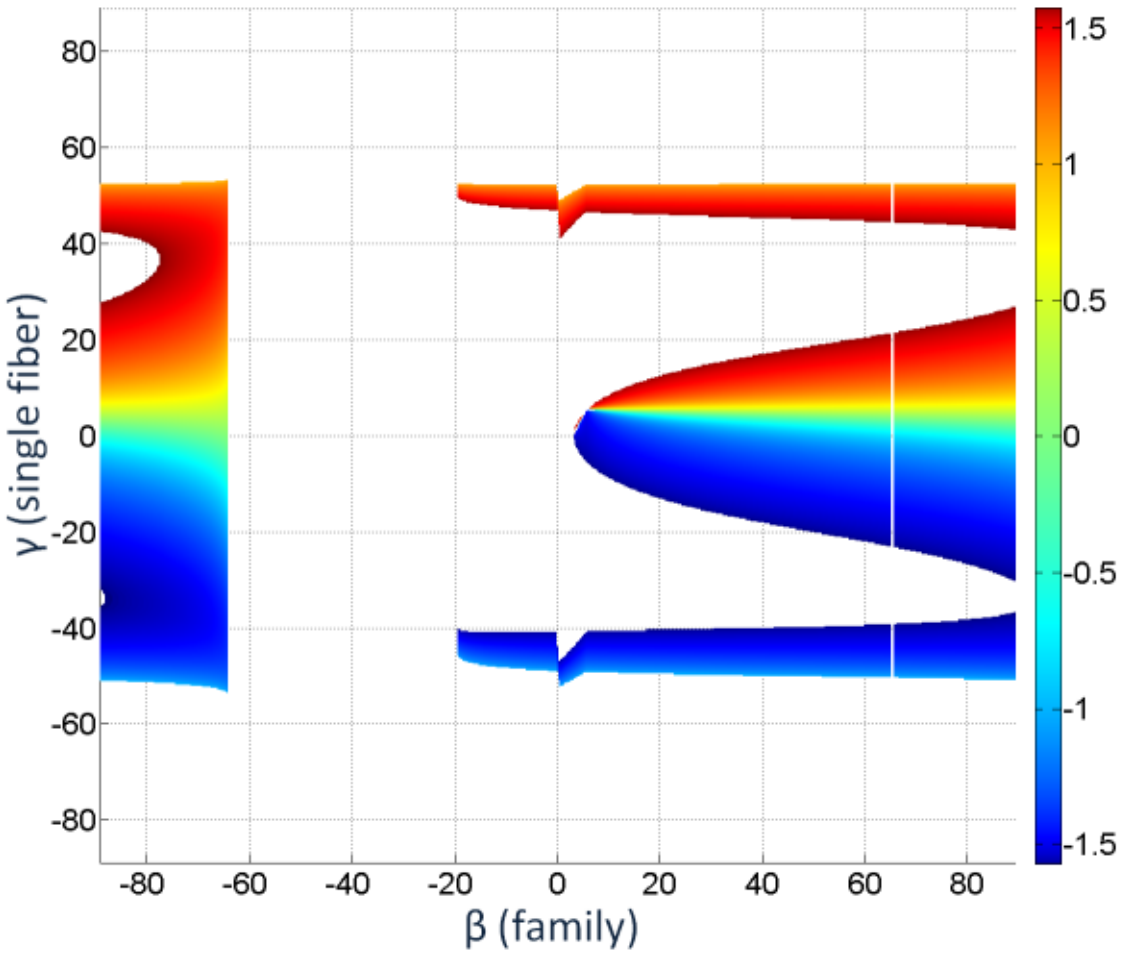

Figure 6.4: Helix angle, ϕ (in radians), across fiber angles β and γ (in degrees). One of the families of fibers, α, is set at $65°$, volume change is set at +10%, and the radius of the device is set at 6mm

6.3 Experimental Validation

To verify the accuracy of the model in predicting the kinematics of the helical FREEs, multiple prototypes were fabricated and analyzed. These prototypes were constructed across a diverse selection of α, β, and γ. The helix radius was determined through measurement, while the helix angle was determined by combining this radius with the pitch of the helix. The first prototype tested has fibers at $\alpha = -70°$, $\beta = -30°$, and $\gamma = 1°$. The prototype has a FREE radius of 6 mm and was inflated to a volume increase of 35% ($\frac{V_{final}}{V_{initial}} = 1.35$). The analytical models predict this configuration and inflation to have a body helix angle of $73.1°$ and coil with a radius of 4.46 mm. The resulting device is shown in Figure 6.5. The measured body helix angle of the prototype is $59.4°$. The radius is 9.3 mm. The helix angle has an error of 18.7%.

Figure 6.5: Helical FREE with $\alpha = -70°$, $\beta = -30°$, and $\gamma = 1°$. The helical FREE prototype has a body radius of 6 mm and was inflated to a volume increase of 35%. The image is the inflated helical FREE (image rotated 90 degrees, gravity going right).

The second prototype has fibers at $\alpha = 88°$, $\beta = -60°$, $\gamma = 10°$, a FREE radius of 6 mm, and was inflated to a volume increase of 30%. The analytical models predict this configuration and inflation to have a body helix angle of $60.94°$ and coil with a radius of 5.74 mm. The resulting device is shown in Figure 6.6. The measured body helix angle of the prototype is $55.7°$. The radius is 11.43 mm. The helix angle has an error of 8.6%.

The third prototype tested has fibers at $\alpha = 65°$, $\beta = -80°$, and $\gamma = 5°$, a FREE radius of 6 mm, and was inflated to a volume increase of 15%. The analytical models predict this configuration and inflation to have a body helix angle of $8.13°$ and coil with a radius of 31.9 mm. The resulting device is shown in Figure 6.7. The measured body helix angle of the prototype is $9.1°$. The radius is 50.8 mm. The helix radius has an error of 11.9%.

These dimensions are highly sensitive to prototype fabrication and material assumptions, such as inextensibility of the fibers and exact fiber angles, thus providing opportunities for deviations from values derived from the model. While the helix angles matched rather closely, the helix radius had larger errors. This is likely caused by the single fiber not having an infinite stiffness as the model assumes, thus allowing axial extension without

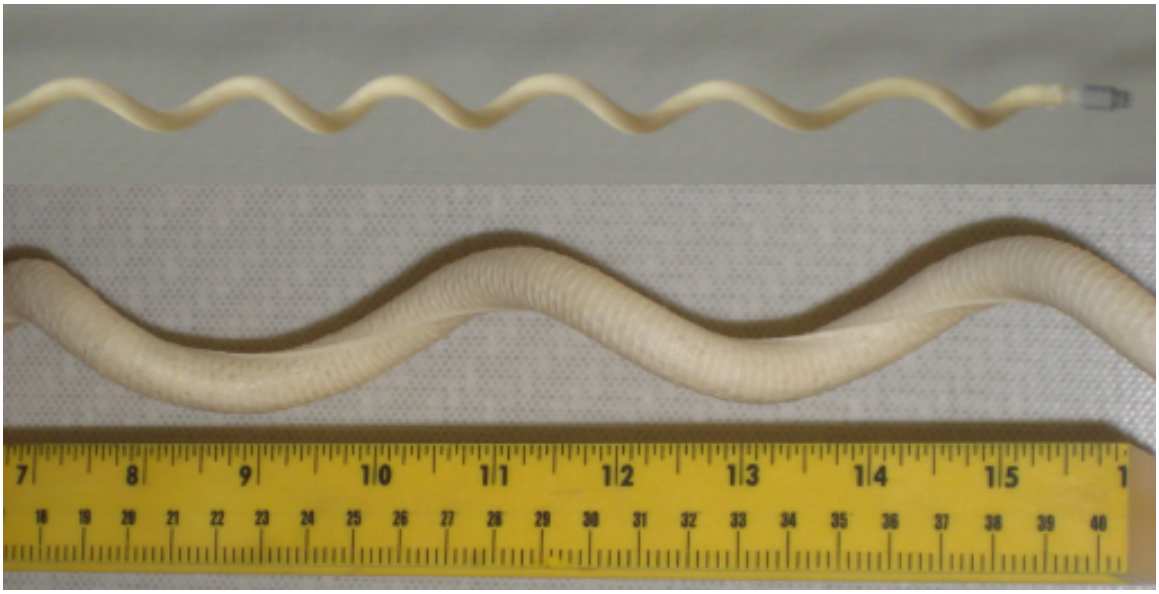

Figure 6.6: Helical FREE with $\alpha = 88°$, $\beta = -60°$, and $\gamma = 10°$. The helical FREE prototype has a body radius of 6 mm and was inflated to a volume increase of 30%. Top image is the full helical FREE (image rotated 90 degrees, gravity going right), and the bottom image compares the helical FREE to a measuring device.

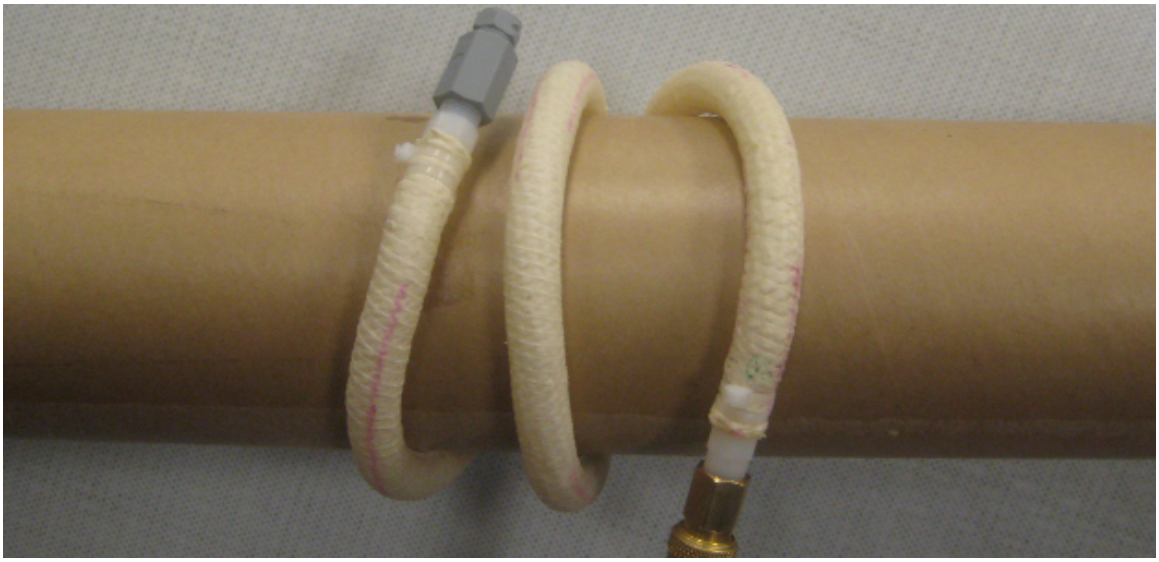

Figure 6.7: Helical FREE with $\alpha = 65°$, $\beta = -80°$, and $\gamma = 5°$. The helical FREE prototype has a body radius of 6 mm and was inflated to a volume increase of 15%. The image is the inflated helical FREE (image rotated 90 degrees, gravity going right).

bending. This would result in a larger helix radius than the one predicted, which is seen in all three prototypes.

Images of additional helical FREE manipulators are shown in Figure 6.8.

Figure 6.8: Helical FREEs demonstrating helical shape generation, rough object grasping, small object grasping, asymetric object grasping, and pipe anchoring.

6.4 Pipe Inspection

Pipe inspection is a critical component of maintaining infrastructure in a range of industries. Municipal water and sewage, gas and oil energy, industrial and commercial plumbing, and chemical refinement all rely on an expansive network of pipelines that require inspection during the construction and operation phases. In the United States alone, there are over 2.5 million miles of hazardous liquid and natural gas pipeline, of which roughly 2 million miles is natural gas distribution pipeline [59] (305,000 miles which is high pressure, large diameter gathering and distribution [2]). There are 800,000 miles of water delivery pipelines and 600,000 to 800,000 miles of sewer pipeline [58]. The United States has 240,000 water main breaks, and 75,000 sewer overflows every year, leading to the discharge of 3 to 10 billion gallons of untreated sewage, resulting in 5,500 illnesses across the country [3]. A

better method for the delivery of non-destructive testing methods (e.g. visual inspection) in these extensive pipeline networks is a critical health, safety, and economic issue.

There are a wide range of pipe inspection mechanisms in use and under development. For shorter distances in simpler pipeline networks, a cable can be fed into the pipe, but longer distances and more complex networks present the need for a more complex solution. Two main approaches have been used. The first approach uses a device that is centered in the pipe and presses treads or wheels outward towards the walls of the pipe. This approach has trouble with changing pipe diameters and pipe junctions, limiting its benefits to primarily simple pipeline systems. The second major approach is to use a snake-like mechanism that forms a helix or sinusoidal wave pattern to generate contact force between the inspection mechanism and the pipe. The approach, a helical snake, provides a more compact robot that can better navigate changing pipe diameters and junctions. Its limited size and smaller obstruction of the pipe presents the opportunity to insert the inspection mechanism into an access port while the pipeline is still active, rather than shutting down operations to perform inspection.

While snake-like inspection devices have many advantages, they have challenges that still need to be addressed. There are currently two main ways to form the helical or sinusoidal pattern necessary to produce contact force on the walls. Those are actively holding the actuator at the correct position and using a non-backdrivable mechanism. This presents the first major challenge of a trade-off between energy efficiency and responsiveness. The active holding of the actuator uses large amounts of energy, while the non-backdrivable mechanism is unable to passively respond to any changes in pipe diameter or direction. The lack of responsiveness presents problems with non-flush mating of pipe segments, trapped debris, and corroded pipe segments. The second major challenge is the use of segmented mechanisms, which only roughly represent the round pipe cross-sections, leading to force concentrations on the pipes. The third challenge is producing a lightweight solution. For applications that require traversing vertically or on slopes, a lightweight device reduces energy use. A fourth challenge is the cost and questionably reliability of producing these multi-segmented devices with complex mechanisms. These challenges drive the need for a low cost, lightweight mechanism that can form and passively hold a desired helical shape while maintaining flexibility.

Using the equations developed in this chapter, a helical FREE was designed that functions as the main structural component of a pipe inspection device. The body can alter the shape of the device from a perfectly straight cylinder to a highly coiled helix, with the ability to remain at any intermediate configuration. Wheels or treads, inspections tools such as cameras, and drive motors can be attached to this helical body to create a full device. A

helically expanded FREE is seen in a transparent 2.25 inch inner diameter pipe in Figures 6.9 and 6.10, and the same device inflated to a different volume is shown in a transparent 3 inch inner diameter pipe in Figures 6.11 and 6.12.

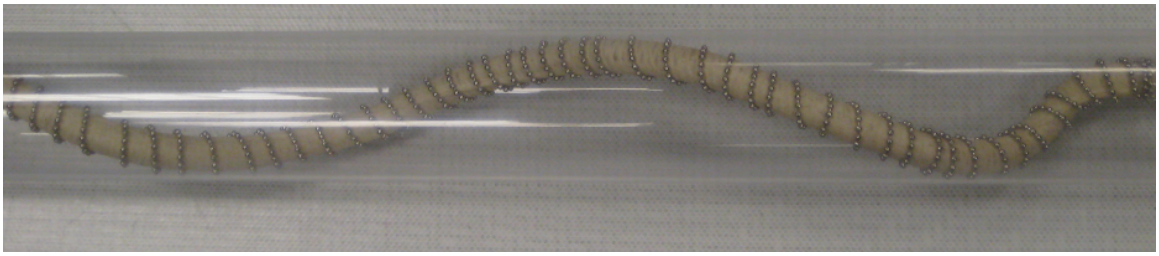

Figure 6.9: Helical FREE pipe inspection device is inflated in a 2.25 inch inner diameter clear pipe, viewed from the side. The device has fiber angles of 88° and -80° for the families of fibers and 5° for the single fiber.

Figure 6.10: Helical FREE pipe inspection device is inflated in a 2.25 inch inner diameter clear pipe, viewed inside the pipe. The device has fiber angles of 88° and -80° for the families of fibers and 5° for the single fiber.

Inflatable devices have been used to expand to different pipe diameters in pipe inspection devices [68] [17], yet these devices are not helical or snake-like and consequently obstruct the fluid flow. The proposed mechanism uses inflation to form a desired helical or sinusoidal shape, rather than simply expanding outward to the diameter of the pipe. Many

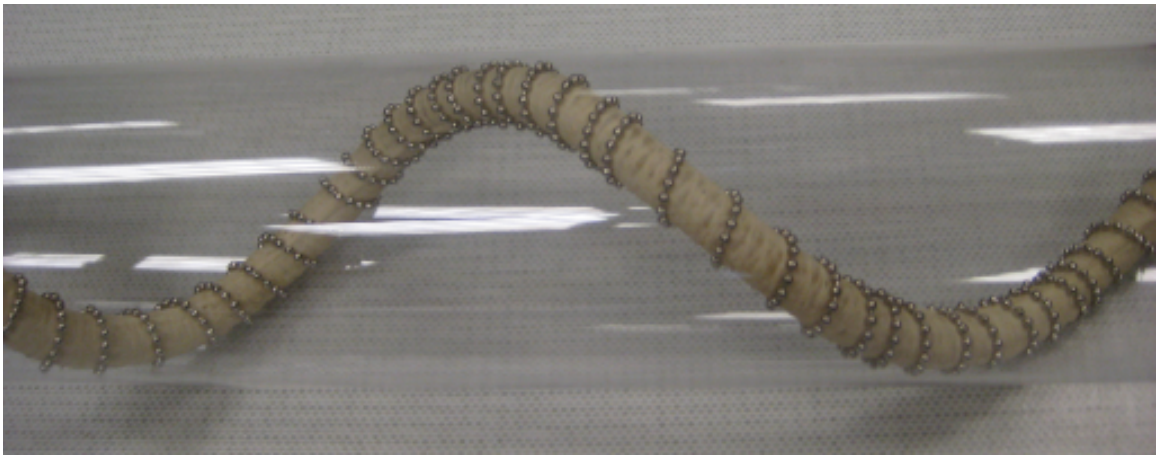

Figure 6.11: Helical FREE pipe inspection device is inflated in a 3 inch inner diameter clear pipe, viewed from the side. The device has fiber angles of 88° and -80° for the families of fibers and 5° for the single fiber.

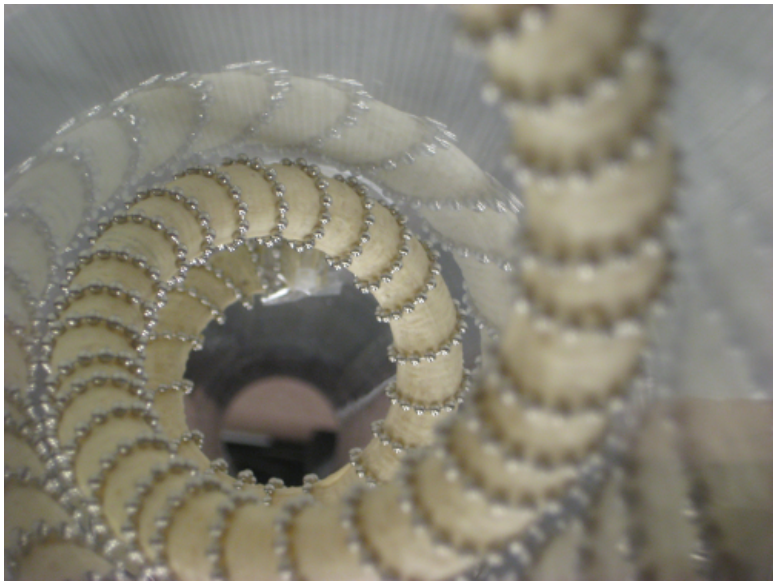

Figure 6.12: Helical FREE pipe inspection device is inflated in a 3 inch inner diameter clear pipe, viewed inside the pipe. The device has fiber angles of 88° and -80° for the families of fibers and 5° for the single fiber.

of these inflatable designs do not have the ability to attach wheels or treads to the expanding members, limiting the device's locomotion. There have been a substantial number of studies on snake robots; many are captured in a review by Hirose et al. [26]. Takayama and Hirose demonstrated some applications and advantages of a helical snake motion for locomotion and manipulation, and they addressed the fabrication of a fluid driven snake [76]. The resulting design, however, was segmented, complex, heavy, and not continuum. Suzumori presents multi-segment manipulators with limited helical motion capabilities [73]. There have been other fluid driven cylindrical manipulators that are only able to obtain bending. The use of helical FREEs enables the design of lightweight, simple, low cost manipulators that passively hold their shape while maintaining flexibility. An understanding of the affect of fluid flow, material degradation in harsh environments, dynamic responses to perturbations, attachment methods for outside objects to FREEs, and numerous other areas are necessary to realize this concept in an industrial pipe inspection application.

6.5 Summary

This chapter illustrated a kinematics approach to determining the deformation pattern of continuum helical FREE manipulators. The motion of the helical FREE mechanism was solved as a function of the contained volume for any given fiber angle α, β, and γ, as well as for FREE radius. Visual representations of portions of the design space are shown, and three test cases were fabricated and actuated to show their fit with the analytical model. Nearly all of the applications require an understanding of how the design parameters of α, β, γ, and FREE radius, as well as the operational parameter of volume, affect the deformation patterns. The primary contributions of this chapter are:

1. Determination of the kinematic deformation patterns for FREEs with two families of fibers and an additional single fiber.

2. Creation of simple equations that can be used to both analyze and synthesize helical FREE fluidic manipulators.

3. Demonstration of potential applications that were previously inaccessible due to a lack of lightweight, simple, low cost, high power density helical soft robots.

CHAPTER 7

Conclusion, Contributions, and Future Work

7.1 Conclusions

Elasto-fluidic systems use fluid as a medium to transfer forces and motion within a flexible body. Looking to nature, many organisms use fiber-reinforced elastomeric enclosures (FREEs) to control the mechanics of these structures. Engineers have attempted to utilize this design with the McKibben actuator, a FREE that uses fluid pressure to obtain extension and contraction. Both the biological organisms and the engineered solutions use the strength of the fibers, the flexibility of the elastomeric material, and the high compressive load capability of the fluid to produce systems with high power density, resilience, adaptability, and scalability. The engineered solutions present low cost fabrication, while biological organisms show the ability to generate a wide range of forces, motions, and forms. While these systems provide all these advantages, they are rarely used by engineers, in part due to the absence of a generalized understanding of their mechanics.

This dissertation discovered an entire design space of previously unknown elasto-fluidic systems. The existing knowledge was limited to only small subsets of the design space, such as McKibben actuators, impeding engineers from utilizing the immense functionality that the diversity of an entire design space provides. Beyond discovering this design space of fiber-reinforced elasto-fluidic systems, this dissertation presents analysis, modeling, testing, and a design methodology and tools for their mechanics. The conclusion drawn from this research is that simple mathematical models that are derived from the underlying kinematics of the fibers determine the mechanical behavior of fluidic FREEs. With the mathematical models and their respective graphical representations, a designer can not only analyze a FREE, but also synthesize one with desired mechanics.

7.1.1 Summary of FREE Mechanics

The modeling of the kinematics of FREEs with two families of fibers in Chapter 2 shows the relationship between the change in length of a FREE with its change in radius and with its rotation. From these relationships, the screw pitch of a FREE undergoing deformation is determined. The screw pitch captures a wide range of motions from pure extension (screw pitch of infinity) to pure rotation (screw pitch of zero) to coordinated extensions and rotations with finite screw pitch. The experimental testing verifies these models, also presenting the helix angle as another way to represent the screw deformation. These kinematics combine to provide an analysis and synthesis method for creating two fiber family FREEs with desired deformation kinematics.

Chapter 3 expands on the kinematic model to produce simple mathematical models for the volume displaced by output motions. The equations and figures for volumetric transduction under screw motion capture many of the important aspects of the FREE mechanics. Zero volume change are freedom directions, maximum volume change are actuation directions, and negative volume change are constraint directions. This mapping captures the range of behaviors across the range of deformation directions. Section 3.4 groups and descretizes the kinematics and volume models to provide a design tool to quickly and easily search the design space. This tool enables a designer to intuitively synthesize a FREE with desired behavior, without needing to understand the underlying equations or complexity of the screw motion volumetric transduction.

The force and moment generation of these FREEs is important for many applications, and chapter 4 creates a closed form analytical equation that a designer can readily use. Experimental testing determined the simplifying assumptions that best model force and moment generation; unconstrained kinematic models best derive moment generation, while constrained rotation kinematic models best derive force generation. Complex actuators with coordinated force and moment can be created by combining the equations or plots. A case study of an arm torsion orthosis shows the utility of the mechanics equations and design tools in developing designs for practical applications.

Parallel combinations of FREEs present a wealth of additional motion possibilities, as seen in Chapter 5. Complicated motions such as bending, screws, and bend-screws can be generated with parallel FREEs, and they can be analyzed and synthesized from the kinematics and volumetric transduction of the constituent FREEs. This synthesis method proves to be computationally efficient at scanning a large design space. A case study of a walking robot using parallel FREEs as an actuated spine shows the utility of the parallel FREE synthesis method.

Helical and bending motions are created with the addition of a single fiber to the two

fiber family FREEs. The key helix properties of helix angle and helix radius are modeled using the fiber angles and contained volume. While the equations and design spaces seem complicated, their ability to be written as explicit expressions allows for rapid computational synthesis. A case study of helical FREE anchoring inside pipes shows the utility of the equations in synthesizing complex helical FREEs.

7.2 Contributions

This dissertation discovered previously unknown FREE designs, models their behavior, experimentally verifies the models, and presents the results in a manner that allows others to understand, use, and expand on the work. The contributions of this dissertation include:

1. Discovery of an entire design space of fiber reinforcement configurations for elasto-fluidic systems not previously described in literature. This design space includes all two fiber family FREEs with and without a single fiber added. Prior knowledge in this space was limited to McKibben actuators and McKibben actuators with a longitudinal fiber added.

2. Determination of the kinematics and volumetric effects for the entire two fiber family FREE design space. Analytical models of the kinematics and volumetric transduction to output motion were developed and the kinematic models were experimentally verified across the entire design space in the extension-rotation directions.

3. Creation of an easy to use design tool describing the actuation, freedom, and constraint directions for each region of the two fiber family FREE design space.

4. Determination of the force and moment generation across the two fiber family FREE design space. Analytical models of the force and moment were developed and experimentally verified across the entire design space.

5. Creation of a method for the analysis and synthesis of parallel FREEs.

6. Modeling of an entire design space of helical and bending FREEs that use two fiber families and an additional single fiber.

These contributions combine to provide a mechanical designer with a vast design space of structures that are easily synthesized using the models, graphs, and tools presented in this dissertation. Practical applications were used to verify the utility of the newly discovered FREEs and the models that describe their mechanics. Three different applications

demonstrated the three different FREE fiber configurations and their respective models. These applications are an orthosis device for correcting arm contractures, a soft hexapod with parallel FREEs generating a walking gait, and a structure for pipe inspection devices. Each of these applications requires further engineering and research to reach applicable products, but they demonstrate novel and future applications of FREEs generated by this research.

7.3 Future Work

As Section 1.4.1 described, the goals of this research are beyond what could be accomplished in a single dissertation. The overall goal is to enable fiber-reinforced elasto-fluidic systems to become a regular part of mechanical design, allowing their numerous advantages to be applied to a multitude of applications. There are three main directions for future work that are necessary for the realization of this aspiration. The first area is further investigation of the mechanics of FREEs. The second main area is a refinement of the models presented in this dissertation. These models made numerous simplifying assumptions in order to capture the behavior of a vast design space with computationally simple expressions. Modeling and analyzing these structures provides essential information for design synthesis, but still leaves challenges in practical implementation. For broader acceptance of fiber-reinforced elasto-fluidic systems in engineering design, the third major area of research is in their fabrication and development of their surrounding component ecosystem.

Towards understanding the mechanics, the specific tasks are:

1. Research on the stiffness of FREEs, including the effect of the elastomeric enclosure. Elastomer stiffness is a complicated and active area of research. The coupling with the fibers and fluid to determine the overall system stiffness is essential towards using FREEs as structures, actuators, or mechanisms. Compressibility of the fluid is also important in the understanding of the stiffness of FREEs.

2. Research on the dynamic response of FREEs. Understanding the dynamics requires a model of the mass, stiffness, and force distributions. Modeling the visco-elastic properties of the elastomer and the effect of the fibers on strain tensors of the surface will help to determine the dynamic response.

3. Development of a model for parallel combinations of FREEs in which the primary axis is not parallel. This is important for developing systems that have control over many degrees of motion.

4. Development of control schemes suitable for elasto-fluidic systems. With the stiffness and dynamics understood, a control scheme that accounts for the non-linear, highly elastic response of FREEs needs to be conceptualized and refined. This research is important for transforming FREEs from structures to components of a system.

Towards refining the developed models, the tasks are:

1. Inclusion of boundary constraints and non-linearity effects of the fiber angles. The ends of the cylindrical FREEs were assumed to change in radius with the rest of the device, and the walls were assumed to remain straight. The fiber equations were simplified by assuming the angles did not change much as the FREE deformed. Refining the model to address these simplifying assumptions will yield more accurate predictions of kinematics, force, and volumetric transduction.

2. Modeling the fiber behavior. The fiber is treated as infinitely stiff, which presented some errors, especially with helical configurations of Chapter 6. Modeling the fiber's true stiffness profile across deflection will better capture its behavior and consequently refine the overall FREE models.

3. Determining the force-deflection relationship for FREEs. Chapter 2 modeled the unforced deflection of the FREEs, while Chapter 4 modeled their undeflected force. The interaction of force and deflection remains an important characteristic to understand for force and deflection control.

The remaining practical challenges to realizing these structures include:

1. Development of rapid and versatile methods for prototyping and mass production of FREEs.

2. Fabrication methods for small length scale devices. This includes both the meso- and mirco- scales.

3. Creation of small scale, lightweight, flexible valves to better control fluid flow, especially for actuators in series.

4. Development of soft compressors to generate fluid pressure.

In addition to advancing the models of existing FREEs, there are multiple modifications to the fundamental structure of fibers, elastomers, and fluids that will create new motion and actuation possibilities. These modifications include:

1. Replacement of some or all of the fibers with thin beams. Beams are able to withstand loads in both tension and compression, rather than only tension for fibers. Beam reinforcement will allow for FREE deformations that would otherwise buckle the fibers. For example, a contracting McKibben actuator with a longitudinal fiber would buckle when pressurized, but with a longitudinal beam, the FREE would bend. Chapter 6 shows large regions with no solutions, but beams could enable the entire design space with feasible solutions.

2. The addition of active fibers, elastomers, and/or fluids. This includes:
   (i) The replacement of some or all fibers with shape memory alloys (SMAs). Seok et al. [69] demonstrated this concept for a single fiber configuration, but the effect across the entire design space is not presently understood. Activating the fibers while simultaneously altering the fluid pressure will more closely mimic the behavior of many animals, providing many additional degrees of actuation.
   (ii) The replacement of some or all of the elastomer with electro-active polymers (EAPs). EAPs are often sheets of flexible material that have large actuation strains. They could provide many additional degrees of actuation as well as an integrated fluid pressure generation method.
   (iii) The addition of actuated fluids or gels. This includes ferrofluid (ferromagnetic fluid) and magnetorheological fluid, as well as phase changing, chemically reactive, and jamming materials.

3. Integration of FREEs into continuum structures and surfaces. Deformable, deployable, and controllable shapes and surfaces can be generated for numerous applications.

7.4 Potential Applications

An understanding of the vast design space of FREEs and their respective mechanics provides the opportunity to develop a wide range of applications. The inherent benefits of these elasto-fluidic systems provide solutions to existing problems, novel applications, and enhancements to existing designs. A few of the many application areas for these devices are:

- Medical devices (e.g. endoscopes) that utilize the diverse motion patterns, human-safe interactions, scalability, and high force transduction to enable carful manipulation of soft tissues. FREEs can be made very small with kinematics that can be tuned to match the morphological features.

- Orthoses (e.g. legs, arms, powered exoskeletons) that use the FREEs for their actuation, variable stiffness, and/or structural behavior. The continuum soft nature enables them to readily lie along the body with minimal risk of injury. The diversity of kinematics enables devices that can be tuned to the clinical need of each patient.

- Prosthetics that use FREEs either as structural elements with integrated stiffness control, or as actuation elements, providing power dense actuation of joints.

- Soft robots that have advantages in interacting directly with people, handling fragile objects, and navigating complicated environments.

- Manufacturing automation (seen in Figure 7.1) that provides a very low cost means to produce many degrees of actuation. FREEs could enable close human-machine interaction in manufacturing, replacing the current dangerous robots that must be kept separate from people.

- Deployable structures that have complex deployment, actuation, or freedom requirements. Inflatable structures are already widely used to provide compact deployment. FREEs will expand this area to provide additional functionality to these inflatable deployable structures.

- Sensing which uses the fluid transduction described in Chapter 3 to provide sensing in directions that are currently difficult to obtain.

- Grasping that using the FREEs as 'fingers' to enclose an object. This can be applied to agricultural robots (e.g. fruit picking). Anchoring is also possible, especially the use of helical FREEs to wrap around or inside pipes, the ground, or uneven surfaces.

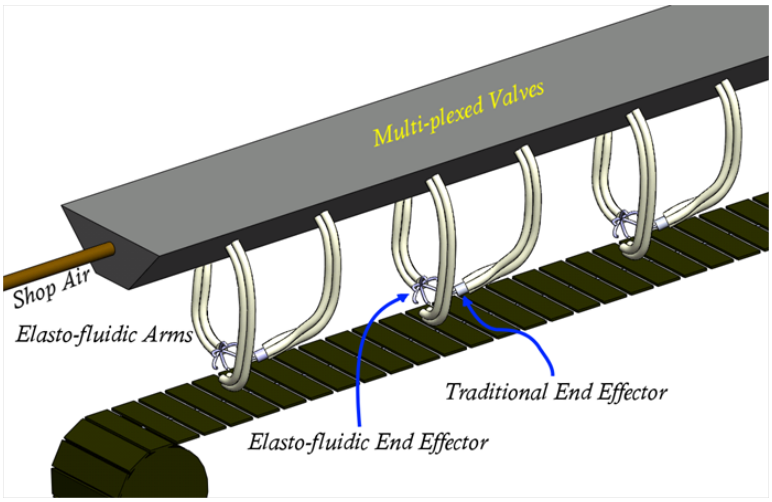

Figure 7.1: Conceptual rendering of an assembly line using a multitude of parallel elasto-fluidic systems.

BIBLIOGRAPHY

[1] JE Adkins and RS Rivlin. Large elastic deformations of isotropic materials x. reinforcement by inextensible cords. *Philosophical Transactions of the Royal Society of London. Series A, Mathematical and Physical Sciences*, 248(944):201–223, 1955.

[2] U.S. Energy Information Administration. About u.s. natural gas pipelines - transporting natural gas. http://www.eia.gov/pub/oil_gas/natural_gas/analysis_publications/ngpipeline/index.html.

[3] U.S. Environmental Protection Agency. Aging water infrastructure. www.epa.gov/sciencematters/april2010/scinews_aging-water-infastructure.htm.

[4] R Alexander. Bending of cylindrical animals with helical fibres in their skin or cuticle. *Journal of theoretical Biology*, 124(1):97–110, 1987.

[5] Paul Birkmeyer, Kevin Peterson, and Ronald S Fearing. Dash: A dynamic 16g hexapedal robot. In *Intelligent Robots and Systems, 2009. IROS 2009. IEEE/RSJ International Conference on*, pages 2683–2689. IEEE, 2009.

[6] Joshua Bishop-Moser and Sridhar Kota. Towards snake-like soft robots: design of fluidic fiber-reinforced elastomeric helical manipulators. In *Intelligent Robots and Systems (IROS), 2013 IEEE/RSJ International Conference on*. IEEE, 2013.

[7] Joshua Bishop-Moser, Girish Krishnan, Charles Kim, and Sridhar Kota. Design of soft robotic actuators using fluid-filled fiber-reinforced elastomeric enclosures in parallel combinations. In *Intelligent Robots and Systems (IROS), 2012 IEEE/RSJ International Conference on*, pages 4264–4269. IEEE, 2012.

[8] Joshua Bishop-Moser, Girish Krishnan, Charles Kim, and Sridhar Kota. Kinematic synthesis of fiber reinforced soft actuators in parallel combinations. *ASME Conference Proceedings*, 2012, 2012.

[9] Joshua Bishop-Moser, Girish Krishnan, and Sridhar Kota. Force and hydraulic displacement amplification of fiber reinforced soft actuators. *ASME Conference Proceedings*, 2013, 2013.

[10] Joshua Bishop-Moser, Girish Krishnan, and Sridhar Kota. Force and moment generation of fiber-reinforced pneumatic soft actuators. In *Intelligent Robots and Systems (IROS), 2013 IEEE/RSJ International Conference on*. IEEE, 2013.

[11] M Calisti, M Giorelli, G Levy, B Mazzolai, B Hochner, C Laschi, and P Dario. An octopus-bioinspired solution to movement and manipulation for soft robots. *Bioinspiration & biomimetics*, 6(3):036002, 2011.

[12] Gang Chen, Minh Tu Pham, and Tanneguy Redarce. Development and kinematic analysis of a silicone-rubber bending tip for colonoscopy. In *Intelligent Robots and Systems, 2006 IEEE/RSJ International Conference on*, pages 168–173. IEEE, 2006.

[13] C.P. Chou and B. Hannaford. Measurement and modeling of mckibben pneumatic artificial muscles. *Robotics and Automation, IEEE Transactions on*, 12(1):90–102, 1996.

[14] Robb William Colbrunn. *Design and control of a robotic leg with braided pneumatic actuators*. PhD thesis, Case Western Reserve University, 2000.

[15] Frank Daerden and Dirk Lefeber. Pneumatic artificial muscles: actuators for robotics and automation. *European journal of mechanical and environmental engineering*, 47(1):11–21, 2002.

[16] Steve Davis, N Tsagarakis, J Canderle, and Darwin G Caldwell. Enhanced modelling and performance in braided pneumatic muscle actuators. *The International Journal of Robotics Research*, 22(3-4):213–227, 2003.

[17] Eric G De Buda, John R Boon, and Michael P Dolbey. Pneumatically operated pipe crawler, February 8 1983. US Patent 4,372,161.

[18] A. De Greef, P. Lambert, and A. Delchambre. Towards flexible medical instruments: review of flexible fluidic actuators. *Precision Engineering*, 33(4):311 – 21, 2009/10/.

[19] Mingcong Deng, Aihui Wang, Shuichi Wakimoto, and Toshihiro Kawashima. Characteristic analysis and modeling of a miniature pneumatic curling rubber actuator. In *Advanced Mechatronic Systems (ICAMechS), 2011 International Conference on*, pages 534–539. IEEE, 2011.

[20] Kevin C Galloway, Panagiotis Polygerinos, Conor J Walsh, and Robert J Wood. Mechanically programmable bend radius for fiber-reinforced soft actuators.

[21] R.H. Gaylord. Fluid actuated motor system and stroking device, July 22 1958. US Patent 2,844,126.

[22] H Ghoneim and Sakif Noor. Pumping potential of a hyperbolic shell-of-revolution flexible-matrix-composite structure. *Composite Structures*, 2012.

[23] NC Goulbourne. A mathematical model for cylindrical, fiber reinforced electropneumatic actuators. *International Journal of Solids and Structures*, 46(5):1043–1052, 2009.

[24] Grzegorz Granosik and Johann Borenstein. Integrated joint actuator for serpentine robots. *Mechatronics, IEEE/ASME Transactions on*, 10(5):473–481, 2005.

[25] Joel Hetrick. *An energy efficiency approach for unified topological and dimensional synthesis of compliant mechanisms*. PhD thesis, University of Michigan, 1999.

[26] Shigeo Hirose and Hiroya Yamada. Snake-like robots [tutorial]. *Robotics & Automation Magazine, IEEE*, 16(1):88–98, 2009.

[27] Gerhard A Holzapfel and Thomas C Gasser. A viscoelastic model for fiber-reinforced composites at finite strains: Continuum basis, computational aspects and applications. *Computer methods in applied mechanics and engineering*, 190(34):4379–4403, 2001.

[28] Gerhard A Holzapfel, Thomas C Gasser, and Ray W Ogden. A new constitutive framework for arterial wall mechanics and a comparative study of material models. *Journal of elasticity and the physical science of solids*, 61(1-3):1–48, 2000.

[29] Filip Ilievski, Aaron D. Mazzeo, Robert F. Shepherd, Xin Chen, and George M. Whitesides. Soft robotics for chemists. *Angewandte Chemie - International Edition*, 50(8):1890 – 1895, 2011.

[30] Guy Immega and Keith Antonelli. The ksi tentacle manipulator. In *Robotics and Automation, 1995. Proceedings., 1995 IEEE International Conference on*, volume 3, pages 3149–3154. IEEE, 1995.

[31] Jin-Yong Joo. *Nonlinear synthesis of compliant mechanisms: topology and size and shape design*. PhD thesis, University of Michigan, 2001.

[32] Kenji Kawashima, Takahiro Sasaki, Ai Ohkubo, Toshiyuki Miyata, and Toshiharu Kagawa. Application of robot arm using fiber knitted type pneumatic artificial rubber muscles. In *Robotics and Automation, 2004. Proceedings. ICRA'04. 2004 IEEE International Conference on*, volume 5, pages 4937–4942. IEEE, 2004.

[33] DA Kelly. The functional morphology of penile erection: tissue designs for increasing and maintaining stiffness. *Integrative and Comparative Biology*, 42(2):216–221, 2002.

[34] Diane A Kelly. Penises as variable-volume hydrostatic skeletons. *Annals of the New York Academy of Sciences*, 1101(1):453–463, 2007.

[35] William M Kier. The diversity of hydrostatic skeletons. *The Journal of Experimental Biology*, 215(8):1247–1257, 2012.

[36] Hitoshi Kimura, Fumihiro Kajimura, Daisuke Maruyama, Michihiko Koseki, and Norio Inou. Flexible hermetically-sealed mobile robot for narrow spaces using hydrostatic skeleton driving mechanism. In *Intelligent Robots and Systems, 2006 IEEE/RSJ International Conference on*, pages 4006–4011. IEEE, 2006.

[37] G.K. Klute, J.M. Czerniecki, and B. Hannaford. Mckibben artificial muscles: pneumatic actuators with biomechanical intelligence. In *Advanced Intelligent Mechatronics, 1999. Proceedings. 1999 IEEE/ASME International Conference on*, pages 221 –226, 1999.

[38] Glenn K Klute and Blake Hannaford. Accounting for elastic energy storage in mckibben artificial muscle actuators. 2000.

[39] Mar Koehl, Kim J Quillin, and Charles A Pell. Mechanical design of fiber-wound hydraulic skeletons: the stiffening and straightening of embryonic notochords. *American Zoologist*, 40(1):28–041, 2000.

[40] Satoshi Konishi, Fumie Kawai, and Pierre Cusin. Thin flexible end-effector using pneumatic balloon actuator. *Sensors and Actuators A: Physical*, 89(1-2):28–35, 2001.

[41] Curt S Kothera, Mamta Jangid, Jayant Sirohi, and Norman M Wereley. Experimental characterization and static modeling of mckibben actuators. *Journal of Mechanical Design*, 131:091010, 2009.

[42] Girish Krishnan. *An intrinsic and geometric framework for synthesis and analysis of distributed compliant mechanisms*. PhD thesis, Ann Arbor, MI, USA, 2011.

[43] Girish Krishnan, Joshua Bishop-Moser, Charles Kim, and Sridhar Kota. Evaluating mobility behavior of fluid filled fiber-reinforced elastomeric enclosures. *ASME Conference Proceedings*, 2012, 2012.

[44] Shinya Kusuda, Satoshi Sawano, and Satoshi Konishi. Fluid-resistive bending sensor having perfect compatibility with flexible pneumatic balloon actuator. In *Micro Electro Mechanical Systems, 2007. MEMS. IEEE 20th International Conference on*, pages 615–618. IEEE, 2007.

[45] AD Kydoniefs. Finite axisymmetric deformations of an initially cylindrical membrane reinforced with inextensible cords. *The Quarterly Journal of Mechanics and Applied Mathematics*, 23(4):481–488, 1970.

[46] Cecilia Laschi, Barbara Mazzolai, V Mattoli, M Cianchetti, and P Dario. Design of a biomimetic robotic octopus arm. *Bioinspiration & Biomimetics*, 4(1):015006, 2009.

[47] W. Liu and C. R. Rahn. Fiber-reinforced membrane models of mckibben actuators. *Journal of Applied Mechanics*, 70(6):853–859, 2003.

[48] A Manuello Bertetto and M Ruggiu. Characterization and modeling of air muscles. *Mechanics Research Communications*, 31(2):185–194, 2004.

[49] Ramses V Martinez, Jamie L Branch, Carina R Fish, Lihua Jin, Robert F Shepherd, Rui Nunes, Zhigang Suo, and George M Whitesides. Robotic tentacles with three-dimensional mobility based on flexible elastomers. *Advanced Materials*, 25(2):205–212, 2013.

[50] Ramses V Martinez, Carina R Fish, Xin Chen, and George M Whitesides. Elastomeric origami: Programmable paper-elastomer composites as pneumatic actuators. *Advanced Functional Materials*, 22(7):1376–1384, 2012.

[51] Daisuke Maruyama, Hitoshi Kimura, Michihiko Koseki, and Norio Inou. Driving force and structural strength evaluation of a flexible mechanical system with a hydrostatic skeleton. *Journal of Zhejiang University: Science A*, 11(4):255 – 262, 2010.

[52] M Matsikoudi-Iliopoulou. Finite axisymmetric deformations with torsion of an initially cylindrical membrane reinforced with one family inextensible cords. *International journal of engineering science*, 25(6):673–680, 1987.

[53] R Skyler McCurley and William M Kier. The functional morphology of starfish tube feet: the role of a crossed-fiber helical array in movement. *The Biological Bulletin*, 188(2):197–209, 1995.

[54] W. McMahan, V. Chitrakaran, M. Csencsits, D. Dawson, I.D. Walker, B.A. Jones, M. Pritts, D. Dienno, M. Grissom, and C.D. Rahn. Field trials and testing of the octarm continuum manipulator. In *Robotics and Automation, 2006. ICRA 2006. Proceedings 2006 IEEE International Conference on*, pages 2336 –2341, may 2006.

[55] RL Moss, TG Rogers, and AJM Spencer. Axially symmetric deformations of fibre-reinforced cylinders. *IMA Journal of Applied Mathematics*, 26(1):21–38, 1980.

[56] N Nelson, Thomas Hanak, Kevin Loewke, and Daniel N Miller. Modeling and implementation of mckibben actuators for a hopping robot. In *Advanced Robotics, 2005. ICAR'05. Proceedings., 12th International Conference on*, pages 833–840. IEEE, 2005.

[57] Toshiro Noritsugu, Masahiro Takaiwa, and Daisuke Sasaki. Pneumatic rubber artificial muscles and application to welfare robotics. In *Next-Generation Actuators Leading Breakthroughs*, pages 255–266. Springer, 2010.

[58] United States Government Accountability Office. Water infrastructure: Comprehensive asset management has potential to help utilities better identify needs and plan future investments. Technical Report GAO-04-461, March 2004.

[59] United States Government Accountability Office. Pipeline safety: Better data and guidance needed to improve pipeline operator incident response. Technical Report GAO-13-168, January 2013.

[60] Hisakazu Onoe, Koichi Suzumori, and Takefumi Kanda. Development of tetra chamber actuator. In *Intelligent Robots and Systems, 2007. IROS 2007. IEEE/RSJ International Conference on*, pages 777–782. IEEE, 2007.

[61] Henry M Paynter. Low-cost pneumatic arthrobots powered by tug-and-twist polymer actuators. In *Proc. Japan-USA Symp. on Flexible Automation*, volume 1, pages 107–110, 1996.

[62] Henry M Paynter. Thermodynamic treatment of tug-&-twist technology: Part 1. thermodynamic tugger design. In *Proceedings, Japan-USA Symposium on Flexible Automation, Boston, MA*, pages 111–117, 1996.

[63] Henry M Paynter and JM Juarez. Thermodynamic treatment of tug-&-twist technology. 2. thermodynamic twistor design. In *Advanced Intelligent Mechatronics, 1999. Proceedings. 1999 IEEE/ASME International Conference on*, pages 826–829. IEEE, 1999.

[64] Larry Peel. *Fabrication and Mechanics of Fiber-Reinforced Elastomers*. PhD thesis, Provo, UT, USA, 1998.

[65] Larry D. Peel and Charles Ball. Fabrication and testing of a simple "bionic arm" demonstrator. *ASME Conference Proceedings*, 2010(44151):733–739, 2010.

[66] Larry D Peel, David W Jensen, and Koichi Suzumori. Batch fabrication of fiber-reinforced elastomer prepreg. *Journal of advanced materials*, 30(3):3–10, 1998.

[67] L.D. Peel, J. Mejia, B. Narvaez, K. Thompson, and M. Lingala. Development of a simple morphing wing using elastomeric composites as skins and actuators. *Journal of mechanical design*, 131(9), 2009.

[68] William F Rush, James E Huebler, and Christopher J Ziolkowski. Pneumatic pipe inspection device, March 3 1987. US Patent 4,646,787.

[69] Sangok Seok, Cagdas Denizel Onal, Robert Wood, Daniela Rus, and Sangbae Kim. Peristaltic locomotion with antagonistic actuators in soft robotics. In *Robotics and Automation (ICRA), 2010 IEEE International Conference on*, pages 1228–1233. IEEE, 2010.

[70] Maloclm K Seymour. Some implications of helical fibres in worm cuticles. *Journal of Zoology*, 199(3):287–295, 1983.

[71] Robert E Shadwick. Foundations of animal hydraulics: geodesic fibres control the shape of soft bodied animals. *Journal of Experimental Biology*, 211(3):289–291, 2008.

[72] Ying Shan, Michael P Philen, Charles E Bakis, Kon-Well Wang, and Christopher D Rahn. Nonlinear-elastic finite axisymmetric deformation of flexible matrix composite membranes under internal pressure and axial force. *Composites Science and Technology*, 66(15):3053–3063, 2006.

[73] Koichi Suzumori. Elastic materials producing compliant robots. *Robotics and Autonomous Systems*, 18(1):135–140, 1996.

[74] Koichi Suzumori, Shoichi Iikura, and Hirohisa Tanaka. Development of flexible microactuator and its applications to robotic mechanisms. In *Robotics and Automation, 1991. Proceedings., 1991 IEEE International Conference on*, pages 1622–1627. IEEE, 1991.

[75] Koichi Suzumori, Shoichi Iikura, and Hiroshisa Tanaka. Applying a flexible microactuator to robotic mechanisms. *Control Systems, IEEE*, 12(1):21–27, 1992.

[76] Toshio Takayama and Shigeo Hirose. Amphibious 3d active cord mechanism. In *Intelligent Robots and Systems, 2002. IEEE/RSJ International Conference on*, volume 1, pages 775–780. IEEE, 2002.

[77] Joseph T Thompson and Janet R Voight. Erectile tissue in an invertebrate animal: the octopus copulatory organ. *Journal of Zoology*, 261(1):101–108, 2003.

[78] B. Tondu and P. Lopez. Modeling and control of mckibben artificial muscle robot actuators. *Control Systems, IEEE*, 20(2):15–38, 2000.

[79] Bertrand Tondu. Modelling of the mckibben artificial muscle: A review. *Journal of Intelligent Material Systems and Structures*, 23(3):225–253, 2012.

[80] Brian Trease. *Topology synthesis of compliant systems with embedded actuators and sensors*. PhD thesis, Ann Arbor, MI, USA, 2008.

[81] D. Trivedi, C.D. Rahn, W.M. Kierb, and I.D. Walker. Soft robotics: biological inspiration, state of the art, and future research. *Applied Bionics and Biomechanics*, 5(3):99 – 117, Sept. 2008.

[82] Deepak Trivedi, Dustin Dienno, and Christopher D Rahn. Optimal, model-based design of soft robotic manipulators. *Journal of Mechanical Design*, 130:091402, 2008.

[83] Deepak Trivedi, Amir Lotfi, and Christopher D. Rahn. Geometrically exact models for soft robotic manipulators. *IEEE Transactions on Robotics*, 24(4):773 – 780, 2008.

[84] N. Tsagarakis and D.G. Caldwell. Improved modelling and assessment of pneumatic muscle actuators. In *Robotics and Automation, 2000. Proceedings. ICRA'00. IEEE International Conference on*, volume 4, pages 3641–3646. IEEE, 2000.

[85] Ravi Vaidyanathan, Hillel J Chiel, and Roger D Quinn. A hydrostatic robot for marine applications. *Robotics and Autonomous Systems*, 30(1):103–113, 2000.

[86] Steven Vogel. *Comparative biomechanics: life's physical world*. Princeton University Press, 2013.

[87] Stephen A Wainwright. *Axis and circumference: the cylindrical shape of plants and animals*. Harvard University Press Cambridge MA:, 1988.

[88] III Webster, R.J. and B.A. Jones. Design and kinematic modeling of constant curvature continuum robots: A review. *International Journal of Robotics Research*, 29(13):1661 – 83, 2010/11/.

[89] A Wedler, J Friederichs, F Hackelöer, and B Denkena. New compliant mc-kibben actuator driven by pneumatic actuators as a hexapod platform in robotic applications. Technical report, Technical report, Institute of Production Engineering and Machine Tools, Leibniz University Hannover, 2008.

[90] Zhiye Zhang. *Modeling, Analysis, and Experiments of Inter Fiber Yarn Compaction Effects in Braided Composite Actuators*. PhD thesis, Virginia Polytechnic Institute and State University, 2012.

[91] Bin Zhu, Christopher D Rahn, and Charles E Bakis. Actuation of fluidic flexible matrix composites in structural media. *Journal of Intelligent Material Systems and Structures*, 23(3):269–278, 2012.